Summer 2013

Creating new superconducting & semiconducting nanomaterials and investingating the effect of reduced dimensionality on their properties

Sukhada Mishra

Department: Chemistry

Recommended Citation

Mishra, Sukhada, "Creating new superconducting & semiconducting nanomaterials and investingating the effect of reduced dimensionality on their properties" (2013). *Doctoral Dissertations*. 2060.
https://scholarsmine.mst.edu/doctoral_dissertations/2060

CREATING NEW SUPERCONDUCTING & SEMICONDUCTING NANOMATERIALS AND INVESTINGATING THE EFFECT OF REDUCED DIMENSIONALITY ON THEIR PROPERTIES

by

SUKHADA MISHRA

A DISSERTATION

Presented to the Faculty of the Graduate School of the
MISSOURI UNIVERSITY OF SCIENCE AND TECHNOLOGY
In Partial Fulfillment of the Requirements for the Degree

DOCTOR OF PHILOSOPHY
in
CHEMISTRY
2013

Approved by

Dr. Manashi Nath, Advisor
Dr. Philip Whitefield
Dr. Nicholas Leventis
Dr. Jeffrey Winiarz
Dr. Matthew O'Keefe

PUBLICATION DISSERTATION OPTION

This dissertation consists of two published articles, two articles which have been submitted for publication and one manuscript in preparation. Paper I, found on pages 52—88, is published in ‘*ACS Nano*’. Paper II included in pages 89—109, has been submitted for publication to ‘*Advanced Materials*’. Paper III, found on pages 110—135, is published in ‘*Nano Energy*’. The pages 136—150 are from the manuscript under preparation (Paper IV) intended for the submission in ‘*Journal of Material Science and Engineering B*’. Paper V (Pages 151—163) has been submitted to ‘*Nanoscale*’.

ABSTRACT

The field of nanomaterials has continued to attract researchers to understand the fundamentals and to investigate potential applications in the fields of semiconductor physics, microfabrication, nanomedicine, surface sciences etc. One of the most critical aspects of the nanomaterials research is to establish synthetic protocols, which can address the underlying product requirements of reproducibility, homogenous morphology and controlled elemental composition. We have focused our research in exploring synthetic routes for the synthesis of superconducting and semiconducting nanomaterials and analyze their structure—property relationship through detailed characterizations.

The first part of dissertation is focused on the synthesis of superconducting FeSe nanostructures using catalyst assisted chemical vapor deposition (CVD) technique. The effect of catalyst—FeSe interphase on the *d* spacing of the FeSe nanostructures has been analyzed, and the internal pressure effect on the T_c has been investigated further through in depth characterizations. The emphasis of second part is on the development of a simple yet versatile protocol for the synthesis of vertically aligned nanorod arrays on conducting substrate by combining electron beam lithography technique with electrochemical deposition. The technique has been utilized to fabricate photovoltaic CdTe nanorod arrays on conducting substrate and further extended to devise CdS—CdTe nanorod arrays to create radial and lateral p—n junction assembly. Using photo—electrochemical analysis, it was observed that, the nanorod arrays yielded higher photo—electrochemical current compared to the thin film counterpart. The third part of dissertation describes the CVD protocol to synthesize multifunctional, dumbbell shaped Au—CoSe nanoparticles, which possess potential applications in '*theronostic*' biological examinations.

ACKNOWLEDGEMENTS

I would like to express my deepest gratitude to my Graduate Advisor, Dr. Manashi Nath, for the encouragement, supervision and support throughout the course of my academic progress. Without her guidance and persistent help, this dissertation would not have been possible. Her expertise in Nanotechnology, Materials Chemistry and endless guidance has crafted me, improved my research skills, and prepared me for future challenges. She has been extremely considerate to me during my hard times and she truly holds a position of a mentor, philosopher and guide to me.

I owe sincere and earnest thankfulness to my committee members, Dr Nicholas Leventis, Dr. Philip Whitefield, Dr. Jeffrey Winiarz and Dr. Mathew O'Keefe for their continuous support and assistance. Words are not enough to express my gratitude towards Dr. Kai Song for his invaluable contribution towards the electron microscopy characterizations. Working with him was a learning experience and it gave me an opportunity to understand the critical aspects of TEM characterizations. I would like to thank entire team at the Materials Research Center for helping me in various characterization techniques. I am grateful to the Department of Chemistry for providing me teaching assistantship during my graduate studies.

My friends Prachi Desai, Shruti Mahadik, Aditya Khanolkar hold a central role in my personal life during the times spent at Rolla. I thank my lab mates Wipula Liyange and Akshay Pariti for their assistance. I offer my gratitude and regards to all of those who supported me in any respect during the completion of the projects.

This journey was impossible without the support, encouragement and unconditional love from my husband Mr. Joyesh Mishra, my parents Mr. Chandrakant Patil and Mrs. Latika Patil, and in—law parents Dr. Bibekananda Mishra, Radha Mishra, brother Novokesh, my sister Mayura, brother in law Sushil and my little niece Ananya. I would like to dedicate this dissertation to my family.

TABLE OF CONTENTS

Page

SECTION

PAPER

SECTION

LIST OF ILLUSTRATIONS

PAPER I

PAPER II

PAPER III

PAPER IV

PAPER V

SECTION

LIST OF TABLES

Table Page

1. INTRODUCTION

1.1. NANOMATERIALS

All matter is composed of atoms—the key building blocks of material, which provide the material it's composition, microstructure, characteristics, and individual properties. The atomic structure primarily affects the chemical, physical, thermal, electrical, magnetic, and optical properties. These properties of the material could be tailored by carefully controlling the atomic building blocks in order to create efficient, faster, cost effective and viable materials. Nanotechnology is the latest advancement in the world of Material Sciences. It refers to constructing and manufacturing of the systems at atomic level. Nano is one billionth part of the meter in comparison to the normal carbon bond length. The physical properties of the materials can alter significantly in the nano regime, compared to the bulk or even molecular level.[1] Nanotechnology has emerged few decades ago but the concept has arisen billion years ago in the nature during the formation of life.[2] In the evolution process while the life was being evolved in the form of birth of living species, reproduction, survival, and formation of innumerable compounds through elements, everything has taken place at nanoscale in nature. Ribosomes, photosynthetic chloroplast are some examples of molecular machineries.[2] In ancient times; Chinese were known to use gold nanoparticles in the dye to form colored ceramic.[3]

Great visionary scientist Richards Feynman had foreseen the significance and emergence of nanotechnology and in 1959 he introduced the concept of nanotechnology in his talk 'there's plenty of room at the bottom'.[4] He described the concept of miniaturization and the idea of building the materials using individual atoms and molecules as building blocks, control the properties of materials and manipulate the characteristics of the material. In his talk, he described advanced ideas, such as writing an entire 24 volumes of encyclopedia Britannica on the head of a pin, and building nano—robots which can perform functions of advanced manufacturing. It needed great deal of efforts for the development of tools and technology in order to understand the prediction and utilize the concept of nanotechnology in real life. After two decades, the limitations associated with light microscope had been conquered with the invention of scanning tunneling microscopy (STM) and high resolution transmission electron microscopy (HRTEM). The invention of electron microscopy played a vital role in observation, analysis and discovery of fullerenes in 1985[5] followed by the discovery of carbon nanotubes in 1991.[6] This was the beginning of new era of nanoscience and since then, the journey of nanomaterials is progressing at a faster pace, leading to many fascinating discoveries affecting optical, electrical, magnetic behavior of materials. The direct integration of nanomaterials in currently established materials, to improve their properties is referred as 'incremental nanotechnology'.[7] The fabrication of entirely new devices and functionalities using self—assembly of the nanomaterials is termed as 'evolutionary nanotechnology'.[8] As nanotechnology also possesses environmental and social impacts, it becomes utmost importance to study the nanomaterials and contribute towards the advancement of the research.

The fundamentals of the field of basic sciences such as chemistry, physics, biology, material science have been analyzed and understood in depth, which makes the potential research and practical applications viable. But in case of nanostructures and nanomaterials, in depth understanding of physical characteristics, the effect of size on material properties and the reasons behind fascinating variations in the properties is yet to be achieved. As newer nanomaterials are being discovered, and explored in the potential applications, the size employs challenges associated with the measurement and characterizations, extraction of the formed product. The complex, multistep synthetic protocols employ difficulty in purification of the product from the reaction system. The characterization instruments, synthesis tools are complex and expensive, which make the fabrication of nanodevices challenging. These factors collectively make the synthesis of nanomaterials economically difficult.

Nanostructures are broadly categorized into three types based on the growth of the nanostructures—

1. Zero Dimension Nanomaterials
2. One Dimension Nanomaterials
3. Two Dimensional Nanomaterials
4. Three Dimensional Nanomaterials

Figure 1.1 demonstrates the classification of nanostructures. Zero dimension nanomaterials include the quantum dots, nanoparticles. Typically, the dimensions of quantum dots lie in the range 1–30 nm. The special cases of nanocrystals—the semiconducting quantum dots have been analyzed in depth and have been established for their optical properties.[9] Quantum dots are widely applied in applications as sensors, lasers, and LEDs. The fabrication of high density disks like HD—DVD, high definition blue—ray DVDs, is highly dependent on the use of quantum dots and those could only be read via blue lasers. Quantum dots also hold long—term applications in optical computing and high—efficiency solar cells. Magnetic nanoparticles has been widely used

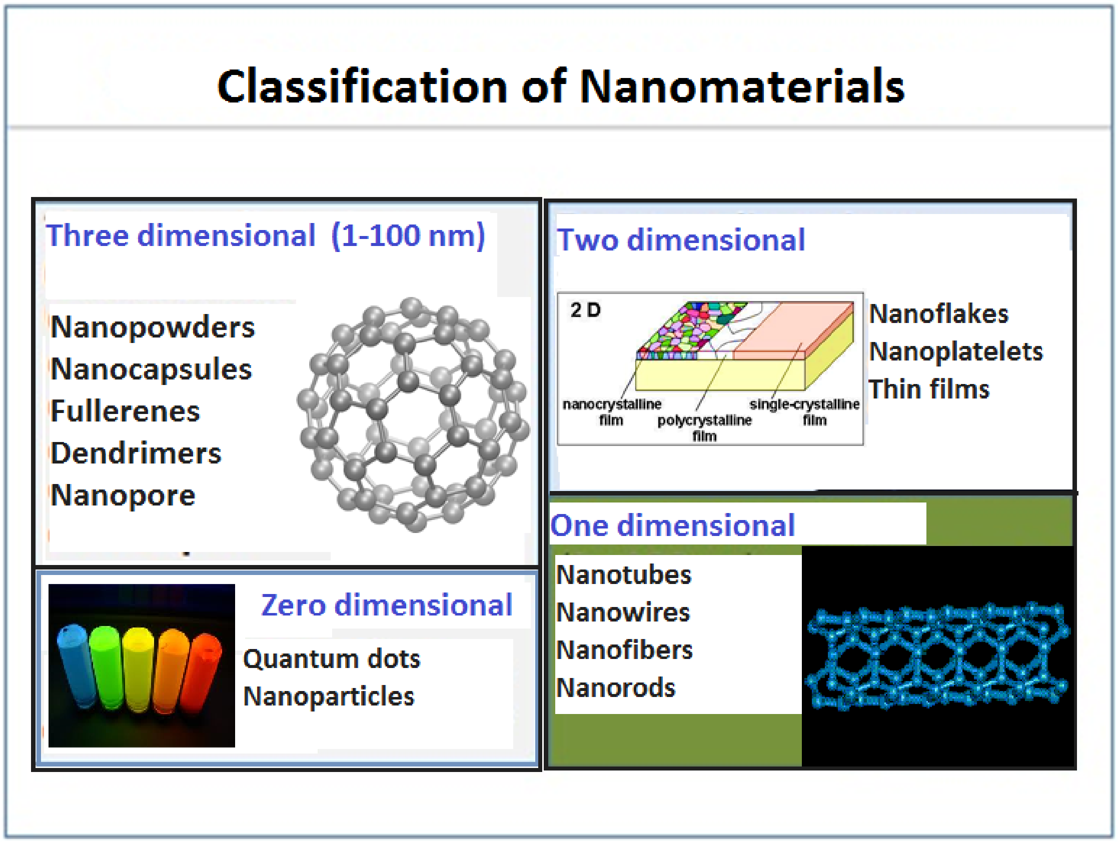

Figure 1.1. Schematic representation of the classification of nanomaterials based on the size of nanostructures

as enhanced hard or soft magnets, as they provide the benefits of lower energy losses and fast response to the external magnetic fields. They have been successfully implemented in applications such nano medicine, catalysis, ferrofluids, drug delivery etc.[10]

One dimensional nanostructure includes nanowires, nanotubes, nanofibers, nanorods and nanobelts. These structures have high aspect ratio of about 100 nm in lateral dimension and unconstrained (micron or larger) in longitudinal dimension. The major difference between nanotubes and nanowires, nanorods, nanofibers, nanobelts results from their morphology. Nanofibers are commonly designated term for one dimensional structure of polymers and nongraphitized carbon. On the other hand, nanowires are crystalline in nature and nanorods possess comparable dimensions of length and the width (both dimensions are less than 100nm). Nanorods are completely linear in shape and contain highly rigid sidewall structures. Two dimensional nanostructures are free—standing 2—dimensional nanostructures, termed as nanoplates, or nanosheets. Nanoplatelets can be metallic, dielectic or semiconducting in nature, and possess uniform thickness smaller than the lateral dimensions. Three dimensional nanostructures includes fullerenes, nanocrystals, nanoclusters, dendrimers etc. The nanocrystals include the class of nanocubes, hexagonal, pentagonal, tetrahedral, octahedral, cuboctahedral, and octahedron nanocrystals.

1.2. PROPERTIES OF NANOMATERIALS

The electronic, optical and magnetic properties of the nanomaterials deviate substantially compared to the bulk materials. This section mentions some of the notable properties of nanomaterials.

1.2.1. Quantum Confinement Effect. The quantum confinement effect is observed when the diameter of the nanoparticles is in magnitudes comparable/smaller than the wavelength of the electron wave function.[11] Figure 1.2 demonstrates the quantum confinement effect schematically. As a result of quantum confinement effect the bandgap of the nanoparticles become size dependent. In the bulk materials, when an electron is transferred from valence band to the conduction band, electron—hole pair is created which is called as exciton. The separating distance between this electron—hole pair is termed as exciton Bohr radius (r_B). Table 1.1 lists the r_B values for common semiconductor crystals.[11] In bulk material the r_B is typically smaller compared to the crystal dimensions, so the excitons are free to migrate in the lattice. Quantum

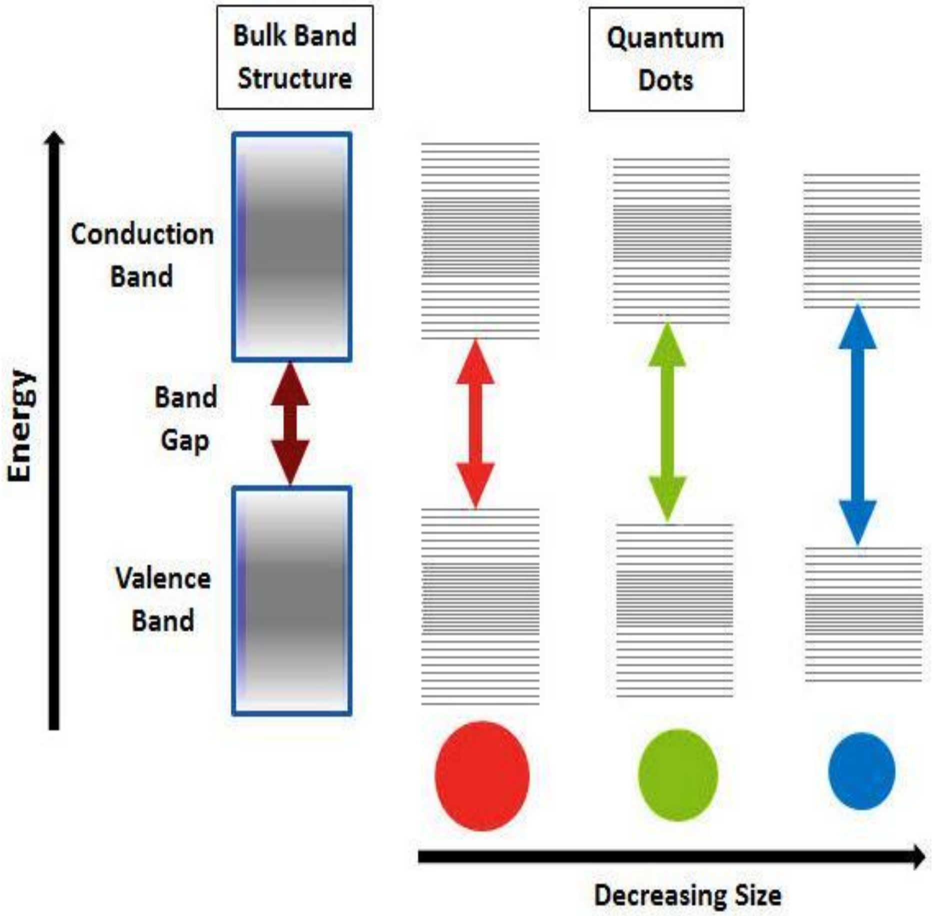

Figure 1.2. Schematic representation of the quantum confinement effect in semiconducting nanoparticles.

confinement effect occurs as a direct effect of electrons and holes being entrapped into a quantum dot having dimensions equivalent to r_B. This confinement gives rise to discrete energy levels in the nanoparticles, as opposed to continuous bands in the bulk crystals. Owing to the confinement of electrons and holes, the energy for the optical transition of electrons and holes from valence band to conduction band increases, i.e. band gap increases. This effect can be analyzed by studying the optical characteristics of the quantum dot solutions. It has been observed that

Table 1.1 List of exciton Bohr radius (r_B) of the common semiconducting compounds.

Material	r_B **(Å)**
Si	**55**
CdS	**315**
CdSe	**61**
CdTe	**100**
ZnO	**18**
ZnS	**50**
PbS	**204**
PbSe	**460**
InAs	**340**
InSb	**540**

with increase in the size of the quantum dots, the wavelength of absorption of light shifts from blue region to red region, thereby, tuning the size of the quantum dot (should be less than r_B), the band gap can be fine—tuned.[11]

1.2.2. Localized Surface Plasmon Resonance. Surface plasmon resonance (SPR) is the unique property of certain metals. Figure 1.3 represents the schematic of the surface resonance phenomenon. As metals are good conductors of electricity, they contain closely packed atoms which can share electrons and effectively led to the formation of delocalized electrons or "sea of *electrons*". These coherent electrons oscillate at the interphase between the metal and dielectric medium such as air or water to produce surface plasmons (SPs). SPs possess lower energy compared to bulk plasmons. The bulk plasmons contribute in longitudinal electron oscillations at the positive ion cores within the bulk of the plasma. When the SPs combine with a photon, it produces a hybridized excitation state which is called as surface plasmon polarization (SPP). The SPP propagates along the surface of a metal until energy is lost either via absorption in the metal or radiation into free—space. The SPR appears when the surface plasmons get

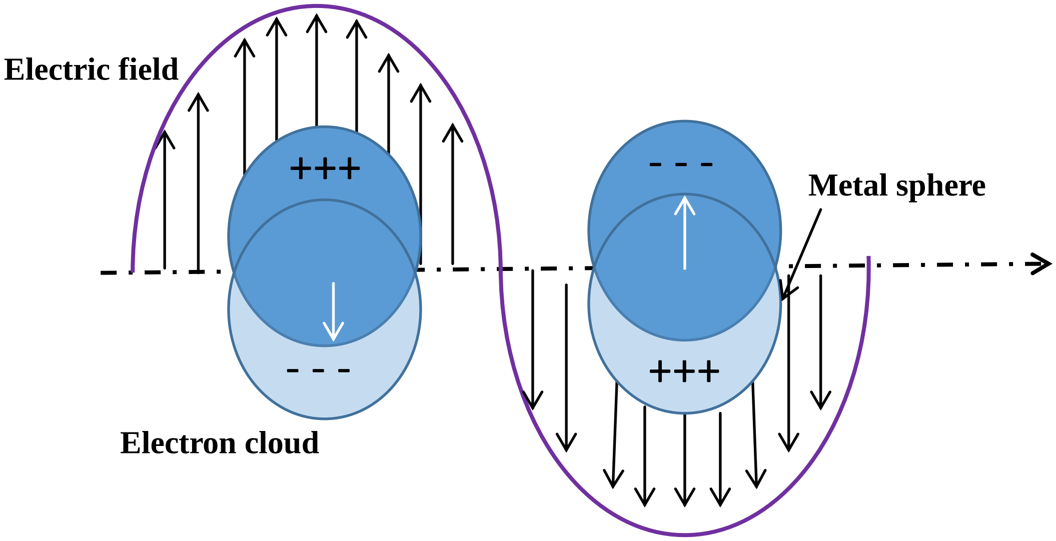

Figure 1.3. Schematic representation the electron delocalization and characteristic charge density wave at the surface of the metal causing SPR.

excited by incoming photons, on the surface of the metallic thin film. In this process, the photon gets transformed into a surface plasmon and when the wavelength of the photon coincides with the wavelength of the natural frequency of the surface plasmons, the resonance condition is established. These processes depend on the refractive index of the adsorbate, angle of incident light, size of the nanoparticles/ surface roughness etc. SPR occurring in the nanoparticles is called localized "*localized surface plasmon resonance*".[12] These localized surface plasmon oscillations provide intense colors to suspensions/ sols containing nanoparticles. Noble metal nanoparticles/ nanowires possess strong absorption bands in UV light ranges, which are absent in bulk metals. This characteristic of exceptional absorption in ultraviolet region has been utilized to increase photon absorption in solar cells by depositing thin layer of metal nanoparticles on the cell surface.[13] SPR is the basic principal used in the applications such as color—based biosensors, lab—on—a—chip sensors, SPR immunoassay, quartz crystal microbalance (QCM), DNA/ protein detection and so on.[14]

1.3. SYNTHESIS AND FABRICATION OF NANOMATERIALS

The synthesis of nanomaterials concentrates on the control of size, shape and structure by employing physical and chemical methodologies. Synthesis can be categorized into two major techniques as represented by Figure 1.4.

(1) Top down approach and

(2) Bottom up approach.

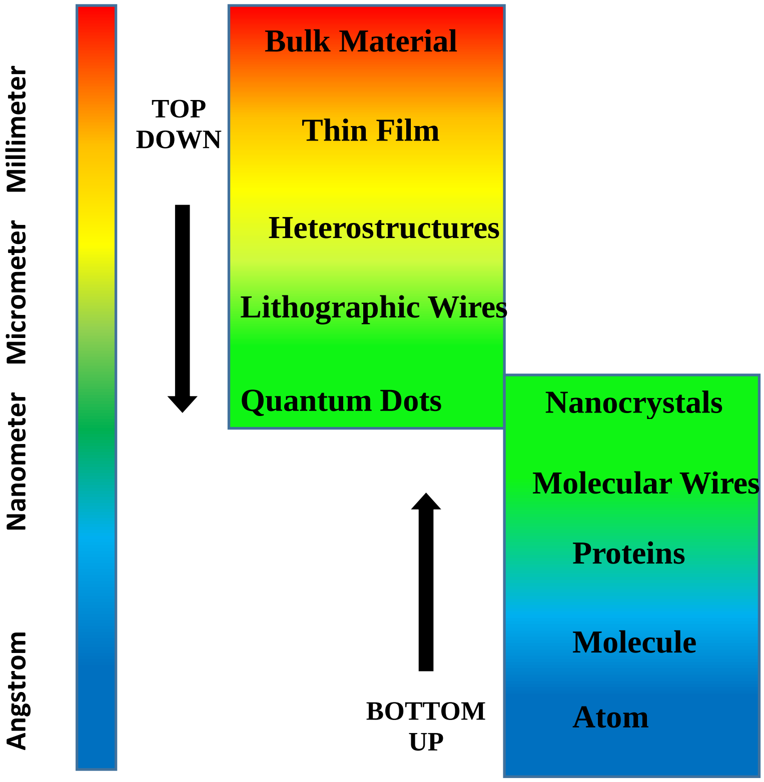

Figure 1.4. Schematic representation of the classification of the two fundamental approached of nanomaterials synthesis.

1.3.1. Top—Down Approach. In top down approach, nanomaterials are fabricated using larger entities, by slicing or cutting the bulk material without affecting atomic composition of original material. Usually top down approach is practiced less as compared to the bottom up approach.

1.3.1.1 Mechanical milling method. Milling or attrition method is the most common method for the synthesis of nanoparticles.[15—20] During milling operations, the kinetic energy from a grinding medium is transferred to a material undergoing reduction in size. This method is most commonly used for the nanocomposites or nanograined bulk materials in metallurgical and ceramic industry,[21] where the sintering is carried out at lower temperatures.[3] Owing to its inexpensive equipment set—up and universal applicability to all classes of materials, ball milling is the simplest technique for the fabrication of nanoparticles.[20] The homogeneity and the size of the nanoparticles vastly depend on the milling speed and time. Surfactants such as oleic acid, oleylamine and 11—phenoxyundecanoic acid and solvents such as heptane are also included in the formulations to achieve narrow size distribution and better dispersion in the solvents.[16,22] Ball—milling technique has been successfully employed to synthesize varieties of semiconducting nanomaterials such as ,ZnO,[17,20] CuO,[24] Si,[25] magnetic nanomaterials — magnetite Fe2O3,[18] Sm–Co hard magnetic nanoparticles,[21] nanoparticles of Fe, Co, FeCo, SmCo, and NdFeB,[16] nanostructures of NdFeB,[16,26] (Sm—Co,Fe) nanoparticles,[23] nanoflakes of SmCo5,[27] nanocomposite of $SmCo_5$/Fe carbon nanotubes,[29—31] boron nitride nanotubes,[32—35] etc. The process of ball milling lowers the melting point of the material, which in turn facilitate the operation at room temperature which increases safety and reduces energy consumption, also in this technique no gaseous by products are not produced.[36]

1.3.1.2. Lithography techniques. In lithography fabrication techniques, the existing structure can be reduced in dimensions using chemical processes combined with electronic, photonic, ionic or X—ray radiation on sensitive resists. The technique consists of scanning a finely focused beam of radiation source across a surface covered with a resist film, sensitive to the radiation. The desired pattern receives the energy on the resist film. This process is followed by the post—development processes which involve etching of the resist material from the patterned area using suitable solvent. Figure 1.5 shows the schematic representation of the lithography processes, which may consists of one of the two types of resists—positive or negative resist. In the case of positive resist, the beam energy destructs the chemical bonds of the resists, which makes the resist in the patterned region more soluble in developing solvents. In the case of the negative resist the beam energy cures the resists, which makes the resist in the patterned region less soluble in the developing solution and the non—patterned regions gets selectively dissolved. The following two parameters of resists play important role in defining the accuracy of the fabrication.[37] (1) Sensitivity of the resist: This parameter refers to the dose of the induced radiation required in order to produce sufficient chemical changes in the resists. Higher sensitivity of the resist will require smaller time of exposure and lower dose of radiations.

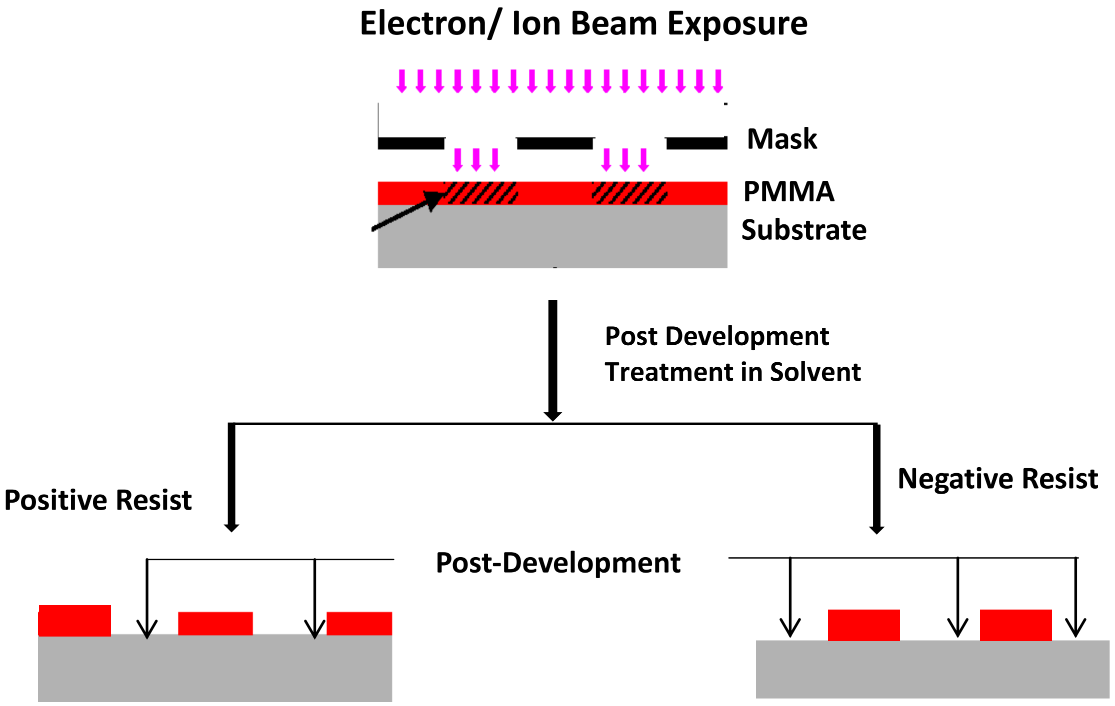

Figure 1.5. Schematic representation of the general protocol for fabrication of nanostructures using electron beam/ ion beam lithography technique.

(2) Contrast of the resist: This parameter measures the rate of solubility of the developing solution as a function of time. Higher contrast of the resist led to better spatial resolution of the fabrication. The resolution of about 32 nm is achievable using UV lithography, while line widths of ~20 nm are achieved using electron beam lithography. Ion beam lithography is the most sensitive technique, and offers higher resolution of about 10 nm feature size. Ion beam has 370 time higher mass compared to electron beam,[37] which provides a higher momentum to the focused beam, it also provides smaller wavelength to the beam and therefore lack of diffraction provides a better resolution compared to photolithography, e—beam lithography. Ion beam also possess important property of milling/ sputtering the atoms from the patterned area, due to which ion beam lithography can be used for subtractive as well as additive lithography.[37] These lithography techniques have been used widely to fabricate quantum dots and wires. The factors governing the electron beam lithography have been discussed in detail in chapter 2.

1.3.1.3. Advantages and disadvantages of top—down approach. Ball milling/ high energy method is the most inexpensive method for the synthesis of nanostructures compared to other synthetic approaches. Though it can be applied for a large scale synthesis, the choice of the material remains limited. Designing and execution of the process is difficult, and the nanomaterials generated through this method possess high degree of imperfections of surface structure and non—uniform size distribution. Significant amount of crystallographic damage occurs during high energy milling process. The end product also contains impurities from the milling medium. The milling operation produces nanostructures in the size range of 20—100 nm. Thus wide size distribution, amorphorization of the material during the process, particle contamination, varied particle size and geometry, non—uniform particle surface are the major disadvantages of this methodology. The lithography techniques are capable of producing nanostructures at very high resolution. The method can work with wide variety of patterns to fabricate atomic scale structures. The most important drawback is, the surface has to be extremely uniform and should possess flat morphology. The process is expensive and requires expensive fabrication tools. It is inflexible technique, as the material of choice are limited.

1.3.2. Bottom—Up Approach. Bottom—up synthesis methods are practiced in industry over a century and these are the most important fabrication tool for the synthesis and processing of nanomaterials.[37] The bottom—up approach consists of reaction between two or more atomic or molecular components to produce end product. This approach includes gas—phase methods like CVD, MOCVD, ALD, liquid phase synthesis, template methods etc. Substantial amount of work has been done for the nanomaterials synthesis through bottom up techniques. Control of size, shape, morphology, chemical composition along with monodispersity can be achieved through bottom up approach hence it is most commonly employed for the synthesis of nanoparticles.

The methods included as bottom—up approach which use solution based synthesis are—nanoparticle growth within dendrimers,[38] hot injection method,[39—41] arrested precipitation etc. These synthesis methods are based on the thermodynamics and kinetics of the reaction. Thermodynamically controlled reaction consists of generation of supersaturation, nucleation, and subsequent growth of the nanoparticles,[37] while in kinetically controlled reaction the further growth of the nanoparticles is quenched by limiting the amount of precursors or by confining growth of the formed material in micelles or zeolite. Amine terminated, poly(aminoamide) and poly(propylene imine)[38] dendrimers were widely used for the synthesis of metals Cu, Au, Pt, Pd, Au, CdS and bimetallic nanoparticles.[39] The control of the size of the nanoparticles is achieved as dendrimers are monodispersed in solution and provide the molecular framework. The reactive surface groups on the polymer provide the linking sites for the metal nanoparticles which cause the selective confinement of the metallic precursors. This process is followed by reduction of the ions to metallic nanoparticles inside the dendrimer using reducing agents such as $NaBH_4$. Dendrimers act as molecular frameworks and not only physically separate the formed nanoparticles but also prevent the agglomeration of the formed nanoparticles. The major limiting factor for the use of dendrimers is, it contains multiple chemical synthesis steps.[40] One—step liquid phase synthetic technique has also been described for the synthesis of monodispersed Pd nanoparticles using thioethers.[41]

Hot—injection synthesis is most explored liquid phase synthetic protocol which is used for the fabrication of monodispersed, well defined shaped nanoparticles with accurate and narrow size distribution. Quantum dots of CdSe,[42] CdS,[43] ZnO,[44] $CoPt_3$,[45] FePt,[46] PbSe,[47] PbS,[48] has been synthesized using hot injection technique. It is a versatile technique in which the size and shape of the nanoparticles can be tuned by manipulating the reaction parameters such as, reaction temperature, molar ratio of surfactants such as olylamine, hexadecylamine (HDA), tri—octyl phosphine (TOP), tri—octyl phosphine oxide (TOPO).[49] In this method, non—ionic precursors are injected in high—boiling organic solvents. In such conditions, the nanoparticles grow at slower rate at high temperature which yields defect—free, well passivated nanocrystals.

1.3.3. Chemical Vapor Deposition. Chemical vapor deposition (CVD) is a rapidly developing technique in which the deposition of the nanomaterials/ thin films depends on the factors such as precursor design, reaction pathways, reactor types, and reactor operating conditions. Figure 1.6 shows the horizontal tube based single zone furnace with the parameters. As variety of parameters could be controlled in the reactor design, CVD is considered to be a versatile technique. CVD technique has been explored extensively and it possesses wide range of literature.[50—61] The relatively simple and inexpensive CVD method is one of the promising techniques for the fabrication of large area, single— to few— layer thick graphene on polycarbonate Ni film on SiO_2 substrate.[50] The synthesized graphene demonstrated high degree of purity and showed conductivity characteristics after multiple processing steps.[50,51,52,53] Other reports also demonstrated the growth of graphene layers on Cu foil using CVD method.[54]

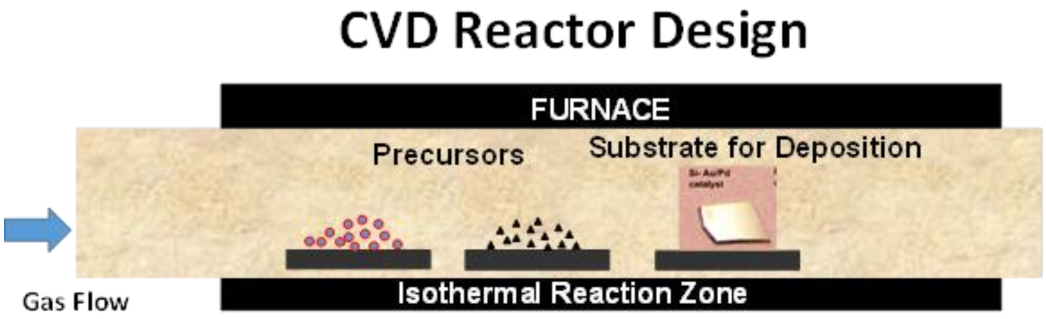

Figure 1.6. Schematic representation of processes occurring at the molecular level during a catalyst assisted chemical vapor deposition.

Impressively, CVD was successfully employed to achieve the largest graphene, approximately 30 inches, made ever compared to any other method.[55] In another approach, polymethyl methacrylate, benzene and polystyrene precursors were used as a source of carbon in CVD reactor to establish convenient and economical route for the synthesis of graphene.[56] CVD is considered as the foremost important tool in the area of synthesis of carbon nanotubes (CNTs). In 1959 catalyst aided vapor deposition of carbon was reported,[57] and in 1992, the CVD protocol for the synthesis of carbon microtubule was described.[58] Since then, extensive reports has been described in literature on the use of CVD as a key tool for the synthesis of single walled[59] and multiwalled carbon nanotubes.[60,61] Dai and coworkers demonstrated CVD protocol for fabricating highly aligned MWNTs and SWNTs on the substrate, using surface—immobilized catalyst nanoclusters.[62] Recently, the CVD technique has also been applied for the large area synthesis of carbon nanotubes which make the utilization of carbon nanotubes in practical applications viable.[61]

1.3.3.1. Vapor—liquid—solid mechanism. Vapor**—L**iquid**—**Solid (VLS) is widely used technique in academic research as well as industry to fabricate thin films, nano whiskers, nanowires, nanorods etc. Figure 1.7. shows the schematic representation of processes occurring at the molecular level. In the VLS process, the carrier gas transports vapors of precursors (solid component), the catalyst is in the liquid state, and the deposition of solid state material takes place, hence it is popularly termed as VLS mechanism. The processes take place at high temperatures, thus the VLS mechanism are employed in accordance with the chemical processes carried out at high temperatures, such as chemical vapor deposition (CVD), molecular beam epitaxy (MBE), laser ablation

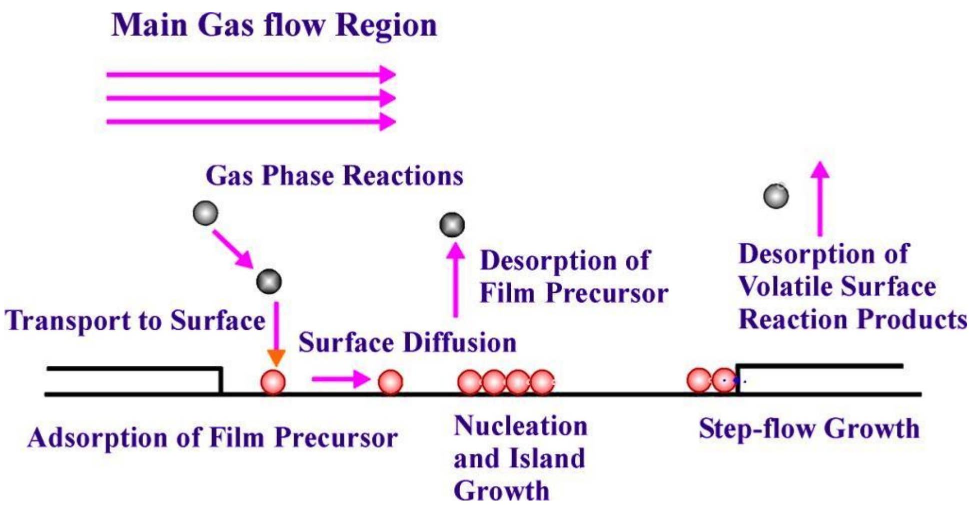

Figure 1.7. Schematic representation of processes occurring at the molecular level during a catalyst assisted chemical vapor deposition.

(LA) and carbothermal reduction (CR). The (VLS) model was first proposed 50 years ago by Wagner for explaining the formation of silicon whiskers in a gas phase reaction in the presence of catalytic gold.[62] The proposed model was based on three observations— (1) requirement of catalytic action of Au for the growth, (2) absence of axial screw dislocations in the whiskers and (3) the occurrence of Au droplet at end of the whisker. Since 1970s, VLS mechanism has been widely used to synthesize different types of whiskers on the micrometer or mm scale. VLS mechanism suggests that the metallic catalyst liquefies at high temperatures and the droplet acts as a preferential adsorption site for precursors in vapor phase. The adsorbed precursors supersaturate the catalyst and subsequently precipitate out as nanotubes/nanowires from the catalyst droplet surface. A continuous supply of precursor vapors is required for the growth of nanostructures.

1.3.3.2. Requirements of metal catalyst. Metal catalyst is the key element in the VLS mechanism. Figure 1.8. shows the 5 processes during the catalyst aided chemical vapor deposition mechanism. Although, not all metals can act as the catalyst for the growth of material, and there are following requirements which should be fulfilled by the catalyst material, (1) The catalyst should be inert towards chemical reactions and form a liquid droplet with a pure component of the solid phase with little/ no contamination in it's composition. (2) The catalyst should have smaller vapor pressure (V_p) as compared to liquid alloy, otherwise during the course of the reaction the catalyst can evaporate affect the reaction progress. (3) It must not make an intermediate solid. Otherwise, the intermediate solid will also deprive it of its catalytic function. The adsorption of precursor in vapor phase on the solid surface is very slow, but in VLS mechanism the vapors are rapidly adsorbed on the liquid catalyst. From this catalytic seed the crystal growth occurs at the liquid—solid interphase. The physical characteristics of nanostructures grown using VLS mechanism largely depend on the size and physical properties of liquid alloy. Figure 1.8 shows the schematic representation of the VLS mechanism, which essentially depends on the sequence of events as follows, (1) Diffusion of Reactants to surface: This reaction step involves mass transfer process. (2) Absorption of Reactants at surface: The metal catalyst forms liquid alloy droplets at a high temperature by adsorbing vapor components. (3) Chemical reaction at surface: The alloy is further supersaturated and it becomes a solution in which the actual concentration of the components is higher than the equilibrium concentration. (4) Desorption of products from surface (5) Diffusion of products from surface. The supersaturation drives the precipitation of the component at the liquid—solid interface to achieve minimum free

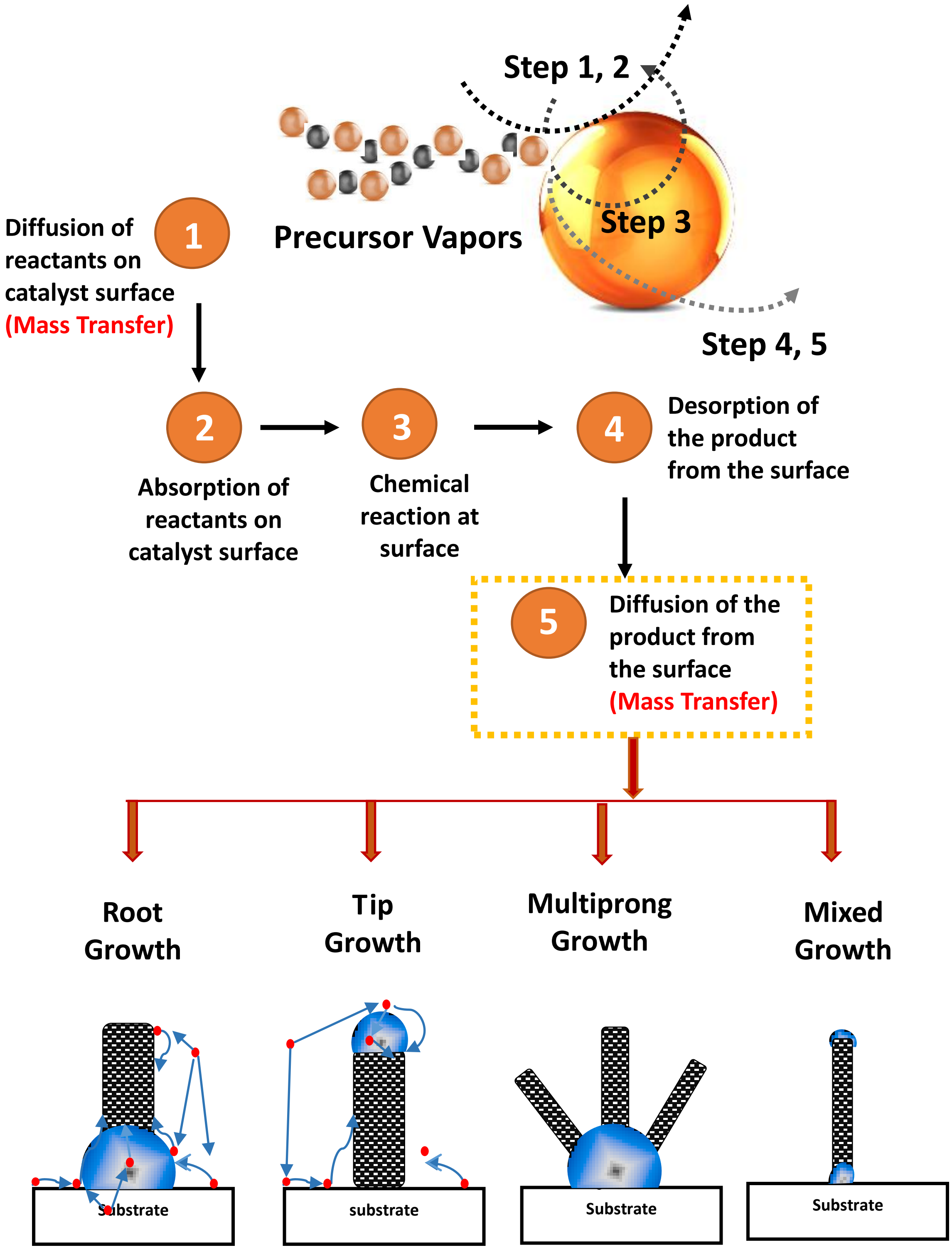

Figure 1.8. Schematic representation of the vapor—liquid—solid mechanism occurring at the surface of the catalyst to produce the nanostructures.

energy of the alloy system. The 1D crystal growth continues as long as the vapor components are supplied.

1.3.3.3. Advantages and disadvantages of bottom—up approach. Liquid phase synthesis method gives the flexibility to control and design the growth of the end product, but varying the operation conditions. Liquid phase synthetic protocols produce nanostructures with homogenous chemical composition and morphology with fewer defects. The major challenge is the separation of the formed nanomaterials from the reaction system. If surfactants are used to assist the growth, it needs one more additional process for the purification of the product, which is not viable for large scale synthesis. The substrate specific growth of the nanomaterials is of prime importance for the fabrication nano—devices, but nanomaterials formed through liquid phase synthesis are difficult to align on specific positions on the chip/ substrates. CVD is highly versatile technique, by examining the precursor—catalyst binary phase diagrams, the temperature range for the VLS growth can be easily determined. The phase diagrams can be effectively used to predict the adsorption, dissolving, mixing, diffusion, and precipitation processes of precursor—catalyst, which helps in designing the CVD reactor. As the metal catalyst is in the form of nanoparticle, the size of the catalyst affects the melting point. As size decreases, melting point also decreases and the catalyst liquefies at lower temperatures compared to that of bulk material, hence the VLS mechanism can be carried out at lower temperatures. The nanowire/ nanotube diameter can be controlled through controlling the diameter of the catalyst used. The nanostructures grow only in catalyst activated areas; hence site specific deposition is feasible. The major disadvantage of the VLS mechanism is the limitations caused because of choice of substrates, precursors and metals. The precursors should be volatile of sublimable which limits the applicability. At the same time the substrate should sustain the operation temperatures which are typically above 500°C. There are limited number of metal catalysts which can be effectively be utilized. The separation of metal catalyst from the formed nanostructures requires repeated washings in acidic solutions, which can degrade the formed material.

1.4. CHALLENGES IN NANOTECHNOLOGY

Since the discovery of Fe—based superconductors, researchers are trying to unfold the mystery behind the mechanism of superconductivity in this newly established superconducting family. The study of superconductivity and magnetism at the atomic scale may lead to deeper understanding of the characteristics and may assist in achieving practically applicable high temperature superconductivity. Thus, it is essential to provide a model system of superconducting nanostructures, which will be beneficial to study the fundamental properties at reduced dimensions. On the other hand, the applications of the nanomaterials has been greatly limited by low signal to noise ratio, complex processes required for the integration of nanomaterials in nanodevice geometry as well as lack of monodispersity of the nanostructures. The research work presented in this dissertation intends to address described challenges in the field of nanotechonology through the following mentioned efforts, (1) Study and analyze the structure—property relationship of the superconducting nanostructures. Not much of the experimental work has been performed earlier to understand the effect of nanoscale geometry on the superconducting transition temperature. The research is focused on establishing the synthesis protocols as well as, examination of the crystal structure in depth to arrive at the conclusion and it presents valuable outcomes which could be helpful for unfolding the mystery behind the superconducting phenomenon observed in Fe—based compounds. (2) Substrate specific growth of the nanostructures. One of the prime requirements for the device fabrication is the alignment of the nanostructures on the substrate to incorporate them in device morphology. The described tool provide an advantage to control the growth of the nanostructures in defined regions along with maintain the structural, elemental integrity as well as homogenous morphology.

2. SUPERCONDUCTING NANOMATERIALS

2.1. FUNDAMENTALS OF SUPERCONDUCTIVITY

Superconductivity is the fascinating phenomenon of the condensed matter physics which is considered as one of the paramount findings of the 20th Century. In 1911 Kammerlingh Onnes,[63] while working to understand the physical property behavior of mercury at very low temperature in his Leiden Laboratory, discovered a strange phenomenon in mercury. In his experiment, the frozen wires were created with mercury in a fine U—shaped glass capillary and at the end of these wires electrodes were attached to measure the resistance at various temperatures. It was observed that, there was sudden drop in the resistivity of mercury as it was cooled down to 4.2 K. Figure 2.1. demonstrates the typical resistivity—temperature curve obtained for the liquid mercury during the experiment. After repeated experiments, it was realized that it was not any experimental artifact but a characteristic of mercury when cooled down below certain *"critical temperature—T_C"*. This characteristic of liquid metal mercury was termed as superconductivity. Extensive research followed this discovery to confirm superconductivity in more than 20 elements in periodic table by 1950.[64] Figure 2.2. represents the periodic table explaining the superconductivity nature in various other elements of the period table.[64]

2.1.1. Classification of Superconducting Materials. In the periodic table there are thirty pure metals which exhibit superconductivity, these are called as Type I superconductors. The mechanism of superconductivity in Type I superconductors can be well described by the BCS theory. On the other hand, the superconductors fabricated from the alloys of metals are called as Type II superconductors. Type I and Type II

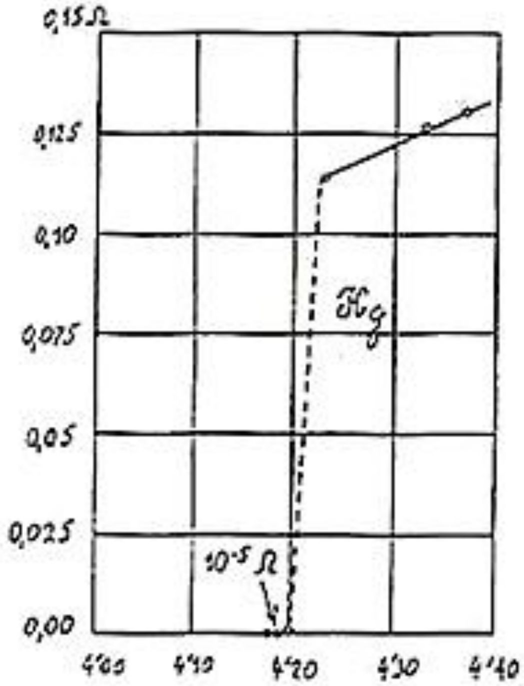

Figure 2.1. Historic graph showing the superconducting transition of mercury, measured by H. Kamerlingh Onnes.[1]

superconductors are also called as *soft* and *hard* superconductors, owing to the evident difference between their magnetic and current carrying properties. Type II superconductors are mechanically stronger and exhibit higher current carrying densities than Type I superconductors, which limits the applications of Type I superconductors. These two properties make them viable to use in practical applications. For example since 1960s two principle superconducting materials, niobium – titanium (Nb—Ti, Tc) and niobium – tin (Nb_3Sn, Tc = 18K, high critical current densities)[64] are utilized in practical wire wound magnetic applications.

Other classification of superconducting materials is based on oxide— ceramics, and Fe—based superconductors. Fundamentally, ceramic based materials are expected to be insulators, but 1986, George Bednorz and Alex Muller discovered superconductivity in LaBaCuO at Tc= 30K.[64] This was followed in early 1997 by the announcement of a cuprate superconductor $YBa_2Cu_3O_{7—x}$ with transition temperature above 77K, the boiling point of liquid nitrogen, by C. W. Chu.[65] Extensive research followed this discovery and led to the development of the field of Cu based superconductors with superconducting T_c as high as 125 K in $Ti_2Ba_2Ca_2Cu_3O_{10}$.[66] In these ceramics, the superconducting state is achieved at much higher temperatures and the class of materials is often referred to as High Temperature Superconductors (HTS). For type I superconductors, it is required to bring down the operating temperature below nitrogen temperature and use of helium becomes unavoidable which restricts the practical applicability of low temperature superconductors. But, oxide based superconductors has one major disadvantage of low critical field (Hc). That means the superconductivity is destroyed under very low external magnetic field. This shortcoming restricts the use of HTS in devices such as generators, motors, power accumulators where high critical field characteristics of a superconductor are required.[64]

2.1.2. Characteristics of Superconductors. Superconductors are the exotic class of materials which show zero resistance to the conduction of current below the specific transition temperature. There are certain unique physical attributes of superconductors described as follows:

The **Meissner Effect** demonstrates that the superconductors are more than just perfect conductors and provides an exclusive characteristic of the superconducting state. In 1933, Walter Meissner and Robert Ochsenfeld while experimenting to understand the effect of superconductivity on the external magnetic field below critical temperature validated that the magnetic field was expelled by the superconductor,[64,67] this behavior was termed as Meissner effect. When the material ‘superconducts’ there are electric currents which run across it’s surface called as ‘screening currents’. The screening currents actually shade the interior of the superconductor from the externally applied magnetic field. They also produce magnetic field at the external surface of the superconductor which acts opposite to the applied magnetic field and repels the external magnetic field.[2]

Owing to the Meissner effect the superconductor exhibits perfect diamagnetism below Tc, and the diamagnetic nature is an important parameters for the characterization of superconductivity. Thus the magnetic susceptibility $\chi = -1$. One of the theoretical explanations of the Meissner effect comes from the London equation. The discovery of the Meissner effect was paramount and it was accounted in the theoretical ‘London Equation’ by Fritz and Heinz London in 1935.[68] The London Equation explains the current density of superconductor j to the magnetic vector potential and it demonstrates that the magnetic field caused by the screening currents decreases over a particular distance near the surface. This distance is described as ‘**London Penetration Depth**’.[68] Every superconducting material contains a characteristic penetration depth, usually in the range of 20—40 nm.[68] **Zero Resistance to Direct Current:** As the name suggest, every ‘SUPER’ conductor shows zero resistance to the flow of current at all temperatures below Tc. The resistivity of a superconductor is less than 10^{-23} Ω.m which is 15 orders of magnitude less than the resistivity of Cu at room temperature[69] (Resistivity of Cu at 20° ≈ 1.68×10^{-8} Ω.m).[70] Owing to this fascinating property of superconductors, they are widely used in practical applications such as electromagnets for the generation of high magnetic fields, power lines, NMRs, MRI instruments etc. The **critical current**, I_c of a superconductor is the maximum current a superconducting material can carry before losing its superconductivity. The critical current per area (cross—sectional area of the wire, tape, thin film or material of interest) of the superconducting material gives the critical current density (J_c) of the superconductor. Thus, higher critical current gives rise to higher current carrying capacity and lower amounts of superconducting material.

2.1.3. Present and Future Applications of Superconductivity. Superconductors play an immensely important role in medical diagnostic science as well as industrial processes. Superconductors are extensively being used in current commercial applications such as Magnetic Resonance Imaging (MRI), Nuclear Magnetic Resonance (NMR), High—energy physics accelerators, and industrial magnetic separation of kaolin clay. In the mentioned field, the low temperature superconducting materials are being used to produce very high magnetic fields. The use of iron wire based electromagnets are limited to applications in generators, motors owing to the limitation in the generation of magnetic field strength of 1.8 T, on the other hand superconducting electromagnets can generate magnetic fields as high as 33T. Superconductors are environmental friendly and provide clean source of power and efficient electricity. Many of the European and Asian countries rely on MagLev – Magnetically levitating trains for the transportation. As the superconductors provide a resistant free flow of current, an extensive research is being carried out currently in the field of superconductors as interconnects in microprocessors to address the problem of joule’s heating in micro—chips.

2.2. Fe BASED SUPERCONDUCTORS

The timeline for Fe—based superconductor research, sometimes referred to as "*the iron age of superconductivity*" started with the discovery of superconductivity in an unexpected compositions, LaFePO and LaNiPO by Hosono's group in 2006.[71,72] Following this discovery superconductivity was reported at 26 K in the fluoride doped iron oxyarsenide, $LaFeAsO_{1—x}F_x$,[73] which stirred up research interests in this field as each of the months following the discovery witnessed the T_c in this family of compounds climbing up the ladder[74] culminating in a T_c of 57 K for $Sm_{0.95}La_{0.05}O_{0.85}F_{0.15}FeAs$.[75] To date this is the highest T_c reported in a non—cuprate based superconductor. This family of compounds is generically referred to as *LnMPn*O (*Ln* = rare—earth, *M* = transition metal ion, *Pn* = pnictogen ion) or the [1111] series based on the stoichiometry of the ions. These compounds are seen to have a very forgiving composition and the rare—earth atom can be varied within the *Ln* series, while the superconductivity is retained. The T_c was boosted up from 26 K to 55 K in a matter of days simply by changing the rare—earth atom from La to Sm. The presence of superconductivity in iron based compound itself is fascinating because iron is more popularly known for having magnetic ordering, which does not preferably coexist with superconductivity. Hence researchers continued the search for new superconducting compositions in these iron pnictides, and pretty soon two new families of compounds were identified as a new class of superconductors. The family of compounds generically referred to as [122], is exemplified by $BaFe_2As_2$ (T_c ~ 38 K) and substituted compositions.[75,76] The second family of superconductors containing iron pnictide as the basic backbone, has an even simpler composition, generically referred to as [111] family, and exemplified by LiFeAs.[77,78] These new family of superconductors are now collectively referred to as the pnictide superconductors, with the generic formula, [1111] (*LnMPn*O), [122] ($BaFe_2As_2$) and [111] (LiFeAs).

It was observed that all these pnictide superconductors have a crystal structure which was derived from the simple layered arrangement of the Fe_2As_2 anionic layers alternately stacked with the cationic layers/ions. The [1111] *LnMPn*O series of compounds crystallize in the tetragonal space group (*P*4/*nmm*) with ZrCuSiAs structure—type.[71-78] The structure can be described as layers of edge—shared MPn_4 tetrahedra alternating with layers of edge—shared LnO_4 tetrahedra (Figure 2.2.a). While the *M*—*Pn* bonds are more covalent, the *Ln*—O bonds are ionic and because of this, a distinctively two—dimensional structure forms, whereby, the ionic layers of *Ln*—O alternate with the covalently bonded layers of *M*—*Pn* along the *c*—axis. One characteristic and distinctive feature of the *M*—*Pn* layer is that, there is an overlap between the valence shell *d*—orbitals of the transition metal, thus making these compounds good metallic conductors at room temperature. Studies have shown that the superconductivity in this family arises from the covalent layer. Hole doping in the $Ln^{3+}O^{2-}$ layer transfers the charge carriers to the $M^{2+}Pn^{3-}$ layers, which gives rise to "natural modulation doping", like the high—T_c cuprate superconductors leading to enhancement in T_c. The structure of the [122] pnictide superconductors can be derived from the [1111] series simply by replacing the *Ln*—O layer with divalent Ba^{2+} cations (Figure 2.2.b). Similarly in the [111] series the Li ions occupy the interstices in between the FeAs layers (Figure 2.2.c).

Following the discovery of superconductivity in the rather inconspicuous series of compounds, namely, the layered iron pnictides, it was hypothesized that the iron pnictide layer was the one responsible for superconductivity, while the cationic layer functioned as the charge reservoir layer. Very recently, this hypothesis gained even stronger grounds when superconductivity was discovered in the binary Se deficient PbO—type tetragonal iron selenide, $FeSe_{1—x}$ at ~8 K,[79] where, the structure built up by stacked layers of interconnected $FeSe_4$ tetrahedra, was very similar to the iron pnictide layers in *LnMPn*O (Figure 2.3.a). This paved the way for a series of chalcogenide superconductors similar to the pnictides exhibiting moderately high T_c. In this chalcogenide superconductor, the T_c could be varied by substituting the chalcogenide anion and the highest T_c of 14K is obtained in the optimally doped $FeTe_{1—x}Se_x$ ($0.5<x<1$).[80] These compounds are derived from the FeSe structure simply by placing the alkali metal cations like K in between the anionic FeSe layers (Figure 2.3.b). The structure of FeSe is the simplest among the iron

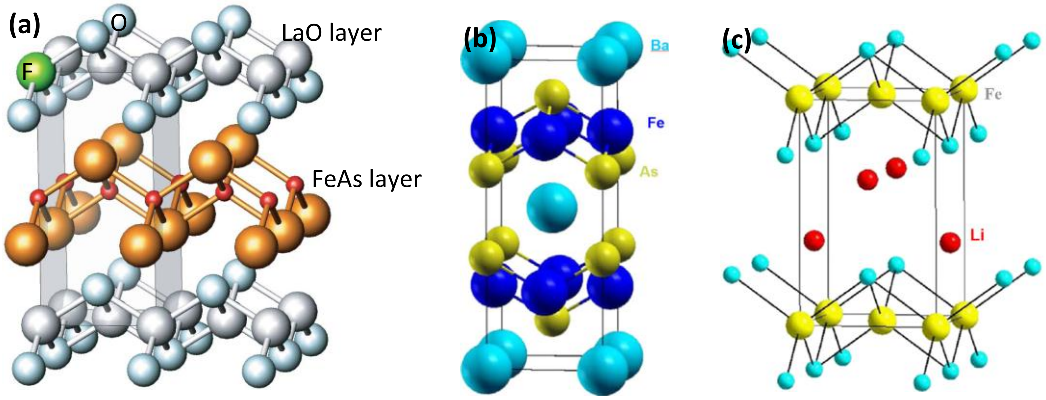

Figure 2.2. Representative crystal structure of the *pnictide* superconductors: (a) $LaFeAsO_{1-x}F_x$ (red – Fe, brown – As, blue – La) [Adapted from ref 4]; (b) $BaFe_2As_2$;[14] (c) LiFeAs.[16]

based superconductors. Moreover, theoretical studies indicate the similarity between the electronic structure of the iron chalcogenide and pnictide superconductors. As a result of their common natures, the simple FeSe superconductor is being considered as a key element to elucidate and understand the mechanism of iron based superconductivity.

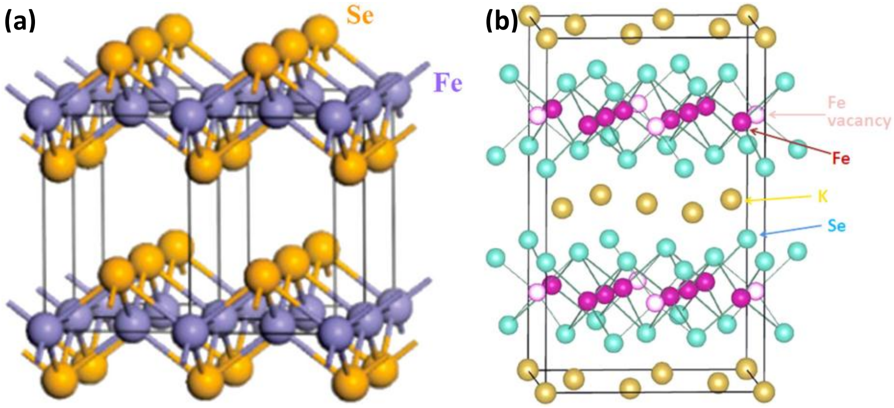

Figure 2.3. Representative crystal structure of the *chalcogenide* [Fe*Ch*] superconductors: (a) tetragonal FeSe;[18] (b) $K_{0.8}Fe_{1.6}Se_2$.[20]

Fe—based chalcogenide superconductors have an even larger significance from the technological aspect, primarily because the T_c in these compounds is almost 30 K warmer than the most widely used superconductors, [Nb_3Sn, T_c = 23 K; NbTi, T_c = 10 K], which means that the devices would be more cost—effective and efficient. Apart from having a significantly higher superconducting T_c in a simple binary composition, these Fe—based superconductors are also characterized by a high critical current density, making them very attractive for potential applications. However, the potential for actual use of these superconductors was still somewhat uncertain, since intrinsic electronic properties might affect the application range. For example, extreme electronic anisotropy prevents the effective pinning of vortices and limits the critical current density, a problem frequently encountered in cuprates.[81] As a comparison, the critical current density of the some commonly used superconductors, (NbN, Nb_3Ge), MgB_2 and the pnictides is higher and can be used effectively for practical applications.[82-94] Reduction of compositional complexity of the newest superconductors, significantly increases their applicability, especially with the binary and ternary superconductors like FeSe and LiFeAs.

2.3. EFFECT OF PRESSURE AND NANOSTRUCTURING ON THE TRANSITION TEMPERATURE

The T_c in the Fe—based superconductors is very pressure sensitive and shows an enhancement in the [1111],[94] [111][95] and the [122] families.[96] However FeSe shows the most dramatic positive pressure dependence of T_c amongst all the Fe—bases superconductors.[97,98] The T_c in FeSe is increased to 37K under an applied pressure of 4 GPa, which is the third highest T_c among the binary superconductors (after 39K in MgB_2[99]and 38K in Cs_3C_{60}[100]). According to Cava and his co—workers as the pressure increases, the FeSe layers are brought closer together, leading to denser structure which is instrumental in increasing the T_c.[36] Such T_c enhancement have been observed in the $FeTe_{1—x}Se_x$ also, but not so profoundly.[101] Pressure can be applied as external physical pressure or as chemical pressure by doping and even internal pressure by creating lattice strain. Confinement of the material into nanostructured geometry creates some strain which might translate as internal pressure points. Additionally, the iron based superconductors by virtue of their unconventional nature is expected to show a change in their magnetic and electronic properties on nanostructuring thereby affecting their superconducting properties.[102] Hence, the current focus in these chalcogenide superconductors is on nanostructuring and morphology controlled growth.

2.4. SUPERCONDUCTING NANOSTRUCTURES

As the advances in technology promotes miniaturization of devices, the prospect of using the 1D nanostructures, nanowires and nanotubes, as interconnects and functional components in these tiny length scales, is now better than ever. Recently there have been several reports where the nanowires have been tested and used as an integral part of functional device.[103-105] Superconducting nanowires are attractive from the technological point of view for many reasons. One of the most straightforward advantages is that, since below the transition temperature (T_c) the material can support resistance—less flow of current, nanowires can be used as low—dissipation interconnects in the nano—scale devices. While, it has been reported that superconductivity can be suppressed in ultrathin nanowires of simple elemental and alloy superconductors due to thermal and quantum phase slips,[105,106] the critical current on the other hand increases significantly with decreasing diameter of superconducting nanowires.[107,108] Theoretical studies on finite size effects in pnictide superconductors have led to the hypothesis that both critical current and T_c can be affected in low—dimensional structures.[109] Also recent reports show that the critical current can be increased manifold in superconducting nanowire arrays, making them promising candidates for carrying high levels of low—dissipation current.[110] This would be even more attractive for the Fe—based superconductors since they inherently

3. FABRICATION OF NANOWIRE ARRAYS ON SUBSTRATES

3.1. SUBSTRATE SPECIFIC GROWTH OF NANOWIRES AS ARRAYS

In recent times, device miniaturization has led to an intense research in the field of designing nanostructures over substrates in well—defined regions. The physical properties of the nanostructures intensely depend on the electron transport across the nanowires and at the nanowire electrode interface. These two factors define in large the effectiveness of the semiconductor nanowire device. Poor contact at the nanowire electrode interface leads to large Schottky barrier and huge contact resistance across the interface thus giving rise to inhibited transpot,[111] hence; there is a renewed interest in the exploration and development of new assembly methods for integration of nanowires. The growth of nanowires on a substrate is highly advantageous in this regard since it confines the region of growth and also by adopting suitable bottom—up growth techniques, high densities of nanowires can be grown over any defined region. Individual nanowires assembled as arrays, provide greater surface area of material—electrode interface. The semiconducting nanowires as arrays possess potential applications in photovoltaic devices like solar cells and thermoelectric devices. The use of hard templates like the anodic aluminium oxide (AAO) which contains ordered arrays of columnar pores has been widely used to grow nanowire arrays. Similar methodology has also been adopted to grow nanowires through electrodeposition inside the pores of the template.[112,113] Though this method produces assembled arrays of monodisperse nanowires of uniform composition; it possesses some of the disadvantages. (1) The template removal requires etching of the alumina in a highly basic or acidic solution. This harsh chemical treatment could lead to the degradation of formed nanowires by changing the chemical composition through hydrolysis under basic conditions or decomposition in acidic conditions.

(2) The presence of alumina backbone that defines the pores requires a rigid substrate for maintaining structural integrity; hence the method is not applicable on the flexible substrates and thus lacks versatility required for modifications. The size of the grow

Figure 3.1. demonstrates the current research idea which has been implemented with a vision to develop a generalized protocol to grow ordered arrays of nanowires at patterned regions on substrates, specially targeted towards creating efficient photovoltaic and superconducting devices. The substrates were modified using electron beam lithography such that it created nanoelectrodes and confined growth within the nanochannels would lead to nanowires. As demonstrated in Figure 3.1. the growth regions defined on the substrates through lithographic techniques has been used to

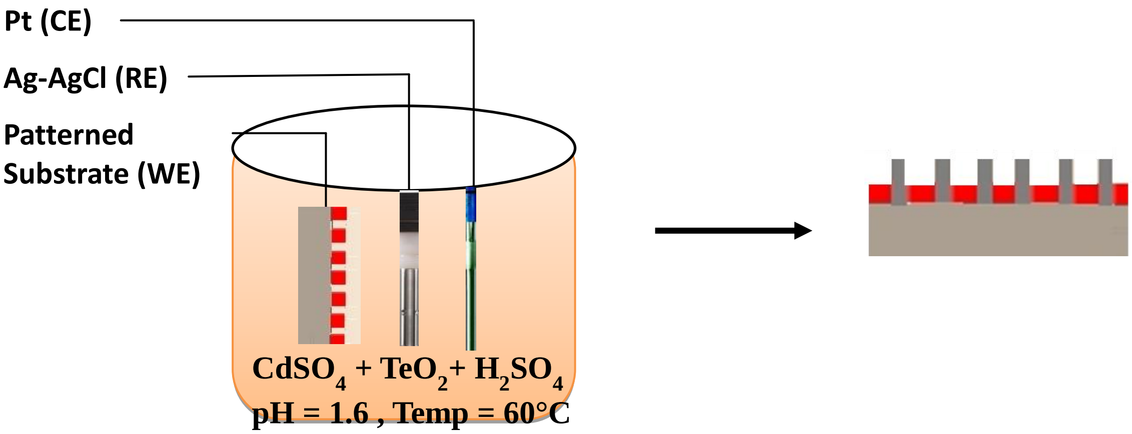

Figure 3.1. Schematic description of the research protocol used for the fabrication of nanorod arrays on substrates by combining electron beam lithography and electrochemical deposition

deposit thin layer of the material of interest through electrochemical deposition. The aim of this research was to explore and design various methodologies to grow assemblies of nanowires, and study the effectiveness of the approach in terms of reproducibility, enhanced signal—to—noise ratio and scalability. Electrodeposition is a simple yet novel method that offers versatility with respect to the materials that can be deposited. Also, it is a cheap and scalable method producing reproducible results, which is ideal for device fabrication.

3.2. TECHNICAL CHALLENGES ENCOUNTERED AND THE PRACTICAL SOLUTIONS

As described earlier in the introduction section, electron beam lithography is able to provide a high resolution patterning and utilized widely in semiconductor industry to fabricate chrome on glass masks for photo lithography. The fine focused beam of electron carried significant amount of energy and when it interact with the surface of the substrate/ resist, it generates a variety of signals. The electron beam having intensely high kinetic energy penetrates the atoms and decelerates eventually in the solid sample. In this process, secondary electron signal, backscatter electrons, X—rays, cathodoluminescence, photons, and heat signals are generated. (Figure 3.2) During lithography, these produced signals can affect the resolution, speed and accuracy of the lithography significantly. The wavelength of the electron is small (3.70 pm, for electron beam at 100 KeV), and thus the diffracted electron beam does not affect the resolution. But, the resolution is limited by the chromatic and spherical aberrations, as well as scattering of the electrons in the resist and substrate. The electron beam lithography parameters, such as beam voltage, beam energy (current), maximum dosage of the electron beam, dwell time, vibrations in the surrounding area can affect the resolution and performance to a larger extent. And manipulating these characteristics is the major challenge while establishing a lithography protocol. The writing of the desired pattern suffers significantly due to the variations in these parameters as explained in Table 3.1. In the next section, technical problems encounter during the electron beam lithography experiments has been explained and the solutions which were employed are discussed in detail.

Table 3.1 Table demonstrating the electron beam lithography parameters.

Parameter	**Process Impact**
Exposure Energy	**Resolution, sensitivity, proximity**
Exposure dose	**Pattern quality**
Pattern density	**Proximity, pattern quality**
Resist material	**Sensitivity, resolution, contrast**
Resist thickness	**Sensitivity, resolution, pattern quality**
Developer	**Sensitivity, resolution, development window**
Development temperature	**Sensitivity, resolution, exposure window**
Development time	**Sensitivity, resolution, exposure window**

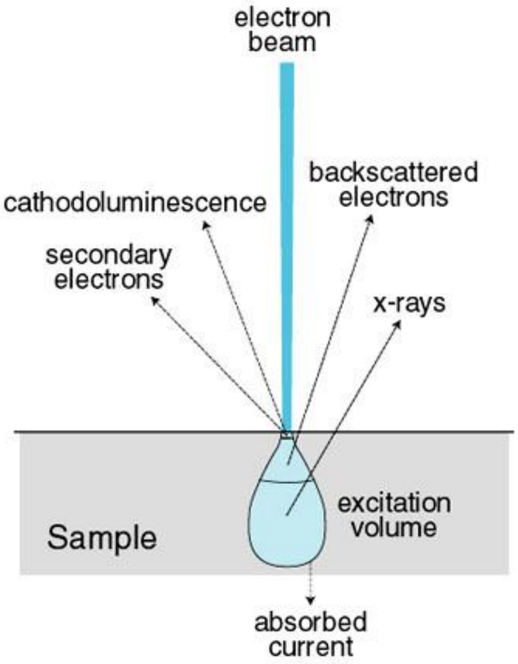

Figure 3.2. Electron—solid interaction model.

3.2.1. Over—Exposure of the Electron Beam. When the electron beam is induced on the positive PMMA resists, due to the high energy of the beam the molecular chains in the resist molecules will break effectively reducing the molecular weight. The solubility of polymer from these regions will be high and could be dissolved easily using developing solution. When the beam is over—exposed it affects the feature size of the pattern. Figure 3.3. demonstrates such an instant of over exposure of the electron beam. Further experimentations were carried out to set—up appropriate beam voltage and current i.e. correct beam exposure time.

3.2.2. Astigmatism In order to achieve accurate feature size and shape the electron beam should be circular in cross section when it is induced on the resist. Due to various factors of the electron column, such as presence of layer of impurities (carbonaceous matter) on the pole piece, imperfections in the castings of the iron magnets

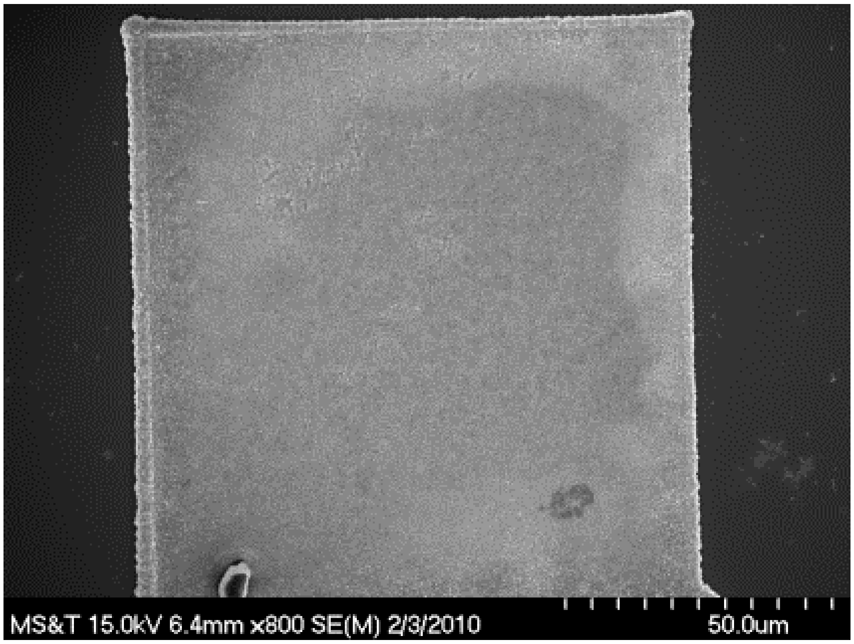

Figure 3.3. SEM image of the failed e—beam lithography experiment, showing the patterned region of a block, contrast to the spherical structures.

and copper windings, the beam cross section gets distorted to form an eclipse. This condition lead to the difficulties in focusing and it is termed as ‘astigmatism’. Bad astigmatism can be observed as "streaking" in either X direction or Y direction, as the image passes through focus from under focus to over focus. Figure 3.4 demonstrates the SEM image which shows the patterns suffering from astigmatism problem. It could be clearly observed that the circular features are elongated in one direction. To correct the stigmatism issue, the standard spherical ‘Sn beads’ sample was used. An accurate stigma and focus correction was performed, before the lithography, using X and Y stigmator knobs at stage height= 4 mm. These adjustments allowed the manipulation of the beam shape and assisted to correct for major lens distortions.

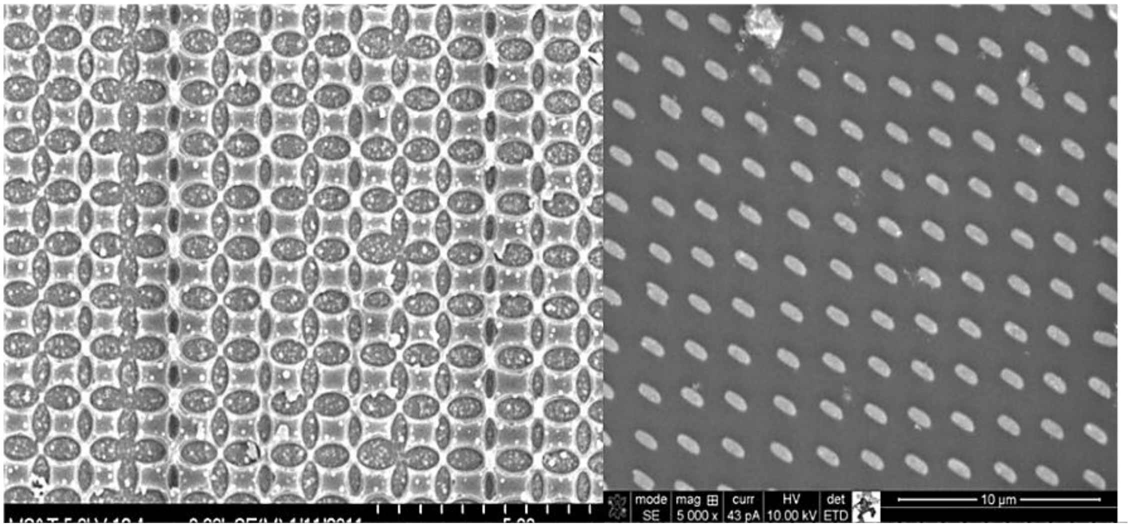

Figure 3.4. SEM images of the e—beam lithography experiment, showing the astigmation effect of the electron beam.

3.2.3. Proximity Effect. The scattering events occurring after the exposure of the beam on the substrate are the major cause of damage to the patterns. There are two types of scattering events, forward scattering and backscattering. Backscattering is the elastic scattering, in which the electrons retain their energy but the changes the direction and deflect through a large scattering angle. In such case, the electrons revert back to the surface through the resist, at a distance away from the incident beam. Thus scattering leads to an influence in the regions adjacent to those exposed by the electron beam. This condition is termed as ‘proximity effect’. Figure 3.5. demonstrates the schematic representation of the proximity effect, where the electron beam is intended to expose at the region of pixel—A, but as a result of proximity effect the pixel—B also get exposed by electrons and in turn affects the pattern. Once the proximity effect is observed in the pattern, additional manipulation of parameters becomes essential to reduce the scattering, so that the electrons can easily penetrate the resist layer and substrate.

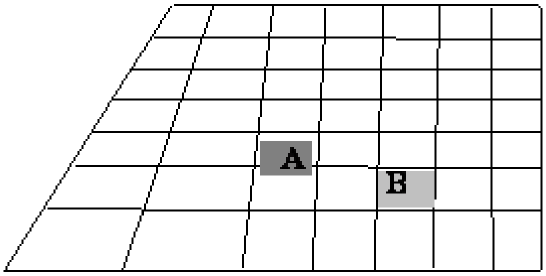

Figure 3.5**.** Proximity effect: exposure at pixel A affects pixel B.

Figure 3.6 demonstrates the SEM image showing the occurrence of proximity effect, represented by the red dotted circle. In order to correct the proximity effect, the experiments were carried out for the dose modulation. It was essential to decrease the dose of the electrons, thus, the thickness of the polymer was also reduced in order to assure the sufficient amount of exposure. Theoretically, lowering the beam voltage can

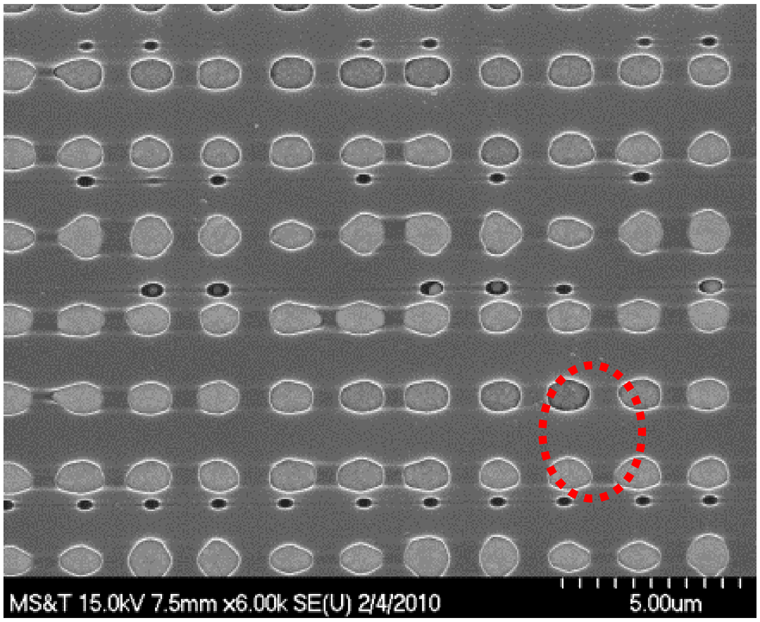

Figure 3.6. SEM image demonstrating the proximity effect in the patterned region.

also help in reducing the proximity effect, but, in our case the voltage was kept constant at 30 KeV to ensure the provision of high energy of electrons to keep the time of writing optimum. In cases, multiple layers of the resists are also utilized; also, the shape corrections are performed using mathematical modeling to counteract the proximity effect.

3.2.4. Vibration Noise/ Instability of the Beam. Electron beam lithography is very susceptible to acoustics, temperature fluctuations, humidity, floor vibrations, and these parameters affect the output results. For best results, particular operational practices were followed, such as avoiding leaning on the desk after the lithography has initiated, avoiding walking on the floor to keep the operation of the room devoid of vibrations. Figure 3.7 shows the SEM image of the lithography patterns affected by the vibrational noise of e—beam. Carrying out the lithography experiments for long time makes the system vulnerable to beam drifts and instability. Also, unstable beam current was

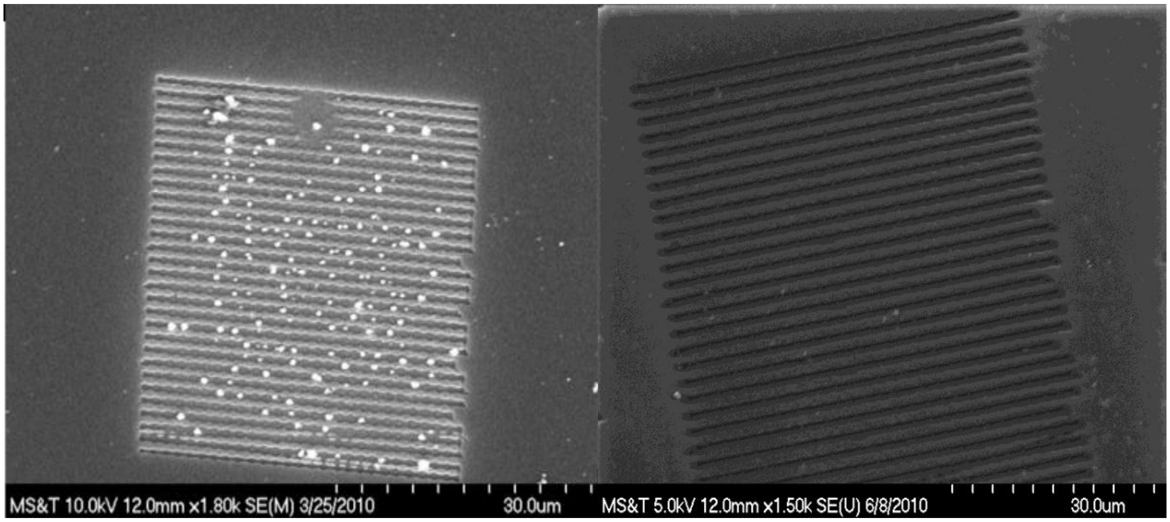

Figure 3.7. SEM image showing the occurance of the '*curly*' pattern as a result of instability of the beam.

observed to affect the feature patterning. size of the pattern. It was observed that keeping the electron beam on for about 15—20 minutes to stabilize the beam current, the problem was alleviated.

3.2.5. Excessive Charging. As the resists layer is composed of insulating PMMA polymer matrix; it causes the accumulation of electrostatic charge at the resist surface, due insufficient provision of grounding. During lithography, significant pattern displacement occurs due to charging at the resist surface causing deflection of the electron beam path. Figure 3.8 demonstrates the SEM image which shows the deflection of the patterns caused by the charging of the polymer resist surface. To address this issue, a thin layer (≈10 nm) of Au—Pd was sputter coated on PMMA prior to the lithography.

3.2.6. Longer Time of Writing It was observed that, the initial lithography experiments required longer electron beam exposure time and required more than 60 minutes to finish writing of one pattern. The amount of time consumed for one

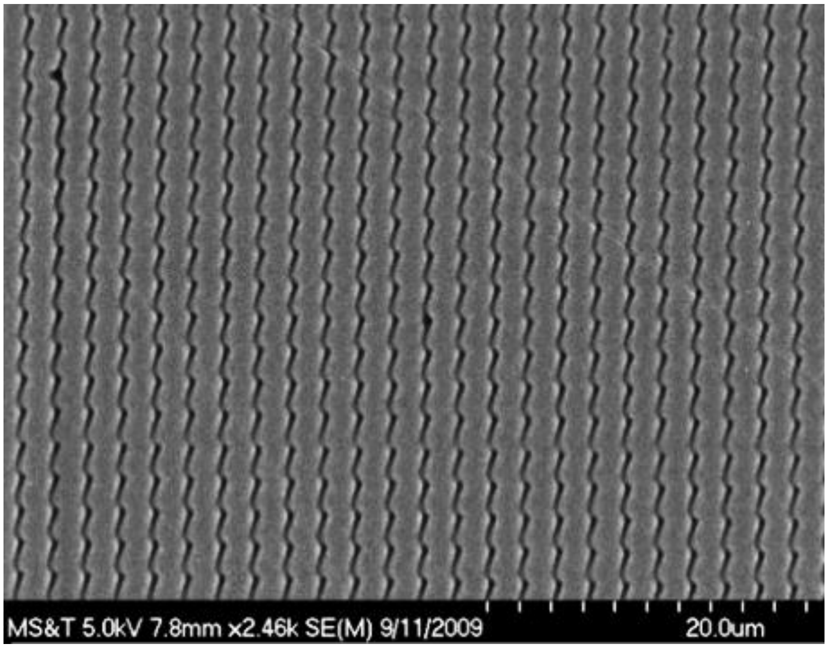

Figure 3.8. SEM images demonstrating the charging effect on the e—beam lithography

lithography pattern was unacceptable and not feasible for practical application to the project. Hence, modifications to the original lithography mask design were carried out in order to reduce the time. The time factor largely depends on the thickness of the polymer as well as the pixel size of the mask design. Smaller pixel sizes are necessary to obtain an accurate image and provide better resolution. However, small pixels with the point exposure profile requires long exposure time, thus the initial mask design pixel size was reduced from 4000×4000 pixel to 1500×1500 pixel. As the required feature size was 400 nm, hence increasing the pixel size did not affect the resolution to larger extent, but it could considerably reduce the time from 60 minutes to 54 seconds.

3.2.7. Inaccurate Development Time For the accurate development time in the solvent, it is essential to understand the three dimensional distribution of beam in the resist during the exposure. Insufficient etching through shorter development time may not remove the e—beam exposed polymer completely, which in turn lead to the formation of under—cut phenomenon. While, over—etching can remove the excess of the polymer from the substrate forming an over—cut. The concentration of the solvent also plays a crucial role in determining the development time. Figure 3.9 demonstrates the SEM image of the pattern developed for the excess time. Based on this observation, the concentration of active ingredient Methyl isobutyl ketone was reduced in the formulation and set as MIBK:IPA 1:1 v/v ratio. The development time was also modulated to

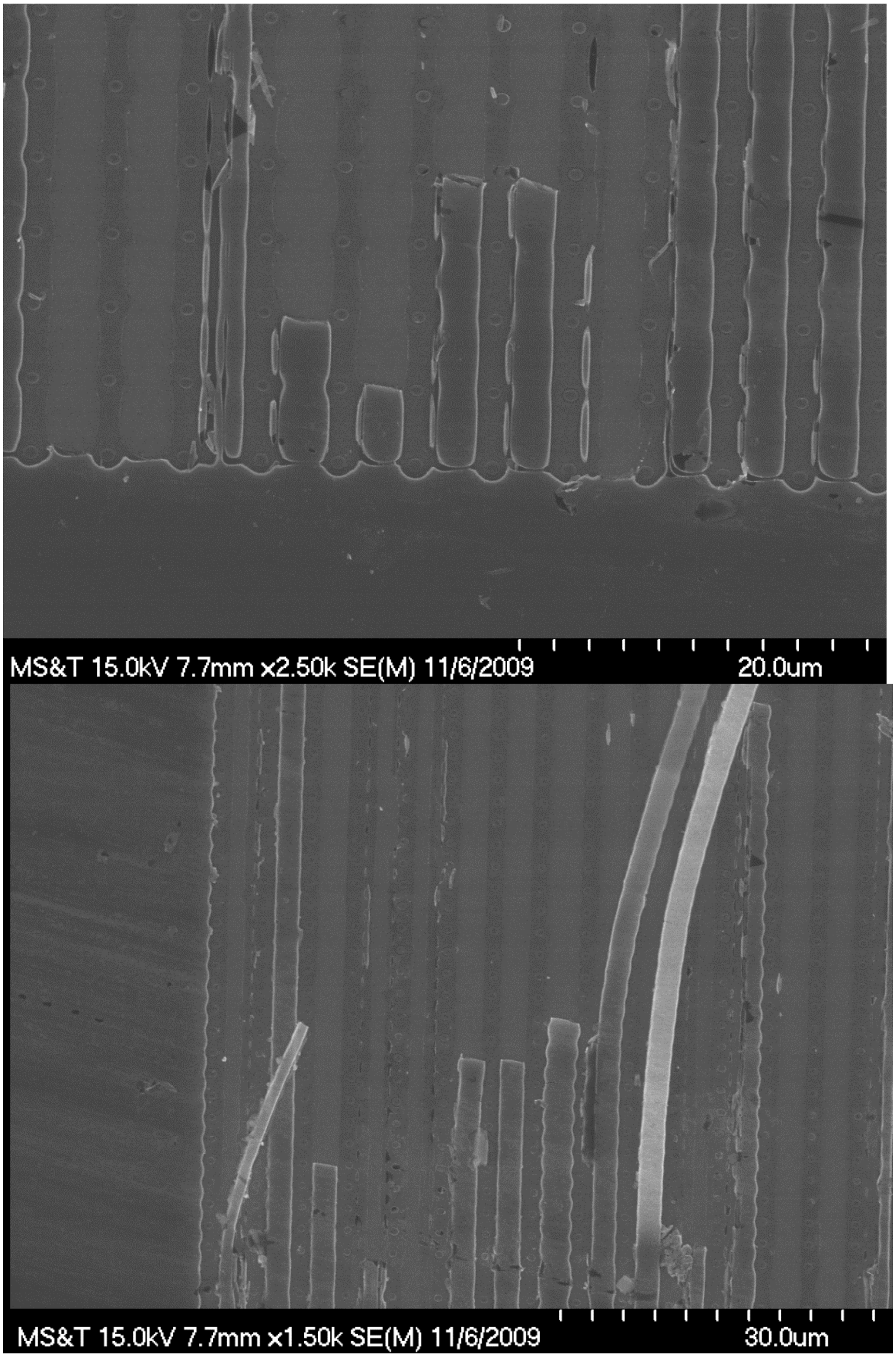

Figure 3.9. SEM images demonstrating the pilling of PMMA resist owing to the over—exposure of pattern to the developing solution.

4. MULTIFUNCTIONAL NANOSTRUCTURES

4.1. OVERVIEW OF MULTIFUNCTIONAL NANOSTRUCTURES

Multifunctional nanostructures consist of two or more components with distinctly different functionalities, sharing a common interface. These nanoparticles possess wide spread applications and can be used effectively in biomedical, diagnostic, therapeutic and catalysis applications. Magnetic nanoparticles are thoroughly explored and analyzed for their role in diagnostic and therapeutic applications. Magnetic nanoparticles having diameters less than 20 nm produce high saturation magnetization, leading to the superparamagnetic state at room temperature. In the superparamagnetic state, the magnetization of the nanoparticles can be saturated with external magnetic field. The absence of external magnetic field produces zero magnetization under thermal agitation. Due to these magnetic characteristics, and size comparable to the biologically critical objects, the monodispersed magnetic nanostructures (nanoparticles, nanocrystals, nanorods) such as FePt,[114] CoPt,[115] Fe_2O_3,[116] Fe_3O_4,[117] γ— Fe_3O_4[116] have been explored for applications in MRI contrast agent,[5] bioseparation, targeted drug delivery,[117] pathogen detection, or protein separation.[117] The combination of the features magnetic nanoparticles and metallic nanoparticles, in the form of core—shell, dumbbell shaped nanoparticles have been proved to be very effective. Owing to the excellent size tunable optical properties, metallic Ag, Au, Pt nanoparticles are critical component of multifunctional nanoparticles. The metallic nanoparticles functionality serve as optical contrast agents, multimodal sensors and photothermal therapy.[118,119] One of the constructive assemblies include nanostructures containing semiconducting properties leading to fluorescence combined with magnetic nanoparticles. The examples of such assemblies includes nanostructures such as FePt—CdS nanoparticles,[120] γ—Fe_2O_3/ZnS,[121] FePt—ZnS nanosponges,[122] Fe_2O_3 bead—CdSe/ZnS[123] quantum dot nanocomposites, Co@CdSe core—shell nanocomposites.[124]

There is plethora of reported methods for the synthesis of multifunctional nanoparticles. The most popular synthesis method is the solution based synthesis, where one component of the multifunctional nanoparticles is synthesized first and utilized as a primary seed in the reaction.[124] The other functionality particle grows surrounding this primary particle, providing core—shell morphology. This kind of synthesis methods possesses advantages of selection of functionalities and designing of the variety of components in desired architecture to produce multifunctional nanostructures. J. Gao and coworkers demonstrated synthetic methodology for fabricating core—shell, FePt@CdX (X=S, Se) nanoparticles through manipulation of the order of reagent addition in the solvent assisted one pot synthesis method.[125] The FePt region acts as a magnetically active superparamagnetic particle while the CdS/CdSe component can generate fluorescence. In the reaction protocol the magnetic FePt nanoparticles were synthesized first and reacted with $Cd(acac)_2$, which acted as a source of Cd. These initial steps were followed by the addition of elemental Se/S as a source of chalcogenide.[125] These nanoparticles were further characterized for the magnetic properties of FePt showing the blocking temperature at 9K and optical properties of CdSe/CdS through UV—Vis and Fluorescence spectroscopy.[125] Bawendi and coworkers, engineered the synthesis protocol for fabricating optically active multifunctional nanoparticles assembly by synthesizing semiconducting $InAs_{0.66}P_{0.33}$ and InAs nanoparticles, and utilizing them as seed particles in the further reaction.[126,127] In these studies, they demonstrated the synthesis of water soluble core—shell, InAs(ZnCdS) quantum dots demonstrating constant and intense emission at near—infrared region applicable for biological imaging.[128] The formed nanoparticles were successfully utilized to image tumor vasculature through in—vivo studies.[128] In other studies, a complex assembly of core—shell—shell quantum dots with alloy core of $InAs_{(1-x)}P_x$, coated with InP shell and ZnSe as final outer shell, has been synthesized.[16] The $InAs_xP_{1-x}$ demonstrated an emission in the near—infrared region, InP shell contributed to a red—shift and the ZnSe shell imparts provides stability in aqueous medium. The core—shell—shell quantum dots, dispersed in aqueous media have been successfully utilized in near—infrared lymph node mapping.[129] Simple, reproducible methodology for the synthesis of superparamagnetic Fe_3O_4—Au nanospheres has been reported, which utilized pre—synthesized Fe_3O_4 nanoparticles.[130] Core—shell nanostructures of FePt—ZnO have been synthesized successfully through a seed—mediated growth mechanism, where FePt nanoparticles were used as a primary seed synthesized from $Fe(CO)_5$, $Pt(acac)_2$ and then further reacted with $Zn(acac)_2$ precursors to synthesize ZnO shell.[131] These solution based synthesis protocols contain certain disadvantages. As the synthetic protocols contain multi—step process, there is an increase in the processing time. The separation of the product after the completion of the reaction also imparts difficulties. On the other hand, though chemical vapor deposition technique has been explored extensively for thin film deposition, epitaxial growth, nanowires/nanoparticles synthesis, very few reports have been described in the literature which could fabricate multifunctional nanoparticles. Chemical vapor deposition technique possesses tremendous potential to address the problems encountered in the solution base synthesis by fine tuning the reaction parameters. Hence, it is necessary to investigate the chemical vapor deposition technique to synthesize core—shell, dumbbell—shaped type of multifunctional nanoparticles.

4.2. Au NANOPARTICLES AS A KEY COMPONENT IN MULTIFUNCTIONAL NANOSTRUCTURES

Extensive research has been carried out in the field of multifunctional nanostructures consisting of gold as one of component in the structure. Gold has been popularly known for it's bulk properties, such as, high conduction of heat and electricity, malleability, ductility, corrosion/oxidation resistance and optical properties. In ancient times, Au nanoparticles in the form of colloidal solutions have been utilized in the process of staining the glasses with the intense colors of red and mauve. Au nanoparticles were introduced in the modern science by Michael Faraday in 1980.[132] He synthesized pure, colloidal gold called as activated gold, and the suspension of colloidal gold consists of nanometer sized gold synthesized in aqueous solution.[133] The optical properties of the colloidal gold are strongly dependent on the size of Au nanoparticles, which can be attributed to the intense red color for the particles less than 100nm in size and bluish/purple color for particles larger than 100nm.[133,134]

Au possesses remarkable variations when subjected to interaction with light. When the light is induced upon the Au nanoparticles, strong absorption/scattering takes place at the specific resonanting frequencies. These characteristic wavelengths are highly dependent on the size, morphology and dielectric environment of Au nanoparticles. This occurrence is termed as localized surface Plasmon resonance (LSPR).[135] The surface chemistry, and localized surface plasmon resonance properties of Au nanoparticles make them suitable for the broad range of practical applications. The various well—established

Au—nanoparticles synthetic protocols such as Terkevich Method,[132—135] Brush Method,[136,137] Perrault Method,[138] Sonolysis,[139] provide the flexibility for the fabrication of range of controlled sizes and shapes of Au nanoparticles. The absorption of hemoglobin and water at near infrared regions are very low, and thus by fine—tuning the LSPR of the Au nanoparticles, it is viable to utilize Au nanoparticles in biomedicine.[140,141] Additionally, Au nanoparticles possess active surface chemistry, and the nanoparticles surface could be modified through functionalizations.[142,143] One of the most important properties of Au nanoparticles is the biocompatibility. The interaction of Au as a foreign substance with the biological fluids and cells has been evaluated broadly based on their potential cytotoxicity[144] Au nanoparticle circulation in the blood stream, elimination from the organism[145] through *in—vivo* and *in—vitro* studies.[146—149] Owing to these critical attributes, Au nanoparticles are considered as favorable material in broad range of biomedical applications such as diagnostics, sensing, imaging, and therapeutic techniques.[150-153]

PAPER

I. SYNTHESIS OF SUPERCONDUCTING NANOCABLES OF FeSe ENCAPSULATED IN CARBONACEOUS SHELL

ACS Nano, 2013, 7, 1145.

Sukhada Mishra,[a] Kai Song,[b,c] Jakub A. Koza,[b] Manashi Nath[a,]*

[a]*Department of Chemistry and* [b]*Materials Research Center, Missouri University of Science and Technology, Rolla, Missouri 65409, United States.*

[c]*Present address: FEI Company, 5350 NE Dawson Creek Drive, Hillsboro, Oregon 97124, United States.*

KEYWORDS: FeSe Nanowires, Superconducting Nanowires, Pnictide Superconductors, Core—Shell Nanowires.

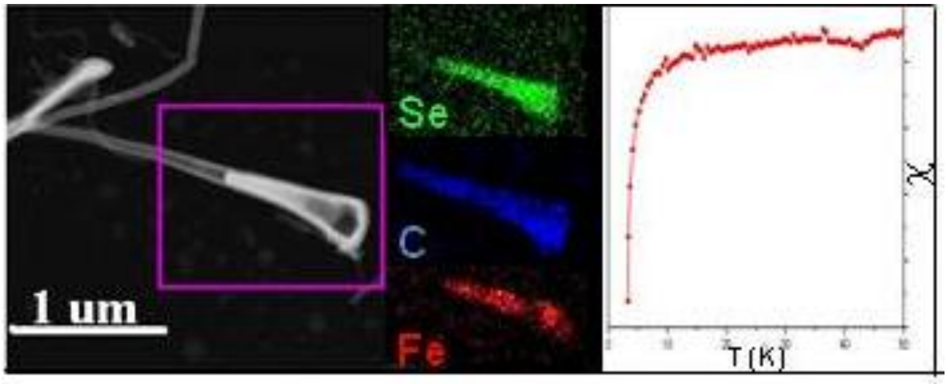

1. INTRODUCTION

The recent discovery of superconductivity in iron selenide has attracted considerable attention due to the simplicity of composition, unconventional nature of superconductivity and ease of synthesis. We have synthesized superconducting FeSe nanowires with a simple catalyst aided vapor transport reaction at 800°C in an inert atmosphere. The precursors were chosen to be elemental Se and iron acetylacetonate [FeIII($C_5H_8O_2$)$_3$]. These vaporized very easily thereby facilitating transport and also contributed to the formation of a carbonaceous shell encapsulating the FeSe nanowires. The superconductivity of these nanocables was confirmed through magnetic measurements and a Tc of ≈ 8K was obtained for an ensemble of nanocables. The length of FeSe filling inside the carbon nanofibers could be varied by controlling the reaction conditions while the diameter of nanowires was dependent on the thickness of Au—Pd coating used as a catalyst. Extensive analysis through high—resolution microscopy revealed that there was considerable lattice contraction of FeSe in the nanocable up to about 3.6% along the c—direction leading to a reduced spacing between the (001) lattice planes. Interestingly, this compression was more pronounced near the catalyst—FeSe interface and was reduced further along the length of the nanocable. The presence of carbon nanofibers as a shell around the FeSe protected the FeSe nanowires from both atmospheric O2 and moisture attack as was evident from the very long ambient condition shelf life of these nanocables, and also makes them more stable under e—beam irradiation.

The discovery of superconductivity in LaFePO in 2006 by Hosono and co-workers[1] marked the onset of a new family of iron-based superconductors. It also began an era of unconventional superconductors, which has been termed "*the iron age of superconductivity*". These new superconductors belong to the iron pnictide families, generally referred to as [1111] (*Ln*Fe*Pn*O, Ln = lanthanides, *Pn* = P, As);[2-4] [122] (A′A′′Fe2As2 A′ = K; A′′ = Ba, Sr, Eu);[5,6] [111] (AFeAs, A = Li, Na);[7,8] and the chalcogenide FeSe (011).[9] Current progress in this field has been compiled in several extensive reviews.[10-14] The presence of superconductivity in Fe-based compound itself is fascinating since Fe is more popularly known for having magnetic ordering, which does not preferably coexist with superconductivity. The common motif present in Fe-based superconductors is a Fe_2Pn_2 layer, (*Pn* = As, P), where Fe is tetrahedrally coordinated to *Pn* in the anionic layer and the cationic layers play a significant role of charge reservoirs. One of the simplest compounds containing similar Fe_2Pn_2 layers as found in these superconductors is a PbO-type tetragonal FeSe. In fact, in 2008, FeSe, a simple binary compound, demonstrated superconductivity at 8K, without any chemical doping.[9] FeSe has two major phases, a Se deficient tetragonal phase where superconductivity was initially observed,[9] and an Fe deficient phase which is a stoichiometric variant of the NiAs structure type.[15] The structure of superconducting FeSe is built by edge sharing of $FeSe_4$ tetrahedra where both Fe and Se are 4 coordinated.[16] Analogous to other iron based superconductors, FeSe also exhibits an enhancement in T_c through chemical doping with Te in anionic site (T_c = 21K).[17] More interestingly, the T_c in this tetragonal FeSe is pressure sensitive and can be increased significantly (36.5K) by applying external pressure.[18,19] Superconductivity in low-dimensional materials is of huge interest to researchers working in this field. It has been reported that superconductivity can be suppressed in ultrathin nanowires of simple elemental and alloy superconductors due to thermal and quantum phase slips.[20,21] The critical current on the other hand increases significantly with decreasing diameter of superconducting nanowires.[22,23] Theoretical studies on finite size effects in pnictide superconductors have led to the belief that both critical current and T_c can be affected in low-dimensional structures.[24] This finding is especially important for the Fe-based superconductors that inherently exhibit both high critical fields and critical current density.[10,11,14] Superconducting nanowires are also important technologically as ideally they can provide a dissipation-less flow of current in complex nanodevices. They can also facilitate high-efficiency power transmission, and offer potential applications in photodetectors,[25] superconducting gravimeters,[26] single-photon detectors,[27,28] and quantum electronics.[29] Iron-based superconductors, by virtue of their unconventional nature, are expected to demonstrate a change in not only their magnetic but also their electronic properties on nanostructuring, thereby affecting their superconducting properties.[30] To date, several superconducting nanowires, including those of simple metals,[31] cuprates [YBCO][32] and, recently, MgB_2[33,34] have been synthesized through various techniques, including vapor transport, sol-gel synthesis, electrodeposition, and lithographic pattern transfer.[20-22,32-34] However, there are very few reports on the synthesis of FeSe nanostructures till date.[35,36] Traditional techniques for synthesizing FeSe such as pulsed laser deposition,[37] the selenization of Fe films,[38] and solid state reactions[39] require drastic conditions, thereby leading to bulk morphology. FeSe nanorods were recently synthesized using chemical vapor deposition methods,[40] with H_2Se as the selenium source. In this paper we present a simple synthesis method for growing FeSe nanowires through one-step catalyst aided vapor transport reaction.

2. RESULTS & DISCUSSIONS

2.1. SYNTHESIS OF FeSe@C NANOCABLES

FeSe nanowires were synthesized by chemical vapor deposition, under N_2 flow at 800 ºC in a horizontal tube furnace equipped with a mass flow controller. In this approach for the synthesis of FeSe nanowires, the key feature was the choice of the precursors; iron acetylacetonate [$Fe(acac)_3$] and Se both subliming very easily at 180°C and 400°C respectively. These sublimable precursors were expected to assist in the formation of nanowires. A catalyst coated Si wafer, maintained at 800°C, was used as a substrate to grow the nanostructures, while $Fe(acac)_3$ and Se were kept at the desired temperatures to maintain a steady flow of the precursors. Further details of the experimental set-up are provided in the method section. After the completion of the reaction the Si substrate was covered with a blackish product. This was further characterized thoroughly through powder X-ray diffraction (pxrd), scanning and tunneling electron microscopy (SEM, TEM respectively), scanning tunneling electron microscopy (STEM), high angle annular dark field imaging (HAADF), magnetic characterization, X-ray photoelectron spectroscopy (XPS), electron dispersive spectroscopy (EDS) and Raman analysis, to get an insight into the product morphology, phase and elemental composition.

2.2. STRUCTURAL AND MORPHOLOGY CHARACTERIZATION

Figure 2.1a shows the pxrd pattern of the product, confirming the presence of tetragonal FeSe (JCPDS card number- 04-001-9129) along with the peaks for Au used as catalyst. Interestingly, the cubic phase of $Pd_{17}Se_{15}$ (JCPDS card number- 00-011-0508) was also observed as shown in the Figure 1a. Peaks of tetragonal FeSe could be indexed according to the standard pattern (JCPDS card number- 04-001-9129). It should be noted here that few FeSe peaks were indiscernible in the experimental pxrd pattern, probably due to orientation effect and anisotropy in the formed nanostructures. The pxrd pattern demonstrated a broad feature at the 2θ range of 52°-57° which can be attributed to the presence of several closely spaced peaks for $Pd_{17}Se_{15}$ that also overlaps with the peaks for tetragonal FeSe, effectively giving rise to a broad peak. It was observed that the pxrd. This could be attributed to the fact that, the pxrd pattern was collected from powder spread over Si substrate where the high crystallinity of the Si background created obstructive scattering noise from the substrate. Also the actual amount of FeSe and $Pd_{17}Se_{15}$ in the product was only a fraction of the total mass (*vide infra*) thereby reducing the signal intensity even more. The thickness of the FeSe nanostructure as estimated from the Debye-Scherrer equation[41] was ~23nm.

SEM, as shown in Figure 2.1b exhibited a high yield of nanowires, with lengths exceeding several micrometers and diameters in the range of 30 – 70 nm. Careful observation of the STEM images, however, revealed that the nanostructures possess a peculiar, core-shell type of morphology, as shown in Figure 2.2a. These nanostructures consisted of hollow tubules filled with solid material where the tip of the filling is typically darker in contrast, giving them the appearance of a '*nanocable*'. The diameter of the filling was 20-50 nm and the length of the individual tubules varied from 5-10 μm. Energy Dispersive Spectrometry (EDS) analysis demonstrated the presence of elemental Fe and Se in a 1:1 ratio in these 1-dimensional nanostructures, confirming the formation of FeSe (Supplementary Figure 10.1). A detailed elemental analysis of the nanocables was performed through EDS line scans collected from different locations along the nanocable length to determine the composition of the nanocable tip, filling, and tube wall. Figure 2.2b illustrates the line scan performed at the tip of the nanocable, revealing the presence of both Au and Pd catalyst as major components along with trace amounts of Fe and Se. Figure 2.2c illustrates the line scan collected from the body of the filling. In this region, both Fe and Se appeared to be the major components along with C and negligible amounts of Au and Pd. Interestingly, the C signal (green line) peaked near the tube wall, indicating there was less C in the filling itself. Figure 2.2d illustrates the line scan performed across the tubule where there was no filling, clearly showing that the C signal was most intensified with a negligible amount of Se, Fe, Au, and Pd. Thus, it was concluded that the hollow tubules were comprised of C, while the filling was purely FeSe. Further quantitative and qualitative analysis was performed using X-ray photoelectron spectroscopy (XPS) technique to confirm the chemical composition (Supplementary Figure 10.2a). The XPS spectra collected on the nanocables indicated the presence of elemental Se and C, along with a trace amount of Fe. After sputtering for 20 minutes which removed approximately 20 nm surface layers of nanocables, the Fe signal increased significantly and the C signal decreased. This type of superconducting nanowires, encapsulated by carbon nanotubes (CNT), has been previously reported for Sn nanowires.[42] Raman spectroscopy was conducted on an ensemble of these nanocables to get a better insight of the carbonaceous shell in these nanocables. Raman analysis

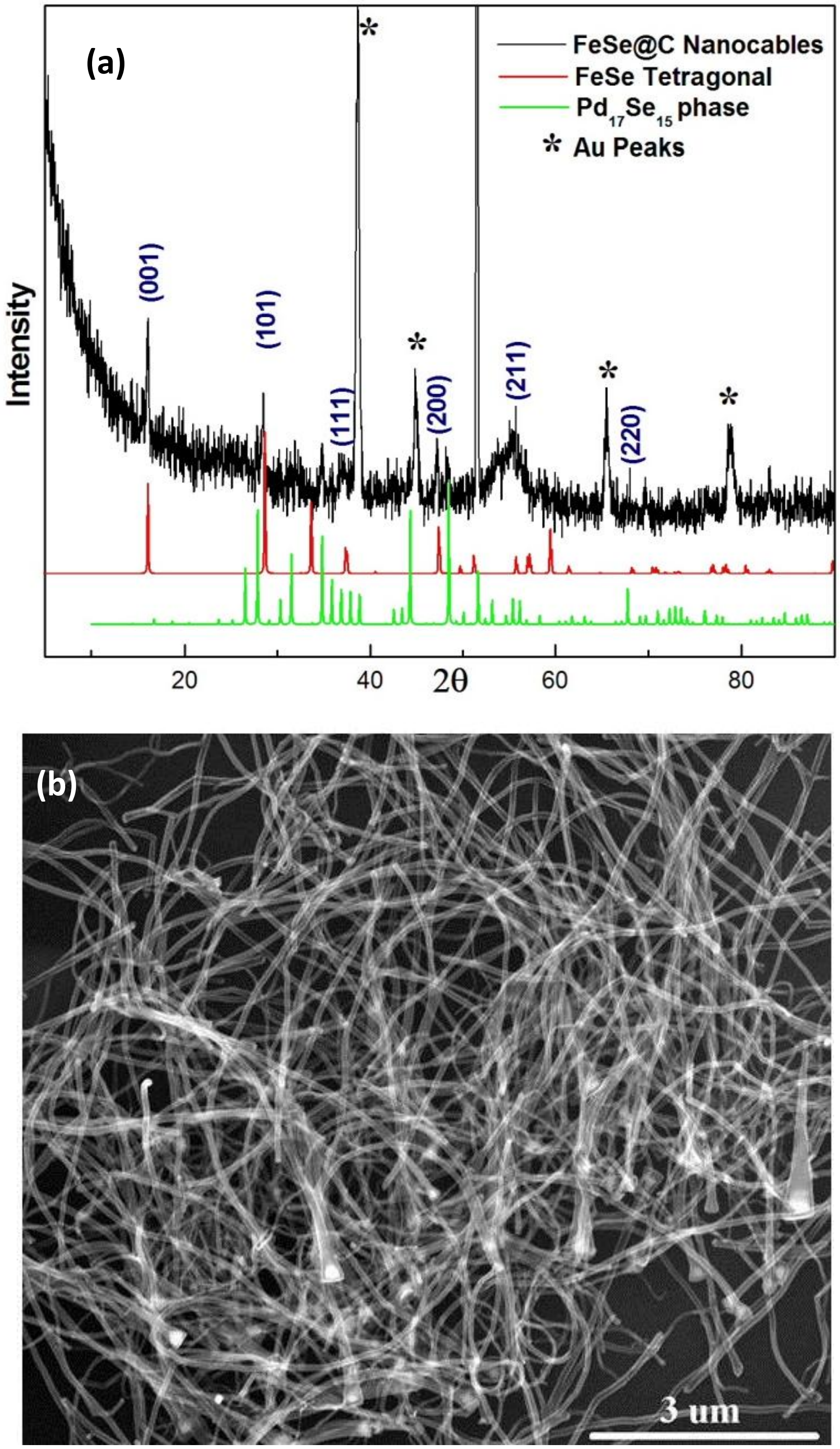

Figure 2.1. (a): PXRD pattern of the nanowires showing a mixture of tetragonal FeSe and cubic $Pd_{17}Se_{15}$ along with Au peaks. (b) SEM image showing huge yield of nanowires over the Si substrate.

demonstrated both, a D band and a G band at 1319.30 cm^{-1} and 1585.85 cm^{-1} respectively (Supplementary Figure 10.2b). The area integral intensity ratio of the D and G peaks (ID/IG) in the Raman spectra was calculated to be 3.327, indicating the presence of amorphous carbon in the form of nanofibers.[43] The length of the FeSe filling inside the nanocables could be increased by varying the reaction conditions, including an increase in the concentration of the reactants (Se and $Fe(acac)_3$), whereby, we could successfully extend FeSe filling further away from the tip (Supplementary Figure S3). The diameter of the FeSe filling could be somewhat controlled by the diameter of the Au-Pd catalyst particle, where the optimal catalyst thickness was observed to be 50 – 100 nm. These nanocables were also analyzed through a high resolution transmission electron microscopy (HRTEM), which demonstrated crystalline nature of the FeSe filling and offered some valuable insights for understanding the growth mechanism of these FeSe@C nanocables (*vide infra*).

Superconductivity in these nanocables was characterized by DC magnetic susceptibility, measured on an ensemble of nanocables, spread on the Si substrate. Magnetization was measured as a function of temperature, under zero field cooled conditions using, a vibrating sample magnetometer. Figure 2.3 illustrates a plot of magnetic susceptibility (χ) as a function of temperature, measured with an applied field of 100 Oe. Superconducting transition was clearly observed at ≈ 8K which was in good agreement with the T_c of bulk FeSe.[9] Since the exact mass of the nanocables dispersed over Si could not be precisely determined, the magnetization data could not be normalized with respect to mass. Hence, the magnetization of a blank Si substrate was also measured under similar conditions and used as a reference. As expected the Si

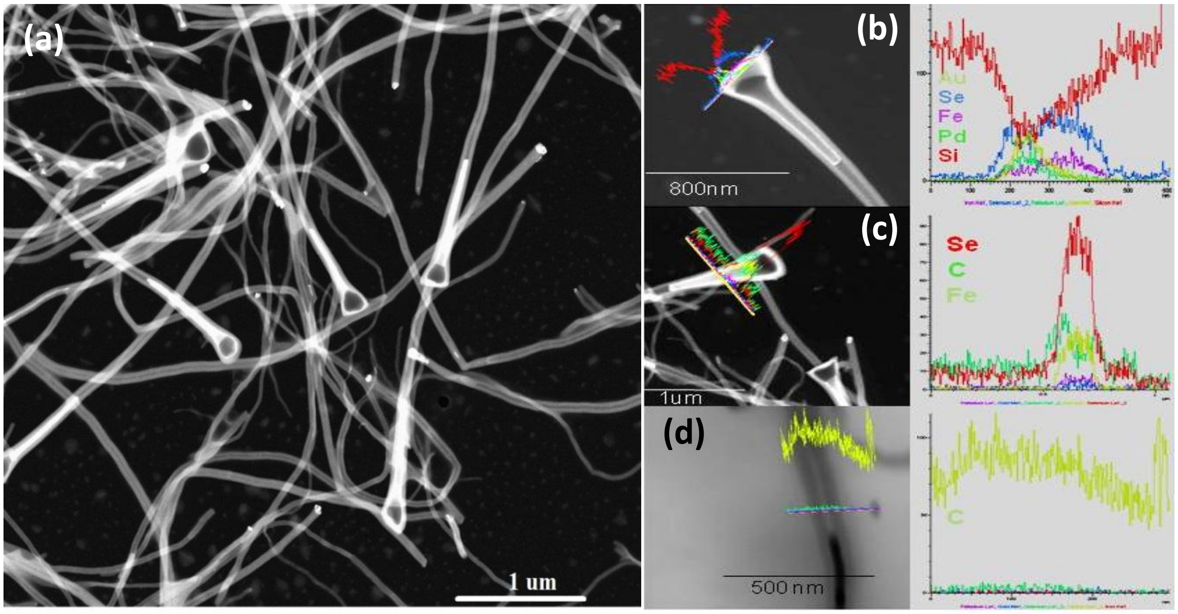

Figure 2.2. (a): Low magnification STEM image of the formed nanocables, showing core-shell type of morphology along with nanocable tip (b)-(d) Elemental analysis through line scan at the (b) tip of the nanocable showing the presence of Au, Pd, C, Se, Fe (right panel) (c) in the filling part showing Fe, Se and C predominantly and minimal Au, Pd. (d) in the tube confirming the presence of carbon nanofibers.

substrate by itself did not demonstrate any appreciable transition (Supplementary Figure 10.4). However, the magnetization data from the ensemble was heavily masked by the huge diamagnetic background from both the Si substrate and the carbonaceous shell. Interestingly, the carbonaceous shell did not affect the superconducting T_c of FeSe in these nanocables. This observation is similar to that made by Jankovic et al. for their CNT coated Sn nanowires.[42]

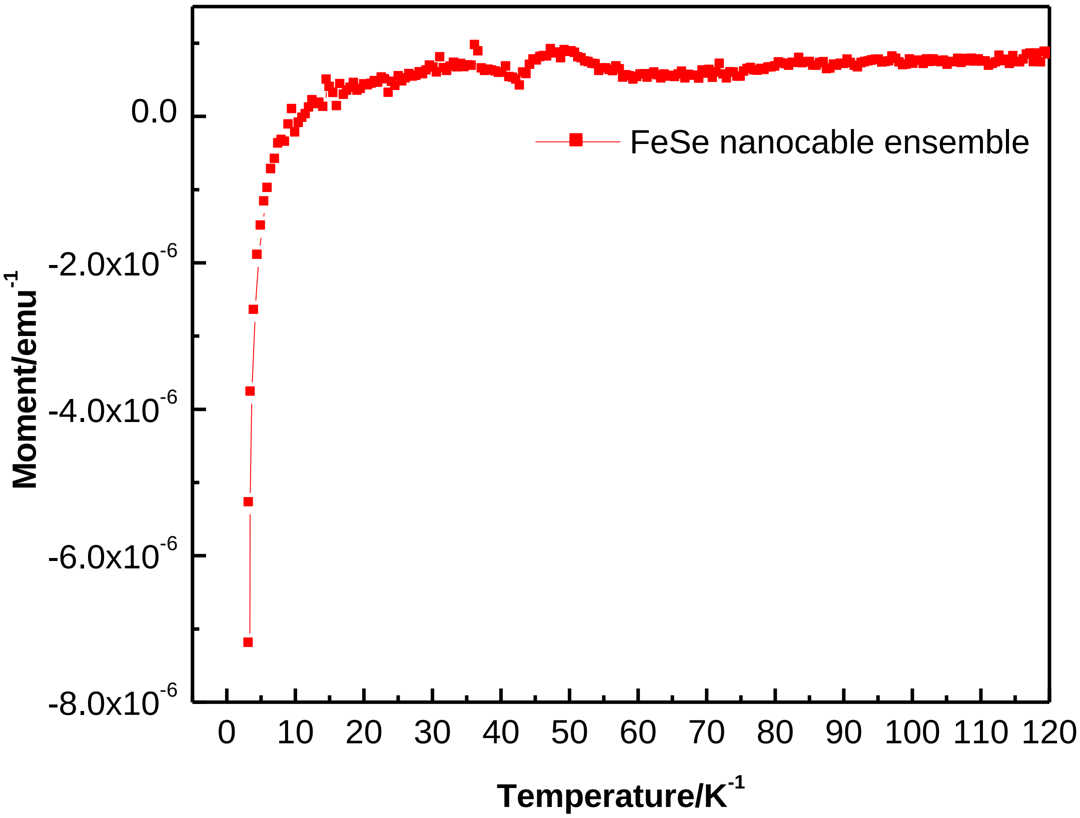

Figure 2.3. Plot of magnetic susceptibility *vs* temperature of the FeSe@C nanocables showing the onset of superconducticvity at ≈ 8K. Inset shows the closer view of the transition.

3. HIGH RESOLUTION TEM CHARACTERIZATION OF FeSe@C NANOCABLES

HRTEM was performed at various regions of the FeSe@C nanocables, as shown in Figure 3.1a – f. HRTEM revealed lattice fringes of both the FeSe filling and Au-Pd-rich catalyst, which demonstrated high degree of crystallinity of these phases. The carbon tubule walls, however, did not demonstrate a high degree of crystallinity. Figure 3.1a illustrates the bright field TEM image of a filled nanocable which includes regions of different contrast. An EDS line scan along the same nanocable (Figure 3.1b) indicates that, beginning at the tip, the nanocable has a sequence of Au-rich, Pd-Se-rich, Fe-Se-rich, Pd-Se-rich, and Fe-Se-rich segments as shown by arrows in the Figure 3.1a. EDS point analysis collected from the above marked regions also corroborated the proposed element distribution (Supplementary Figure 10.5). The electron diffraction pattern (inset in Figure 3.1a) obtained from the Au-rich tip confirmed the presence of single crystalline Au. It was observed that while Au was immobilized at the tip of the nanocable, the Pd part of the bimetallic catalyst actually attached to the growing FeSe (as shown in Figure 3.1a) and was frequently dislodged from the tip, whereby, the Pd-rich segment was located within the FeSe filling (4th arrow from the left in Figure 3.1a). Figure 3.1c is a magnified HRTEM image illustrating the interface between the Pd-Se region (on the left) and the Fe-Se region (on the right). The lattice spacing in the Fe-Se region was measured to be 5.32 Å, which is in close agreement with the (001) plane of the tetragonal FeSe phase. The Pd-Se rich region was characterized by electron diffraction (ED) generated by Fast Fourier Transform (FFT) from the lattice fringes (inset of Figure 3.1c), which indicated the presence of cubic $Pd_{17}Se_{15}$ single crystal. While majority of the FeSe nanocables showed lattice fringes corresponding to (001) planes, some nanocables as

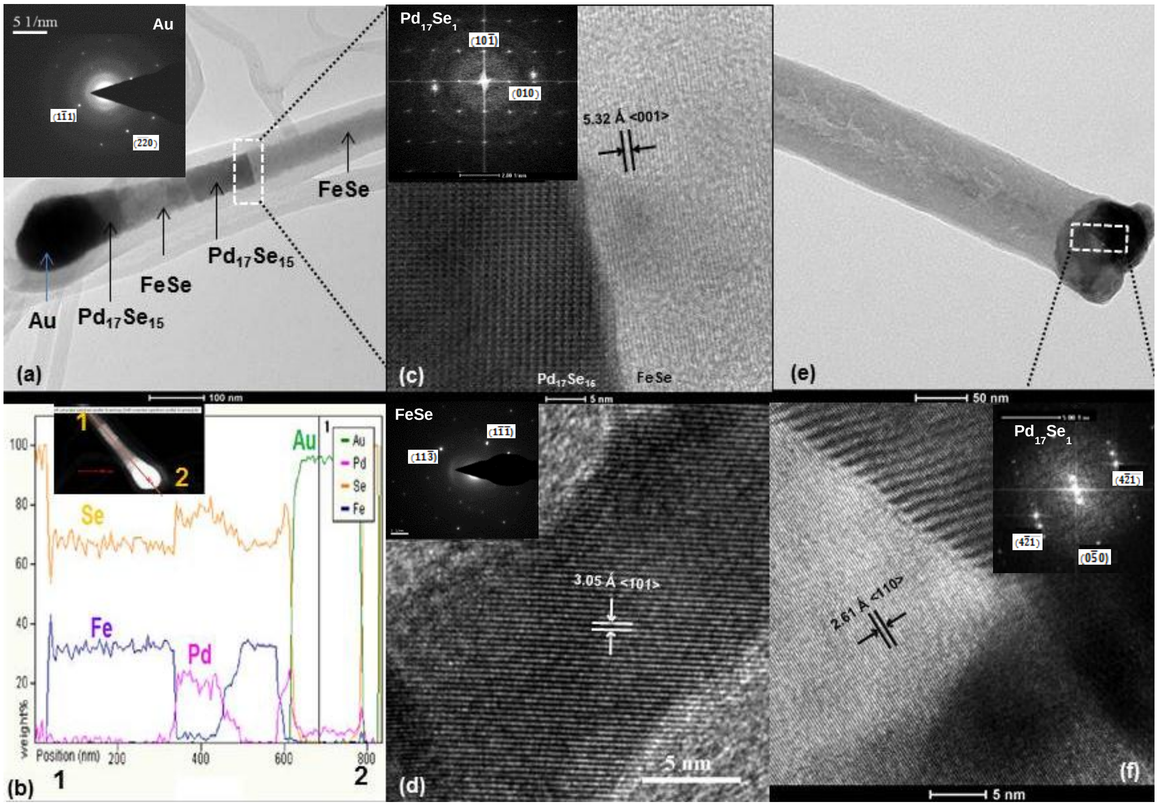

Figure 3.1. (a): TEM image of the FeSe@C nanocable showing the segregation of Au, Pd$_{17}$Se$_{15}$ and FeSe along the nanocable length. Inset shows the SAED pattern obtained from the Au region. (b) EDS Line scan performed across the length of the nanocable (from position 1-2) tracing the presence of Au, Pd, Fe and Se at different regions. (c) HRTEM image showing the interface between Pd$_{17}$Se$_{15}$ and FeSe. Inset shows the FFT pattern generated from the Pd$_{17}$Se$_{15}$ region. (d) The HRTEM image of the FeSe displaced away from the catalyst tip. Inset shows the SAED with the spots indexed to tetragonal FeSe. (e) TEM image of the catalyst tip at the end of the FeSe@C nanocables showing coexistence of Pd$_{17}$Se$_{15}$ and FeSe. (f) HRTEM image of the catalyst tip, showing the interface between FeSe (left side) and Pd$_{17}$Se$_{15}$ (right side). Inset shows the FFT pattern of the PdSe phase.

shown in Figure 3.1d exhibited lattice fringes at 3.05 Å corresponding to the (101) plane. HRTEM images shown in Figure 3.1d was collected from the FeSe filling which was far away from the catalyst tip. The inset in Figure 3.1d illustrates the experimental electron diffraction pattern from this FeSe filling phase which contained diffraction spots corresponding to the ($11\bar{3}$ and $1\bar{1}\bar{1}$) planes, respectively. Frequently the other end of these nanocables also contained a catalyst tip, as shown in Figure 3.1e which shows regions of different contrast. A magnified, high resolution image of this catalyst tip collected from the region marked by the white box is given in Figure 3.1f. The lattice spacing from the FeSe region was measured to be 2.61 Å, matching that of the (110) planes of the tetragonal FeSe phase. The inset in Figure 3.1f shows the FFT image of the Pd/Se region which contained spots corresponding to 2.48 Å, 2.29 Å and 2.09 Å, matching with the $(4\bar{1}\bar{1})$, $(4\bar{2}\bar{1})$ and $(0\bar{5}0)$ planes of the cubic $Pd_{17}Se_{15}$ phase respectively. Single crystal Si was used as a calibration standard for accurately estimating the lattice spacing from HRTEM images. All calculations for lattice spacing were done by counting at least 30 lattice planes. From these detailed microscopic studies involving HRTEM, EDS line scans and elemental mapping, it was evident, that the nanocables are not pure FeSe but rather consisted of segments of Au, $Pd_{17}Se_{15}$ and FeSe, thereby forming a composite nanocable. But, it should be noted here that, the FeSe segment in the nanocable was chemically pure since there was no evidence of chemical doping with either Pd or Au in the FeSe regions.

4. EVIDENCE FOR LATTICE COMPRESSION OF FeSe AND ITS EFFECT ON T_c

It should be noted that the (001) lattice spacing for the tetragonal FeSe is reported to be 5.52 Å.[15] For the FeSe nanocables, the (001) lattice spacing consistently demonstrated a contraction of ~3.62%. Lattice compression for the FeSe was also observed through a reduction of lattice spacing for other planes such as the (101) plane [3.05 Å (experimental) *vs* 3.15 Å (reported)], which showed a contraction of ~3.1% as seen in Figure 3.1d. Analogous to both (001) and (101) planes of FeSe, the (110) plane of FeSe also indicated a contraction in the lattice spacing. The value obtained from the standard diffraction data was 2.69 Å. This value corresponds with a ~2.97% of lattice contraction along [110]. From the extensive HRTEM and SAED analysis it was evident that the FeSe in these nanocables showed appreciable lattice compression which was maximum along the [001] direction but also noticeable along the [101] and [110] directions. The lattice compression along the *c*-axis (*i.e.* [001] direction) is very critical in the FeSe superconductors. Previous work by Cava and co-workers have established that on application of external pressure, the FeSe lattice shrinks along the *c*-direction thereby leading to denser packing of the Fe_2Se_2 layers. This compression along the *c*-direction is accompanied by an enhancement in T_c.[18,19] The compression along the *c*-direction increases with the applied pressure, before the FeSe lattice undergoes a total phase transformation to the hexagonal phase at 38 GPa of pressure.[18,19] Hence it can be expected that in these FeSe nanocables, compression of the lattice along the [001] direction is reflective of some internal pressure effect. The pressure on the FeSe nanocables might be attributed mainly to the presence of FeSe-$Pd_{17}Se_{15}$ interface and also to the effect of restricted growth within the carbonaceous shell. Since T_c in FeSe superconductors is very sensitive to pressure, it might be expected that the lattice compression will show some effect in the T_c of these nanocables. However, the T_c as obtained from magnetization studies of the FeSe nanocable ensemble was ~8K as shown in Figure 2.3.

Hence, to get a better insight into this compression along the [001] direction in the FeSe nanocables extensive HRTEM studies were performed on FeSe region in different parts of the filling (i) (Figure 4.1a – d): *viz* at the interface with the Pd-Se phase; (Figure 4.1b); (ii) at the middle portion of the FeSe filling (Figure 4.1c); and (iii) at the open end of the filling (Figure 4.1d). Figure 4.1a shows the low magnified image of the nanocables showing different regions, Au, FeSe, and $Pd_{17}Se_{15}$. Figure 4.1b shows the fringes obtained from the FeSe region close to FeSe/ $Pd_{17}Se_{15}$ interface. Inset of 5b indicates FFT obtained from the same region which could be indexed to (001) planes of tetragonal FeSe. The d-spacing corresponding to (001) plane could be calculated (from both the lattice fringes and FFT) as 5.29 Å which corresponds to approximately 3.8% contraction. Figure 4.1c shows the fringes obtained from the middle portion of the FeSe filling. It shows the lattice spacing of 5.44 Å which corresponds to 1.44% lattice contraction. Figure 4.1d demonstrates HRTEM obtained from the FeSe region corresponding to the open end of the filling. It showed the lattice spacing of 5.51 Å for the (001) planes which corresponds to 0.1% contraction. These observations indicate that the lattice compression is maximum at the FeSe-$Pd_{17}Se_{15}$ interface, and reduces as the FeSe grows away from the interface and is almost negligible at the open end of the FeSe filling. Hence, the amount of FeSe facing this interfacial pressure is only a fraction of the entire nanocable. This might be the reason that the effect on T_c is very minimal. The authors are currently trying

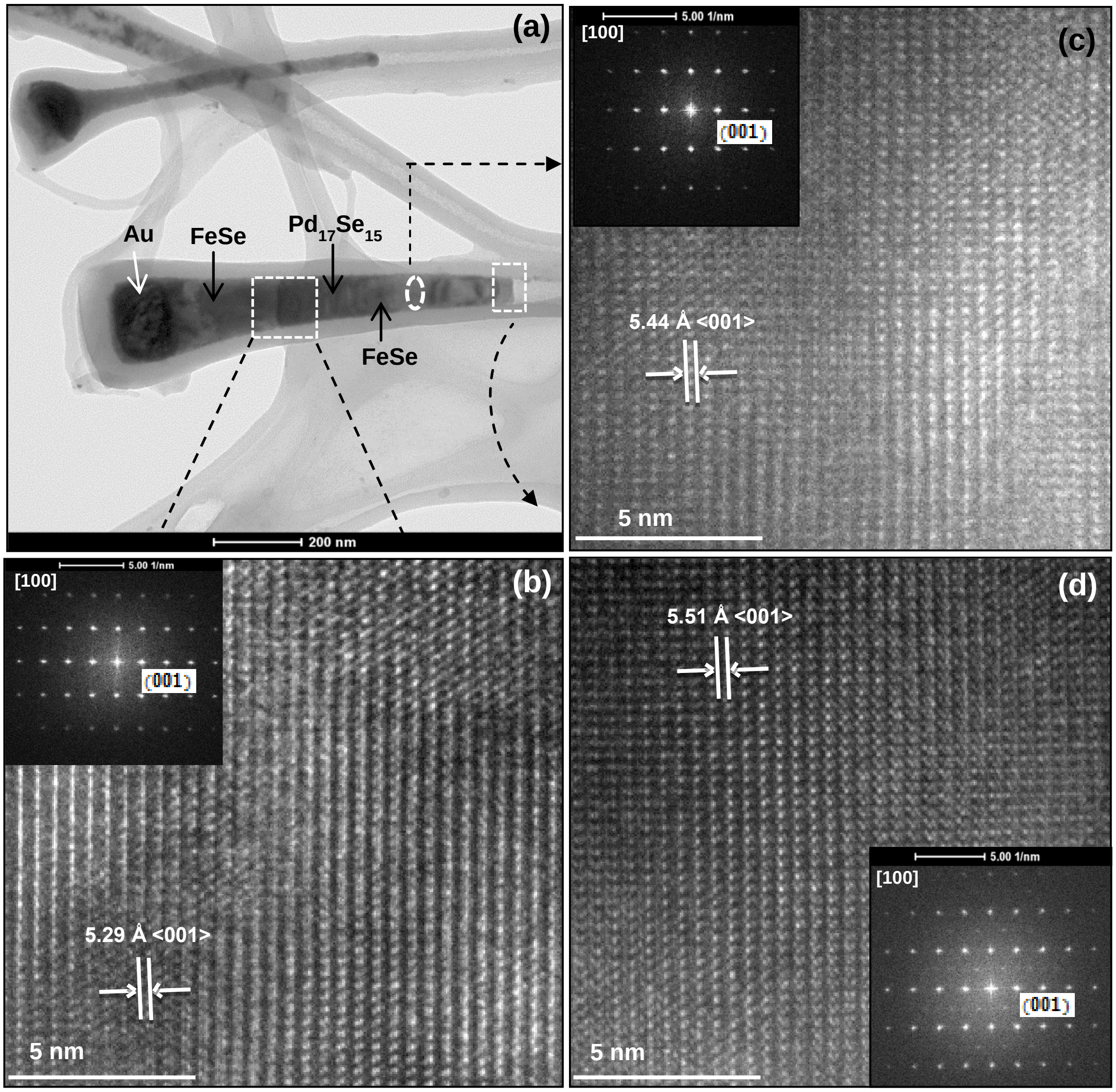

Figure 4.1. HRTEM images of FeSe region collected from different sections in the nanocable. (a) Low-magnification image of the nanocable showing different regions (Au, FeSe, $Pd_{17}Se_{15}$) as marked by arrows. (b) FeSe region near the interface [shown by white box in (a)] with lattice fringes corresponding to (001) planes showing a spacing of 5.23 Å. (b) FeSe region at the middle of the nanocable showing a lattice spacing of 5.44 Å for the (001) planes. (c) FeSe region at the end of the nanocable away from the catalyst tip, showing a separation of 5.51 Å between the (001) planes. Inset in (b) – (d) shows the FFT generated ED patterns, with diffraction spots corresponding to (001) planes.

to increase the interfacial contact area between the Pd-Se and FeSe phases, thereby expecting a larger lattice compression and enhanced effect on the T_c.

5. MECHANISM OF GROWTH OF FeSe@C NANOCABLES

We varied reaction parameters to gain an insight into the formation mechanism of FeSe@C nanocable. We soon realized that the role of a bimetallic catalyst is important for formation of the FeSe nanocables. Experiments conducted in the absence of Au-Pd catalysts did not produce any FeSe deposition on the Si substrate. An investigation of the reaction products at lower temperatures (600 – 800 °C) provided an insight into the mechanism behind the growth of FeSe nanowires. We performed detailed characterization of the intermediate nanostructures through extensive electron microscopy (SEM, TEM and STEM) and EDS analysis. Figure 5.1 shows the various stages involved in the formation of FeSe@C nanocables. During the initial stages of growth, the catalyst particles demonstrated a segregation of Au and Pd, leading to the formation of hetero-zones as shown in the TEM image in Figure 5.1a. It should be noted here that, the formation of a carbonaceous shell was very apparent right from the primary stages of nanostructure formation, and the origin of it has been described in detail below. The phase segregation of Au and Pd was also confirmed through elemental line scan performed across the bimetallic catalyst (shown in the bottom part of the Figure 5.1a), which showed two distinct phases: Au in the higher contrast region and Pd-Se in the lower contrast region. EDS spectra revealed trace amounts of Fe along with Au, Pd and Se in these biphasic nanoparticles (Supplementary Figure 10.6), demonstrating that at low temperatures (600 °C), the incorporation of Fe into these nanostructures have just only begun. Fe was present mostly at the Pd-rich edges of the biphasic nanoparticles, indicating that the decomposition and adsorption of Fe-precursors were catalyzed by the Pd part of the bimetallic catalyst. In the second stage of growth, Se and Fe-rich vapors started diffusing in the bimetallic Au-Pd catalyst. Figure 5.1b shows the elemental mapping from an arrested intermediate stage of growth, where the nanocable has just started growing out from the catalyst end. It demonstrated similar segregation of Au and Pd region in the catalyst tip, while the preferential attachment of the growing Fe-Se region to the Pd-end of the catalyst was more visible at this stage. Small migration of $Pd_{17}Se_{15}$ near the growing Pd-FeSe interface was also very apparent in the elemental mapping which showed that, while Pd is most concentrated near the catalyst tip (upper left hand region of the Pd map in Figure 5.1b), there is a minor spreading of Pd into the Fe-rich region. Se mapping indicates the spread of Se over the entire Pd- and Fe-rich regions. As the mapping was performed in the STEM mode of TEM, the brighter contrast of carbon shell was not visible in the STEM image. The continuous supply of iron from the precursor into the growing nanofibers through surface diffusion formed the thermodynamically stable FeSe filling. As the reaction continues, the formed FeSe further gets filled up inside the carbonaceous shell and led to the formation of nanocables. Figure 5.1c demonstrates the elemental mapping of the fully grown nanocable. The segregation of the bimetallic catalyst is carried over to the nanocables also, where the Au catalyst remains at the tip away from the FeSe, while the Pd gets diffused in the growing nanocables near the catalyst-FeSe interface.

The formation of C nanofibers was highly unanticipated in this reaction scheme. The choice of the iron precursor, however actually facilitated the formation of C nanofibers. During the reaction, $Fe(acac)_3$ was not only a source of iron but also a huge reservoir of carbon. These factors gave rise to an ideal condition for the growth of carbon nanofibers encapsulating the formed FeSe. Previous studies indicate that, the multiwall carbon nanotubes forms readily on the Au-Pd catalyst.[44] As the reaction progresses, the carbon species generated through a decomposition of Fe(acac)$_3$ both dissolves and diffuses into the liquid catalyst. At supersaturation of the catalyst the carbon gets precipitated out as nanofibers. The presence of carbon precursors at the temperature of 800°C provided an ideal condition for the growth of carbon nanofibers, and the Fe and Pd acted as liquid phse catalyst.

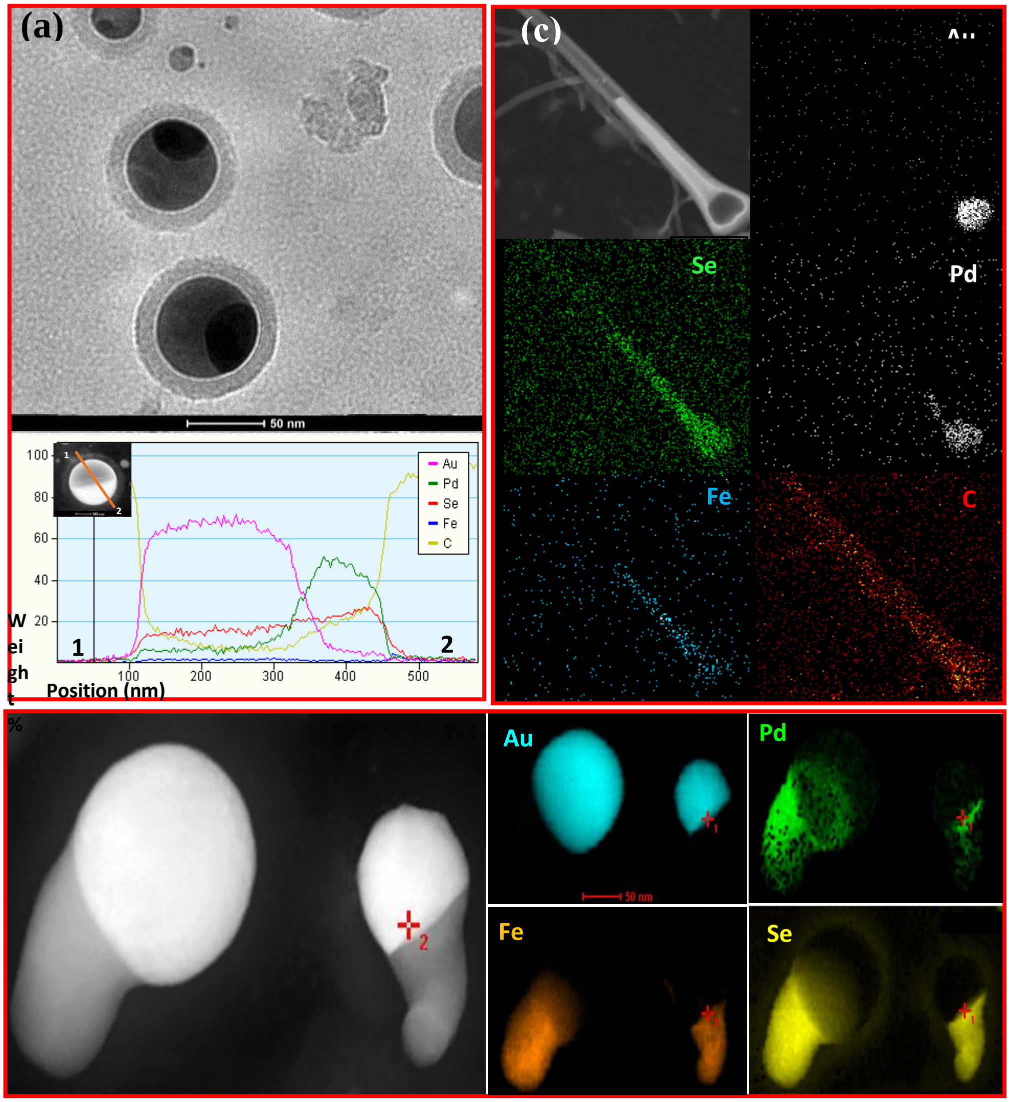

Figure 5.1. (a): TEM image of the carbon encapsulated catalyst formed at 600°C, which shows segregation of Au-Pd. Panel at the bottom shows the EDS line scan performed across the catalyst particle (shown in inset) confirming presence of Au and Pd-Se rich zones, respectively. (b) STEM image of a nanocable in the second stage of growth along with corresponding elemental mappings for Au, Pd, Fe and Se. The carbonaceous shell was not very visible since it was acquired in HAADF mode of STEM. (c) Elemental mapping of a fully grown FeSe@C nanocable showing distribution of Au, Pd, Fe, Se and C along different sections of the nanocable.

6. BINARY PHASE DIAGRAMS OF Au-Pd, Pd-Fe, Pd-Se AND Fe-Se SYSTEMS

To understand the different activity of the Au and Pd zone of the bimetallic catalyst towards formation of the FeSe phase, we looked at the binary phase diagrams of Au-Pd, Pd-Fe, Au-Se and Pd-Se systems.[45-48] From the Au-Pd binary phase diagram it was evident that they mostly exist as solid solution and do not form any stable alloy till about 1100 ºC above which they form the molten phases.[45] Hence, the segregation of the bimetallic catalyst into the Au-rich and Pd-rich zones as the reaction temperature was raised to 800 ºC could be explained. The Au-Fe phase diagram shows minimal miscibility of these two elements at 800 ºC.[46] The Fe-Pd phase diagram on the other hand revealed that, in the Pd excess region, stable alloys like FePd and $FePd_3$ can be formed above 250 ºC.[47] This indicates that Fe has a better miscibility with Pd than with Au and hence, in the present case as the $Fe(acac)_3$ precursor is transported over the catalyst particle and decomposes, the Pd zone of the catalyst particle will preferentially act as the nucleation point for *VLS* growth. As Se vapors are transported in the reaction zone, it gets dissolved into the Pd-Fe rich zone of the catalyst thereby forming the selenides. The Pd-Se binary phase diagram reveals that in the excess Se zone, $Pd_{17}Se_{15}$ is one of the stable intermediates before it goes to $PdSe_2$.[48] The miscibility of Fe with Pd, and the preferential stability of the Pd- and Fe-selenides leads to Pd-end of the catalyst being the active growth zone, while Au is immobilized at the non-participating end. Hence, as the nanofiber is being filled up with FeSe, the catalyst-filling (FeSe) interface at the Pd-end will play a very definitive role in defining the crystal structure of the FeSe filling. The authors are trying to investigate this theme further by attempting synthesis of FeSe nanostructures catalyzed by pure Pd nanoparticles which may show interesting variation in the properties. In order to proceed in this approach, a thin layer of the Pd nanoparticles coated on Si wafer have been utilized as caralyst to produce FeSe coated over Pd particles. It is expected to observe an enhancement in superconducting transition temperature of FeSe through increased interfacial pressure across catalyst-Fese interphase.

7. CONCLUSION

In conclusion, we have successfully developed a protocol for the synthesis of the superconducting FeSe ($T_c \approx$ 8K) nanocables surrounded by a carbonaceous shell. The simplicity of the process makes it viable for a large scale production of the superconducting nanocables. The nanocables reported in this paper indicate a ~3.65% compression of the FeSe lattice along the *c*-direction where the compression is more near the catalyst-FeSe interface and reduces further along the length. The presence of an interface between the Pd-rich phase and FeSe, in combination with restricted growth, may lead to a build-up of internal pressure acting on FeSe resulting in compression of the lattice. Because the T_c in the FeSe superconductors is extremely pressure sensitive, this type of nanostructure will be more useful when investigating the effect of morphology on the T_c. For example, we are currently trying to increase the catalyst-FeSe interface while preserving the nanostructured morphology, thereby expecting to see a much more contraction in the *c*-direction of FeSe and significant enhancement in T_c. The distinguishing factor is that the carbonaceous shell does not destroy the superconducting characteristics of the FeSe. It may instead protect the FeSe from undergoing either aerial oxidation or any other atmospheric damage, both of which may lead to either the destruction or inhibition of superconducting properties. These types of superconducting nanocables can be of significant technological importance since the superconductors being already encapsulated by carbon nanofibers provides an assembly that can be further utilized for the superconducting FET device manufacturing.

8. METHODS

8.1. SYNTHESIS OF FeSe@C NANOCABLES

Core-shell FeSe@C nanocables were grown on a Si substrate (Si quest international) by chemical vapor deposition. These Si substrates were cut into pieces of 1 × 1cm^2 and prewashed with isopropanol and acetone in order to remove dirt particles. These substrates were then sputtered coated with Au-Pd (3:2) for 120 seconds creating a thick layer of (approximately 100 nm) Au-Pd over the substrates.

A chemical vapor deposition with a horizontal tube furnace assembly was utilized to synthesize the FeSe@C nanocables. Silicon substrates were kept at the central region of the horizontal furnace at 800°C. With the help of a mass flow controller the reaction assembly was maintained at a continuous N_2 flow of 180 sccm. Both iron (III) acetylacetonate (99% purity, STREM chemicals) and selenium shots (1-3 mm, amorphous, 99.999%) were chosen to be the precursors for Fe and Se, respectively. Selenium shots were positioned at 400°C, the Fe(acac)$_3$ was kept at a 180°C region. Initially, The Fe(acac)$_3$ and Se were kept outside the heating zone by pushing the ceramic liner to the extreme left. Once the central zone of the furnace was reached the reaction temperature (800°C), the ceramic liner was pushed to the right such that the Se and Fe(acac)$_3$ were at 400 ºC and 180 ºC respectively. This steps were crucial for reproducibility of the reaction, as it avoids the sublimation and escape of the reactants (Se and Fe(acac)$_3$vapors) before the Au/Pd catalyst reaches the melting temperature. The reaction was conducted out for 30 minutes, and the furnace was cooled down at the rate of 8C°/min. After the reaction was completed, we observed a grayish black deposition on the silicon substrate.

8.2. CHARACTERIZATION OF THE NANOCABLES

8.2.1. Powder X-ray Diffraction. The product was characterized without any subsequent purification through powder X-ray diffraction (Philips X-Pert) using CuKα (1.5418Å). Because the product formed a very thin layer on the Si substrate, the pxrd was collected at grazing angles in thin film geometry (GI mode with Göbel mirrors).

8.2.2. Electron Microscopy Characterizations. Scanning electron microscope imaging was performed using FEI Helios NanoLab 600 FIB/FESEM) directly onto the Si substrate covered with the nanocables. TEM images were obtained on FEI Tecnai F20 operating at 200kV. Black powder on Si substrate was both scratched and dispersed in an acetone solution to prepare the TEM sample. A drop of the "as prepared" solution was placed onto a carbon coated TEM grid and dried in air prior to TEM imaging and EDS.

8.2.3. Magnetic Characterizations. A magnetic moment was collected from both a SQUID magnetometer and the VSM option of PPMS. The Si-substrate containing the FeSe@C nanocables was loaded into a gel cap and was inserted into the magnetometer with the help of standard sample loader. The diamagnetic signal from the gel cap was collected separately and subtracted as a background from the signal obtained from the sample. The ZFC data was obtained after cooling the sample down to ~2K under 0 magnetic field and then by measuring the magnetic susceptibility warming up data. The susceptibility of a blank Si substrate which was heat treated under conditions (similar to that for FeSe nanocable growth) was also collected and used as a reference.

8.2.4. X-ray Photoelectron Spectrometry. Elemental quantification was performed on a Kratos Axis 165 Photoelectron Spectrometer. The Si substrate containing an ensemble of the FeSe@C nanocables was analyzed both before and after sputtering.

Sputtering was performed for 20 minutes, which removed approximately 20 nm layer from the substrate.

8.2.5. Supporting Information. Both XPS and Raman analysis, along with EDS elemental quantification data, and the magnetization behavior of Si substrate, is available free of charge *via* the Internet at http://www.pubs.acs.org.

Corresponding Author

nathm@mst.edu

Acknowledgments. The authors would like to acknowledge the Materials Research Center, at Missouri University of Science and Technology for allowing us to use their equipment. The authors would also like to thank Dr. Switzer, Seng Huat Lee and Dr. Hor for their help with magnetic characterizations.

9. REFERENCES

(1) Kamihara, Y.; Hiramatsu, H.; Kawamura, R.; Yanagi, H.; Kamiya, T.; Hosono, H. Iron-Based Layered Superconductor: LaOFeP. *J. Am. Chem. Soc.* **2006**, *128*, 10012-10013.

(2) Kamihara, Y.; Watanabe, T.; Hirano, M.; Hosono, H. Iron-Based Layered Superconductor La[$O_{1-x}F_x$]FeAs ($x = 0.05-0.12$) With $T_c = 26$ K. *J. Am. Chem. Soc.* **2008**, *130*, 3296-3297.

(3) Johrendt, D.; Pöttgen, R. Pnictide Oxides: A New Class of High-T_c Superconductors. *Angew. Chem. Int. Ed.* **2008**, *47*, 4782-4784 and references cited therein.

(4) Chen, X. H.; Wu, T.; Wu, G.; Liu, R. H.; Chen, H.; Fang, D. F. Superconductivity at 43 K in $SmFeAsO_{1-x}F_x$. *Nature* **2008**, *453*, 761-762.

(5) Rotter, M.; Tegel, M.; Schellenberg, I.; Hermes, W.; Pöttgen, R.; Johrendt, D. Spin-Density-Wave Anomaly at 140 K in the Ternary Iron Arsenide $BaFe_2As_2$. *Phys. Rev. B* **2008**, *78*, 020503-20507.

(6) Alireza, P. L.; Ko, Y. T. C.; Gillett, J.; Petrone, C. M.; Cole, J. M.; Lonzarich, G. G.; Sebastian, S. E. Superconductivity Up to 29 K in $SrFe_2As_2$ and $BaFe_2As_2$ at High Pressures. *J. Phys. Condens. Mat.* **2009**, *21*, 012208-012212.

(7) Chu, C. W.; Chen, F.; Gooch, M.; Guloy, A. M.; Lorenz, B.; Lv, B.; Sasmal, K.; Tang, Z. J.; Tapp, J. H.; Xue, Y. Y. The Synthesis and Characterization of LiFeAs and NaFeAs. *Physica C* **2009**, *469*, 326-331.

(8) Wang, X. C.; Liu, Q. Q.; Lv, Y. X.; Gao, W. B.; Yang, L. X.; Yu, R. C.; Li, F. Y.; Jin, C. Q. The Superconductivity at 18 K in LiFeAs System. *Solid State Commun.* **2008**, *148*, 538-540.

(9) Hsu, F. C.; Luo, J. Y.; Yeh, K. Y.; Chen T. K.; Huang, T. W.; Wu, P. M.; Lee, Y. C.; Huang, Y. L.; Chu, Y. Y.; Yan, D. C. *et al.* Superconductivity in the PbO-Type Structure α-FeSe. *Proc. Natl. Acad. Sci.* **2008**, *105*, 14262-14264.

(10) Paglione, J.; Greene, R. L. High-Temperature Superconductivity in Iron-Based Materials. *Nature Phys.* **2010**, *6*, 645-658.

(11) Hiramatsu, H.; Katase, T.; Kamiya, T.; Hosono, H. Thin Film Growth and Device Fabrication of Iron-Based Superconductors. *J. Phys. Soc. Jpn.* **2012**, *81*, 011011(25 pages).

(12) Hosono, H. Layered Iron Pnictide Superconductors: Discovery and Current Status *J. Phys. Soc. Jpn.* **2008**, *77 Suppl. C*, 1-8.

(13) Lumsden, M. D.; Christianson, A. D. Magnetism in Fe-Based Superconductors. *J. Phys. Condens. Mat.* **2010**, *22*, 203203 (24 pages) and references cited therein.

(14) Stewart, G. R. Superconductivity in Iron Compounds. *Rev. Mod. Phys.* **2011**, *83*, 1589-1649 and references cited therein.

(15) McQueen, T. M.; Huang, Q.; Ksenofontov, V.; Felser, C.; Xu, Q.; Zandbergen, H.; Hor, Y. S.; Allred, J.; Williams, A. J.; Qu, D.; Checkelsky, J. *et al.* Extreme Sensitivity of Superconductivity to Stoichiometry in $Fe_{1+\delta}Se$ *Phys. Rev. B* **2009**, *79*, 014522 (7 pages).

(16) Margadonna, S.; Takabayashi, Y.; McDonald, M. T.; Kasperkiewicz, K.; Mizuguchi, Y.; Takano, T.; Fitch, A. N.; Suard, E.; Prassides, K. Crystal Structure of the New $FeSe_{1-x}$ Superconductor. *Chem. Commun.* **2008**, 5607-5611.

(17) Gresty, N. C.; Takabayashi, Y.; Ganin, A. X.; McDonald, M. T.; Claridge, J. B. Giap, D.; Mizuguchi, Y.; Takano, Y.; Kagayama, T.; Ohishi, Y. *et al.* Structural Phase Transitions and Superconductivity in $Fe_{1+\delta}Se_{0.57}Te_{0.43}$ at Ambient and Elevated Pressures. *J. Am. Chem. Soc.* **2009**, *131*, 16944-16952.

(18) Medvedev, S.; McQueen T. M.; Troyan, I. A.; Palasyuk, T.; Eremets M. I.; Cava R. J.; Naghavi, S.; Casper, F.; Ksenofontov, V.; Wortmann, G. *et al.* Electronic and Magnetic Phase Diagram of Beta-$Fe_{1.01}Se$ with Superconductivity at 36.7 K Under Pressure. *Nature Mater*. ***2009***, *8*, 630-633.

(19) Margadona, S.; Takabayashi, Y.; Ohishi, Y.; Mizuguchi, Y.; Takano, Y.; Kagayama, T.; Nakagawa, T.; Takata, M.; Prassides, K. Pressure Evolution of the Low-Temperature Crystal Structure and Bonding of the Superconductor FeSe (T_c=37 K). *Phys Rev. B* **2009**, *80*, 064506-064515.

(20) Bezryadin, A. Quantum Suppression of Superconductivity in Nanowires. *J. Phys.: Condens. Matter* **2008**, *20*, 043202-043221.

(21) Bezryadin, A.; Lau, C. N.; Tinkham, M. Quantum Suppression of Superconductivity in Ultrathin Nanowires. *Nature* **2000**, *404*, 971-974.

(22) Tian, M.; Wang, J.; Snyder, J.; Kurtz, J.; Liu, Y.; Schiffer, P.; Mallouk, T. E.; Chan, M. H. W. Synthesis and Characterization of Superconducting Single-Crystal Sn Nanowires. *Appl. Phys. Lett.* **2003**, *8*, 1620-1622.

(23) Moshchalkov, V. V.; Fritzsche, J. Nanostructured Superconductors, World Scientific Publishing Co Pte Ltd, Singapore, 2011, page 257.

(24) Araújo, M. A. N.; García-García, A. M.; Sacramento, P. D. Enhancement of the Critical Temperature in Iron Pnictide Superconductors by Finite-Size Effects. *Phys. Rev. B* **2011**, *84*, 172502 (4 pages).

(25) Dauler, E. A.; Robinson, B. S.; Kerman, A. J.; Yang, J. K. W.; Rosfjord, K. M.; Anant, V.; Voronov, B.; Gol'tsman, G.; Berggren, K. K. Multi Element Superconducting Nanowire Single-Photon Detector. *IEEE Trans. Appl. Supercond.* **2007**, *17*, 279-284.

(26) Imanishi, Y.; Sato, T.; Higashi, T.; Sun, W.; Okubo, S. A Network of Superconducting Gravimeters Detects Submicrogal Coseismic Gravity Changes. *Science* **2004**, *306*, 476-478.

(27) Hadfield, R. H. Single-Photon Detectors for Optical Quantum Information Applications. *Nat. Photonics* ***2009***, *3*, 696-705.

(28) Marsili, F.; Najafi, F.; Dauler, E.; Bellei, F.; Hu, X.; Csete, M.; Molnar, R. J.; Berggren, K. K. Single-Photon Detectors Based on Ultranarrow Superconducting Nanowire. *Nano. Lett.* **2011**, *11*, 2048-2053.

(29) Wendin, G.; Shumeiko, V. S. Toward Tunable Superconducting Electronics. *Science* **2001**, *292*, 231-232.

(30) Shein, I. R.; Enyashin, A. N.; Ivanovskii, A. L. Nanotubes of Layered Iron-Based Superconductors: Simulations of Atomic Structure and Electronic Properties. *Comput. Mater. Sci.* **2011**, *50*, 824-827.

(31) Wang, J. G.; Tian, M. L.; Kumar, N.; Mallouk, T. E. Controllable Template Synthesis of Superconducting Zn Nanowires with Different Microstructures by Electrochemical Deposition. *Nano Lett.* **2005**, *5*, 1247-1253.

(32) Xu, K.; Heath, J. R. Long Highly-Ordered High-Temperature Superconductor Nanowire Arrays. *Nano Lett.* **2008**, *8*, 3845-3849.

(33) Nath, M; Parkinson, B. A. A Simple Sol–Gel Synthesis of Superconducting MgB_2 Nanowires. *Adv. Mater.* **2006**, *18*, 1865-1868.

(34) Wu, Y.; Messer, B.; Yang, P. Superconducting MgB_2 Nanowires. *Adv. Mater.* **2001,** *13,* 1487-1489.

(35) Oyler, K. D.; Ke, X.; Sines, I. T.; Schiffer, P.; Schaak, R. E. Chemical Synthesis of Two-Dimensional Iron Chalcogenide Nanosheets: FeSe, FeTe, Fe(Se,Te), and $FeTe_2$. *Chem. Mater.* **2009**, *21*, 3655-3661.

(36) Pol, S. V.; Pol, V. G.; Gedanken, A. Synthesis of Ferromagnetic Core-Shell Nanofibers. *J. Phys. Chem. C* **2007**, *111*, 16781-16786.

(37) Han, Y.; Li, W. Y.; Cao, L. X.; Zhang, S.; Xu, B.; Zhao, B. R. Preparation and Superconductivity of Iron Selenide Thin Films. *J. Phys. Condens. Mat.* **2009**, *21*, 235702-235706.

(38) Hamdadou, N.; Bernede, J. C.; Kheli, A. Preparation of Iron Selenide Films by Selenization Technique. *J. Cryst. Growth* **2002**, *241*, 313-319.

(39) Williams, A. J.; McQueen, T. M.; Cava, R. J. The Stoichiometry of FeSe. *Solid State Commun.* **2009**, *149*, 1507-1509.

(40) Zhou, S. M.; Lou, S. Y.; Wang, Y. Q.; Chen, X. L. Synthesis of Ordered α-FeSe Nanorod Array by CVD and its High T_c. *Mater. Lett.* **2011**, *65*, 1741-1747.

(41) Patterson A. L. The Scherrer Formula for X-Ray Particle Size Determination. *Phys. Rev*. **1939**, *56*, 978-981.

(42) Jankovic, L.; Gournis, D.; Trikalitis, P. N.; Arfaoui, I.; Cren, T.; Rudolf, P.; Sage, M. -H.; Palstra, T. T. M.; Kooi, B.; Hosson, J. D. *et al.* Carbon Nanotubes Encapsulating Superconducting Single-Crystalline Tin Nanowires. *Nano Lett.* **2006**, *6*, 1131-1135.

(43) Kim, J. H.; Oh, N.; Kim, C. K.; Yoon, C. S. Area-Selective Growth of Amorphous Carbon Nanofibers *via* Catalytic Decomposition of Polyimide Thin Film. *Chem. Commun.* **2007**, 4018-4020.

(44) Kwok. K.; Chiu, W. K. S. Growth of Carbon Nanotubes by Open-Air Laser-Induced Chemical Vapor Deposition. *Carbon* **2005**, *43*, 437-446.

(45) Okamoto, H.; Massalski, T. B. The Au-Pd (Gold-Palladium) System. *Bull. Alloy Phase Diagram* **1985**, *6*, 229-235.

(46) Okamoto, H.; Massalski, T. B.; Swartzendruber, L. J.; Beck, P. A. The Au-Fe (Gold-Iron) System. *Bull. Alloy Phase Diagram* **1984**, *5*, 592-600.

(47) Raub, E.; Beeskow, H.; Loebich, O. The Iron-Palladium Phase Diagram below 950 ºC. *Z. Metallkunde* **1963**, *54*, 549-552.

(48) Takabataki, T.; Ishikawa, M.; Jorda, J. L. Superconductivity and Phase Relations in the Pd-Se System. *Technical Report of ISSP, Tokyo*, **1987**, *134*, 79-89.

10. SUPPORTING INFORMATION

Element	Weight%	Atomic%
C K	16.58	52.08
Fe L	40.75	27.53
Se L	42.67	20.39
Totals	100.00	

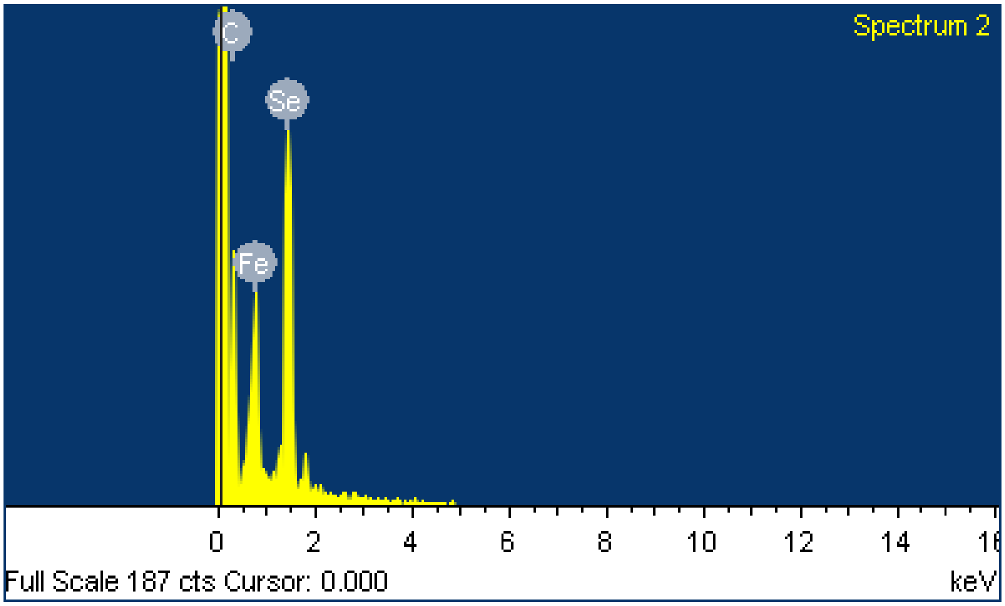

Figure 10.1 EDAX spectra of the black powder on Si substrate showing the presence of elemental Fe and Se.

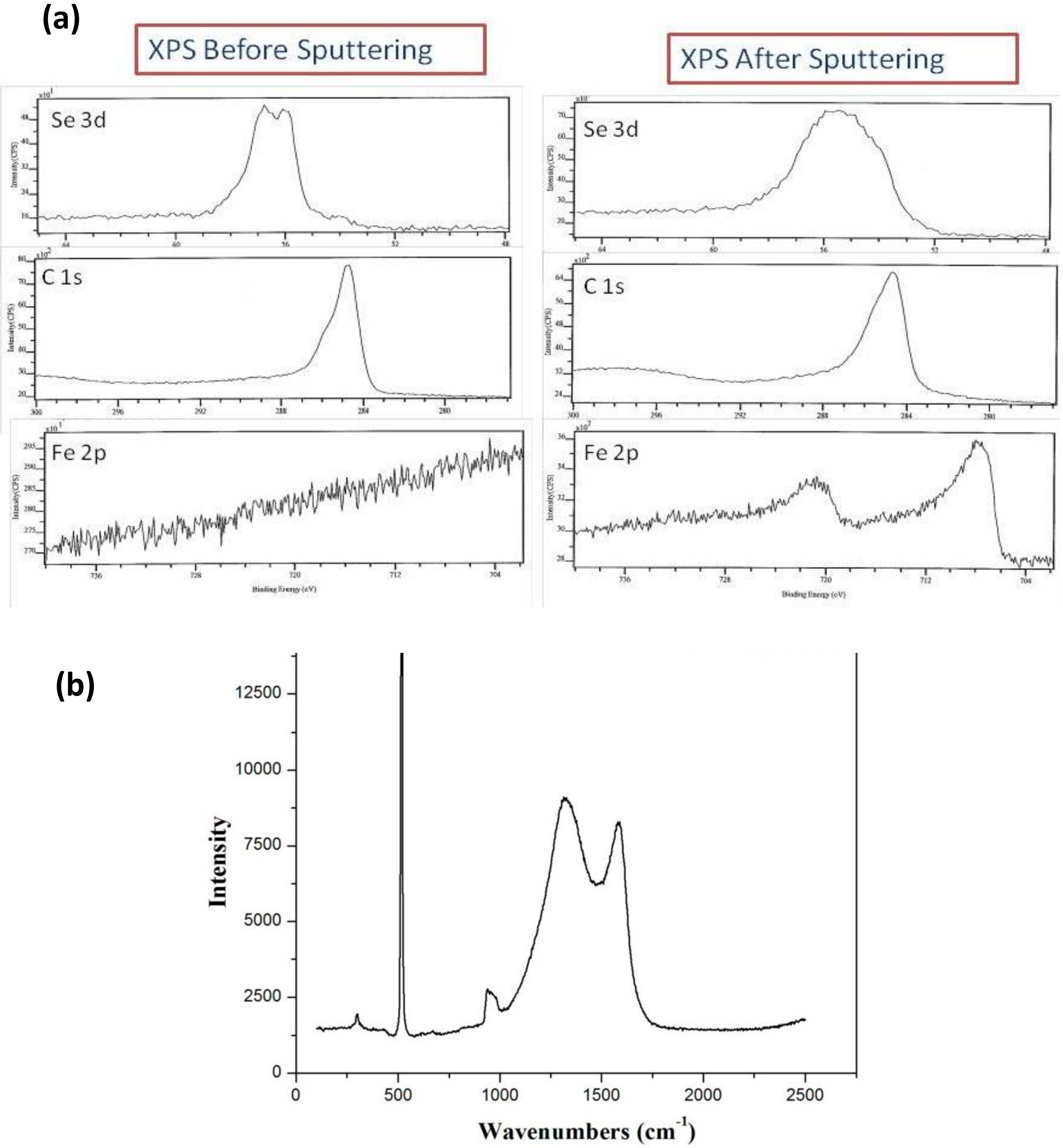

Figure 10.2 (a) XPS spectra of FeSe nanocables before and after sputtering. Sputtering of the sample was performed for 20 minutes which got rid of 20nm surface layer of the nanocables. XPS confirmed the presence of carbon nanotubes as a shell and FeSe as a core, forming the nanocables. (b) Raman spectra showing the presence amorphous carbon.

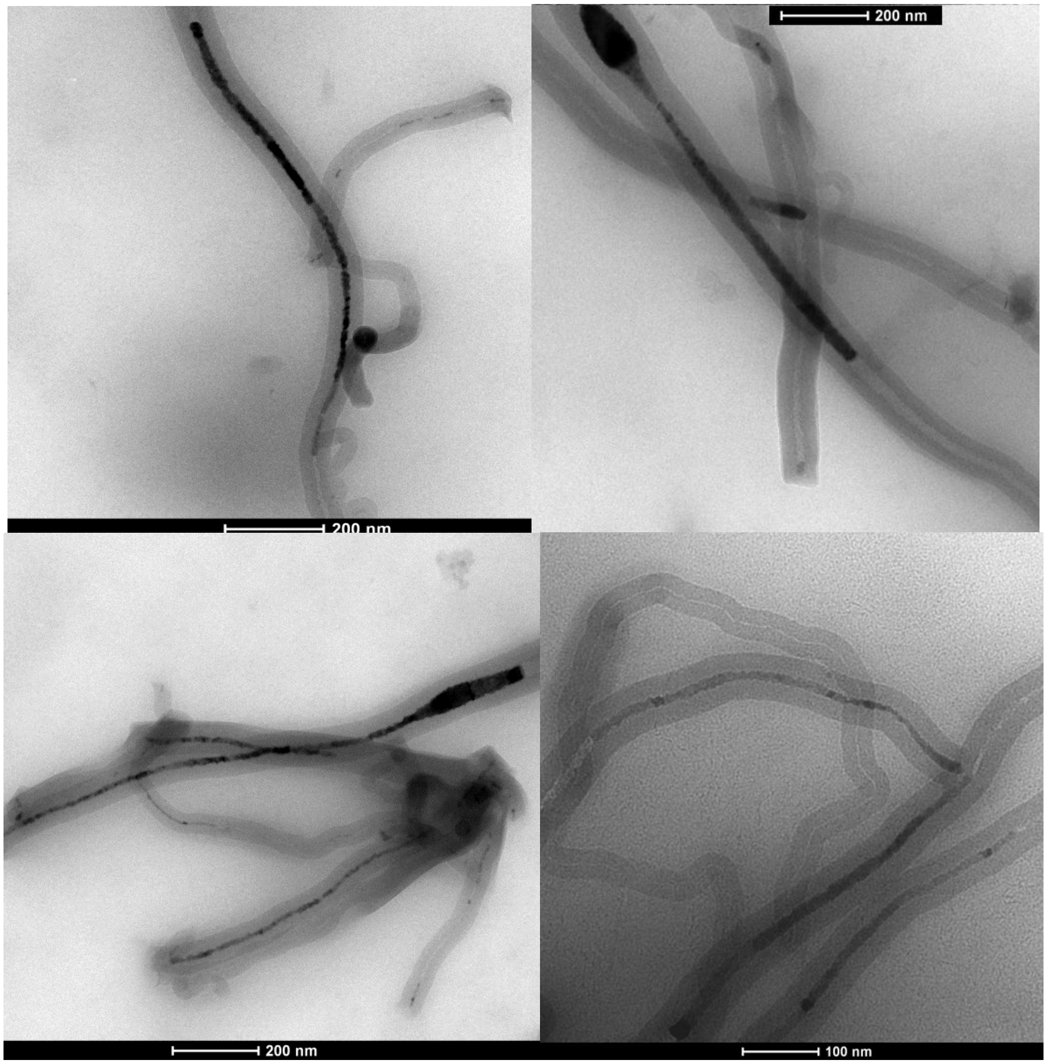

Figure 10.3 STEM images of the nanocables, showing maximum filling of FeSe inside the carbon nanofibers.

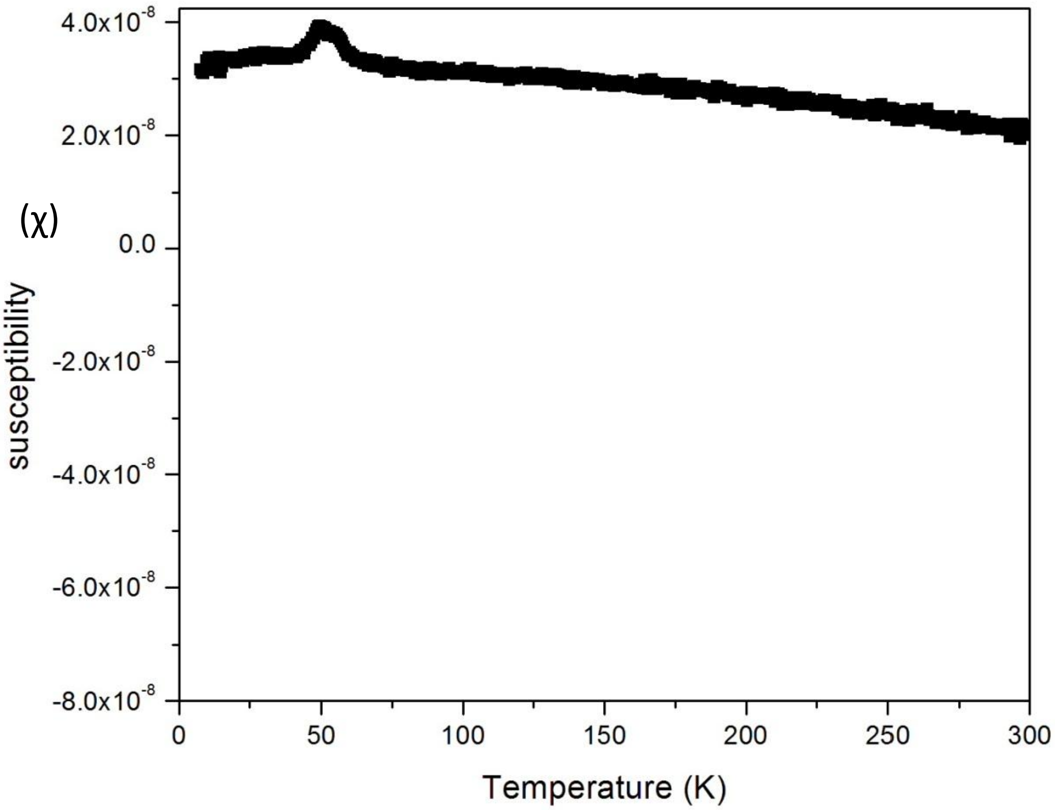

Figure 10.4 Graph of susceptibility vs. temperature for a blank Si substrate.

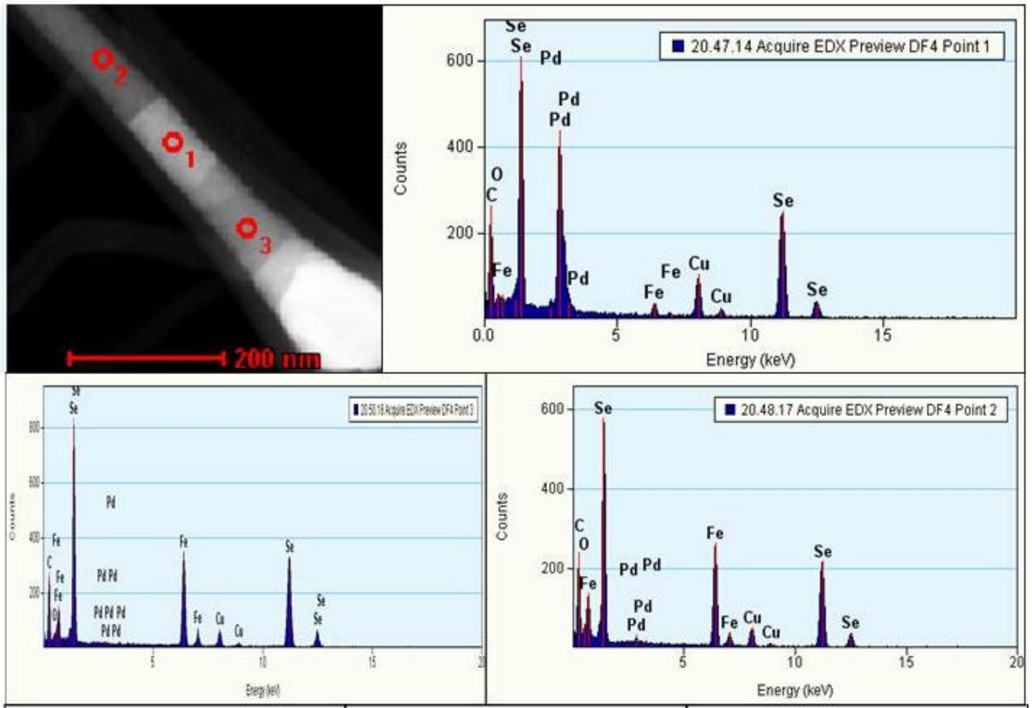

	POINT 1			POINT 2			POINT 3	
Element	Weight %	Atomic %	Element	Weight %	Atomic %	Element	Weight %	Atomic %
C(K)	13.64	52.39	C(K)	25.71	64	C(K)	16.05	52.06
O(K)	0.5	1.44	O(K)	2.66	4.97	O(K)	0.52	1.27
Fe(K)	1.8	1.48	Fe(K)	22.7	12.15	Fe(K)	23.9	16.66
Cu(K)	7.88	5.72	Cu(K)	4.98	2.34	Cu(K)	5.37	3.29
Se(K)	39.51	23.07	Se(K)	42.73	16.17	Se(K)	54.14	26.7
Pd(L)	36.64	15.87	Pd(L)	1.2	0.33	Pd(L)	0	0

Figure 10.5 Figure shows the spot EDS analysis performed across the nanocables on various points. The tables show elemental quantification data acquired from the corresponding points.

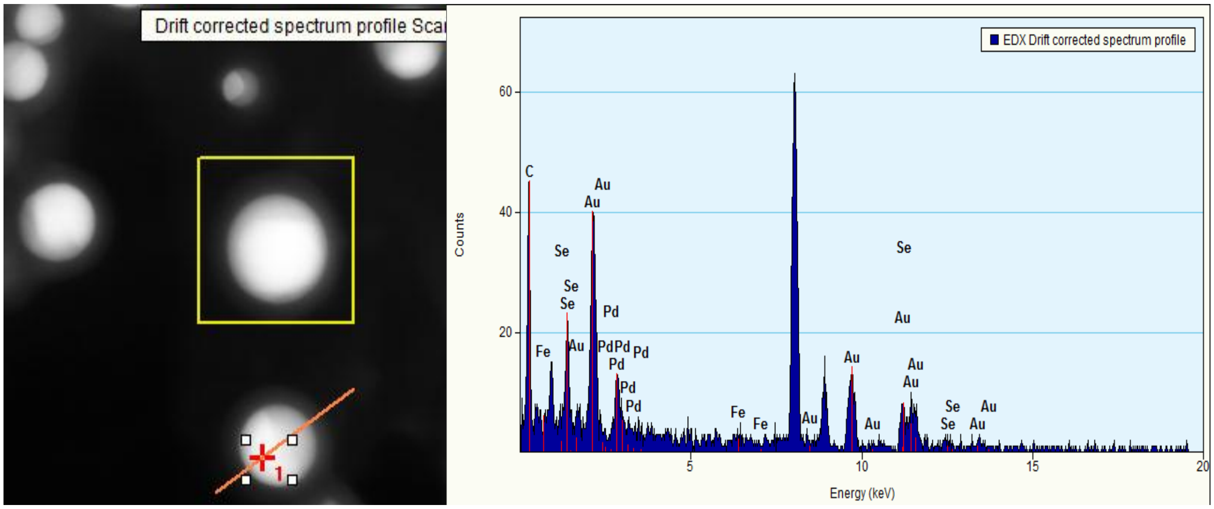

Figure 10.6 Figure shows EDS point analysis performed on a region of the bimetallic catalyst formed at 600°C, demonstrating high Au and Pd signal, as well as showing the presence of Se and trace amount of Fe.

II. ENHANCEMENT OF SUPERCONDUCTING T_C (33 K) BY ENTRAPMENT OF FeSe IN BIPHASIC, CARBON COATED AU—$PD_{17}Se_{15}$ NANOPARTICLES

Submitted to Advanced Materials

*By Sukhada Mishra, Kai Song, Kartik Ghosh and Manashi Nath**

[*] Dr. M. Nath, S. Mishra.
Department of Chemistry, Missouri University of Science and Technology,
Rolla, MO 65409—USA
E—mail: nathm@mst.edu

Dr. K. Song.
Materials Research Centre, Missouri University of Science and Technology,
Rolla, MO 65409—USA
Current Address: FEI Company, 5350 NE Dawson Creek Drive, Hillsboro, Oregon
97124—USA

Dr. Kartik Ghosh.
Physics, Astronomy and Material Science Department
Missouri State University
Springfield MO 65897—USA

Keywords: FeSe nanoparticles, Core—shell nanoparticles, Superconducting FeSe, enhancement in T_c, Pressure effect

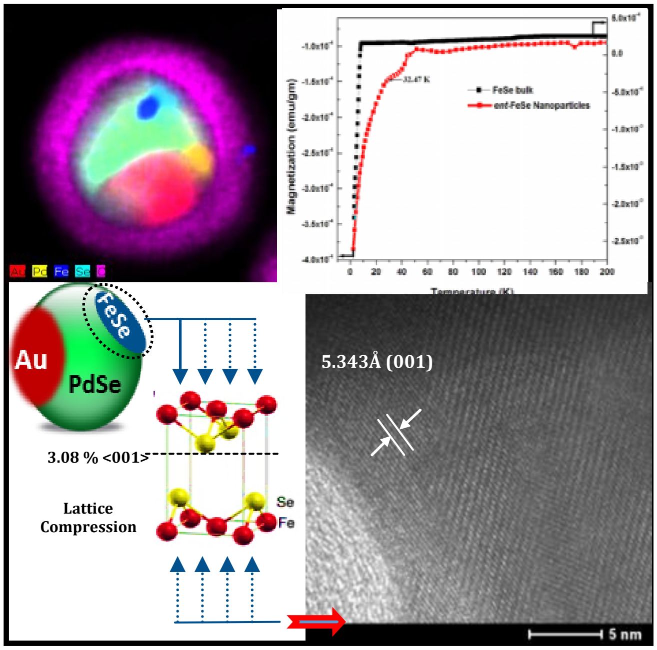

Due to the confinement of FeSe in core—shell Au—$Pd_{17}Se_{15}$@C nanoparticles an internal pressure is induced on layered FeSe, as an effect a notable lattice compression of FeSe (001) and (101) planes is observed through intense high resolution TEM characterizations. Interestingly, an enhancement in superconducting onset Tc=32K is also observed.

1. INTRODUCTION

The discovery of superconductivity in a simple binary compound, FeSe at 8K[1] enriched the family of Fe—based superconductors which started with Hosono's report of superconductivity in the layered iron oxypnictide LaFePO.[2] All these Fe—based superconductors contain analogous crystal structures where the tetrahedral coordination of Fe to the pnictogen (or chalcogen) ion is the main structural ingredient. In the pnictogen based superconducting families, the cationic layers are alternately stacked between the Fe–containing anionic layers, while in FeSe, the crystal structure consists of electronically active layers formed through edge sharing of Fe_2Se_2 tetrahedra[3,4]. In the layered structure, $FeSe_4$ tetrahedra is distorted from its regular shape and the layers are loosely bound to each other through van der Waals interactions giving rise to an inhomogeneous compressibility in the structure.[5,6] Interestingly, when an external pressure of 1.5 GPa[7] was applied to FeSe, a 10% reduction in the unit cell parameters led to the contraction of interlayer separation (in the *c*—direction) and enhanced the T_c from 8K to 36.7K.[6,7] Among all the iron based superconductors, FeSe exhibits largest pressure—sensitivity and shows the highest enhancement of T_c under external pressure.[6] The enhancement in T_c and corresponding structural transitions in FeSe under the application of external pressure has been studied extensively following the initial report by Cava and co—workers.[7,8] Based on the several reports, it is evident that the application of pressure compresses the crystal structure of tetragonal FeSe along the *c*—axis (i.e. layer stacking direction) thereby, decreasing the unit cell volume. The anion height also plays an important role in the enhancement of T_C under high pressure. As pressure is applied, the selenium height decreases leading to an enhancement of T_C.[5] As the pressure is amplified further from 11.5 GPa to 16 GPa, the tetragonal phase of FeSe irreversibly[6] transforms into more densely packed hexagonal[5,6] phase which destroys superconductivity.

The effect of applying external pressure can be also induced through chemical doping (*chemical pressure*),[8—11] confining morphology or by introduction of an interphase.[12] Among these the effect of confined morphology on the superconducting properties including T_C deserves special mention. Previous researchers have reported that that the superconducting parameters can be altered upon nanostructuring, e.g. a 5% enhancement in T_C and 160—400 times higher H_c has been observed for zero dimensional 'In' nanoparticles;[13,14] 60—120 times higher H_c observed for Pb nanoparticles,[15] enhanced T_C and critical field for TaC nanoparticles;[16] and a significantly higher T_C for an array of YBCO nanowires.[17] Recently few reports on FeSe nanostructures suggest that a slight enhancement in T_C (≈10K) with high critical current density was observed for FeSe nanowires,[18] while a significantly higher onset of T_C (≈ 30K) was observed for a film containing FeSe nanoparticles.[19] Following this study, another report claimed that a dramatic enhancement of onset Tc ≈ 53K [20] could be obtained from few layers of FeSe grown over $SrTiO_3$ (STO) substrate, and they predicted that the T_C can be further increased up to 80K by growing a thin film containing a single unit cell layer of FeSe on the STO. This enhancement of T_C was attributed mainly due to the enhanced electron—phonon coupling at the FeSe/STO interphase. Recently, we have also synthesized superconducting FeSe nanocables through chemical vapour deposition (CVD) catalysed by Au—Pd nanoparticles.[12] During this study we observed that the FeSe near the Pd–interface showed a significant lattice compression along the *c*—direction. This lattice contraction was maximum near the interface and decreased further along the FeSe length and expectedly the effect on T_C was very minimal.[12] Hence, we redesigned the experiments in an attempt to confine the FeSe nano—structure growth entirely near the catalyst (Pd) interface, such that the entire FeSe is under lattice contraction. In this communication we describe the synthesis of entrapped [FeSe–$Pd_{17}Se_{15}$–Au]@C nanoparticles (200–250 nm in diameter) where the trapped FeSe (*ent*–FeSe) shares an interface with $Pd_{17}Se_{15}$ and occupies a region of 30–50 nm near the interface. Magnetic characterization showed that an ensemble of these nanoparticles was superconducting with a T_C onset at ~33K, which is four times higher than that for bulk FeSe.

The composite nanoparticles containing *ent*—FeSe was synthesized by catalysed aided chemical vapour deposition, following a procedure reported previously.[12] An Au:Pd (3:2) alloy was used as a catalyst for the FeSe nanostructure growth. In a typical CVD assembly, silicon substrate sputter coated with Au—Pd (3:2) was kept at the isothermal region of the horizontal furnace at 800°C. The reaction assembly was maintained under continuous flow of N_2 at 120 sccm using mass flow controller. Iron(III) tris(acetylacetonate) [$Fe(acac)_3$] and elemental selenium were chosen to be the precursors for Fe and Se respectively. Se shots were positioned at 400°C while $Fe(acac)_3$ was kept at 180°C region to maximize their transport to the reaction zone. Upon completion of reaction a golden brown film was observed on the silicon substrate. To study the morphology, elemental compositions and superconducting transition temperature (T_c) the product was further characterized through powder X—Ray Diffraction (pxrd), scanning electron microscopy (SEM), scanning tunnelling electron microscopy (STEM), high resolution transmission electron microscopy (HRTEM), energy dispersive spectrometry

(EDS), superconducting quantum interference device (SQUID), Raman spectroscopy, Mossbauer spectroscopy and X—ray photoelectron spectroscopy (XPS).

The pxrd of the as—synthesized product as shown in Figure 1.1a confirmed the presence of tetragonal FeSe (JCPDS card number: 04–001–9129) along with cubic $Pd_{17}Se_{15}$ (JCPDS card number: 01–074–6160) and Au in the brownish deposit covering the Si substrate. As the nanoparticles were dispersed as a thin film on Si substrate, owing to small amount of scattering values and high obstructive scattering noise from the Si substrate, weak intensities were obtained in pxrd pattern. SEM characterization was performed directly with the product spread over the Si substrate. Figure 1.1b demonstrates the low magnification SEM image, showing homogenous layer of nanoparticles covering the Si substrate. Figure 1.1c shows a magnified view of these nanoparticles demonstrating core—shell type of distinctive morphology. From the histogram analysis collected from several low magnification SEM images, the sizes of the nanoparticles were observed to be in the range of 200—250 nm (inset of Figure 1.1c). The nanoparticle morphology was similar to that observed by heating the catalyst particles at low temperature (600 ºC) which exhibited a distinct segregation of the bimetallic catalyst into Au and Pd/Se—rich zones, thereby forming an eye—ball kind of morphology (Figure 4.1). Hence, phase segregation was also expected in the composite nanoparticles obtained in the present study. EDAX analysis from these nanoparticles revealed that individual nanoparticles were composed of Fe, Se, Pd, Au and C. To get a better insight into the regional presence

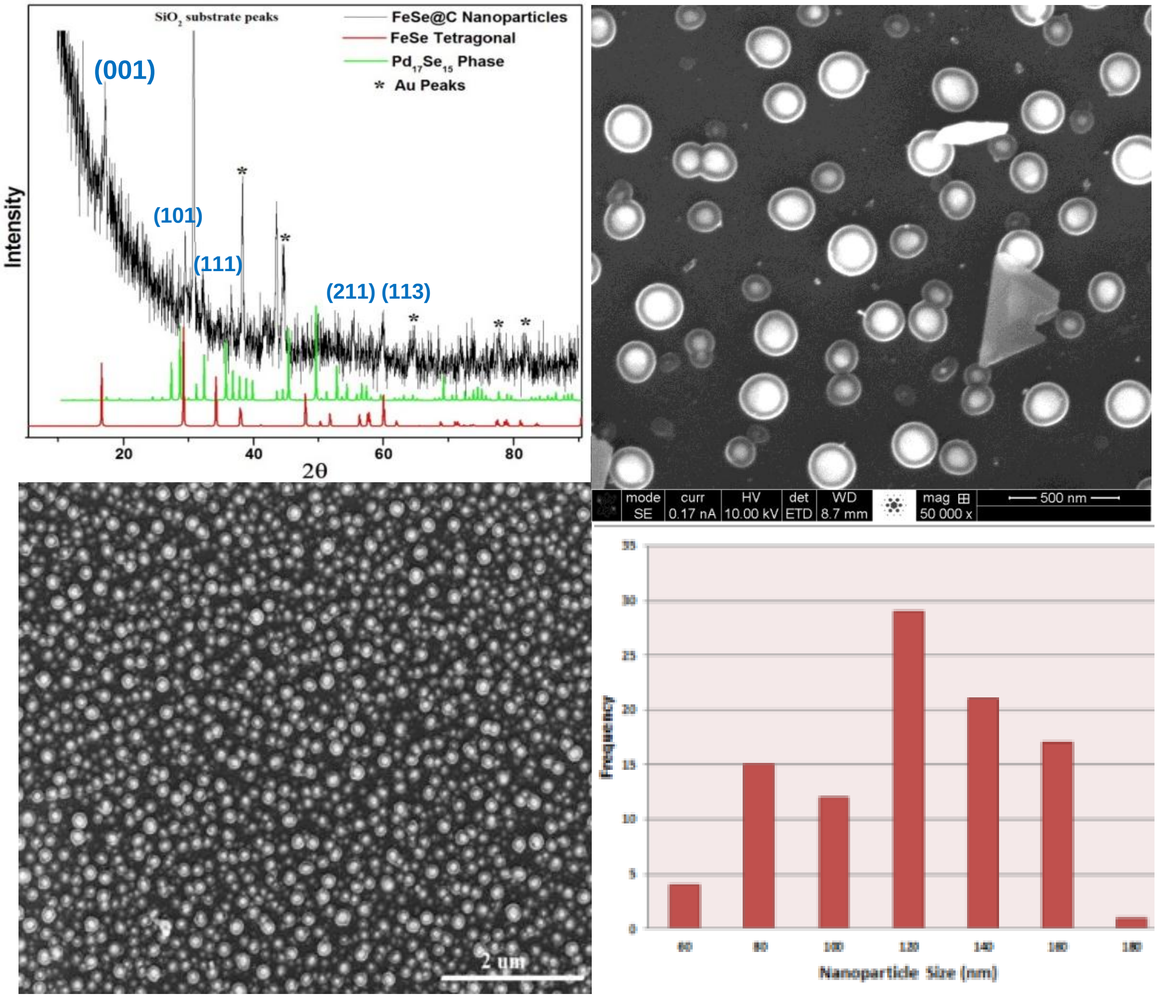

Figure 1.1 (a) XRD pattern of the product showing the presence of tetragonal FeSe and cubic $Pd_{17}Se_{15}$ phase along with the Au peaks. (b) SEM image demonstrating the yield of the nanoparticles on the Si substrate. (c) Magnified SEM image of the Si substrate containing nanoparticles, showing the presence of core-shell type of morphology of the nanoparticles.

of the constituent elements, the nanoparticles were subjected to detailed line scan and elemental mapping analysis in the SEM as shown in Figure 1.2. Figure 1.2(b—e) shows the line scan performed across the line drawn on the nanoparticle shown in Figure 1.2a. The presence of Au was demonstrated in the bright contrast region as shown in Figure 1.2b. The occurrence of Pd and Se in the middle region confirmed the formation of a Pd/Se alloy (Figure 1.2c, 2d). Interestingly, the Fe signal picks up from the other end of the nanoparticle, opposite to the Au catalyst region (Figure 1.2e). Figure 1.2 (f–j) shows the elemental mapping performed on the same particle. It demonstrates carbon signal on the entire particle, suggesting the presence of carbon as a coating on the nanoparticle. The Au, Pd—Se and Fe—Se regions were analogous to the elemental analysis performed through line scans which illustrated that the Fe—rich region was on the Pd—rich zone and away from the Au. Extensive elemental mapping and line scan analysis was performed on several nanoparticles to get the global picture and also by tilting individual nanoparticles in the TEM imaging process. Elemental mapping performed after tilting the nanoparticles (up to +/—20º) in the TEM sample stage further confirmed that the FeSe regions were always adjacent to the Pd—region of the catalyst and away from the Au—rich zone and also gave an approximate idea about the 3–dimensional architecture of these composite nanoparticles. Figure 1.3 shows a schematic representation comparing the experimental elemental mapping with the probable compositional morphology of these nanoparticles. Depending on the viewing direction, the FeSe region can be very prominent right on top of the nanoparticles as shown in the experimental mapping image in Figure 1.3b, while Figure 1.3a shows the probable morphology. The same nanoparticle if viewed atop the Au region (which can be achieved by tilting the sample stage), the

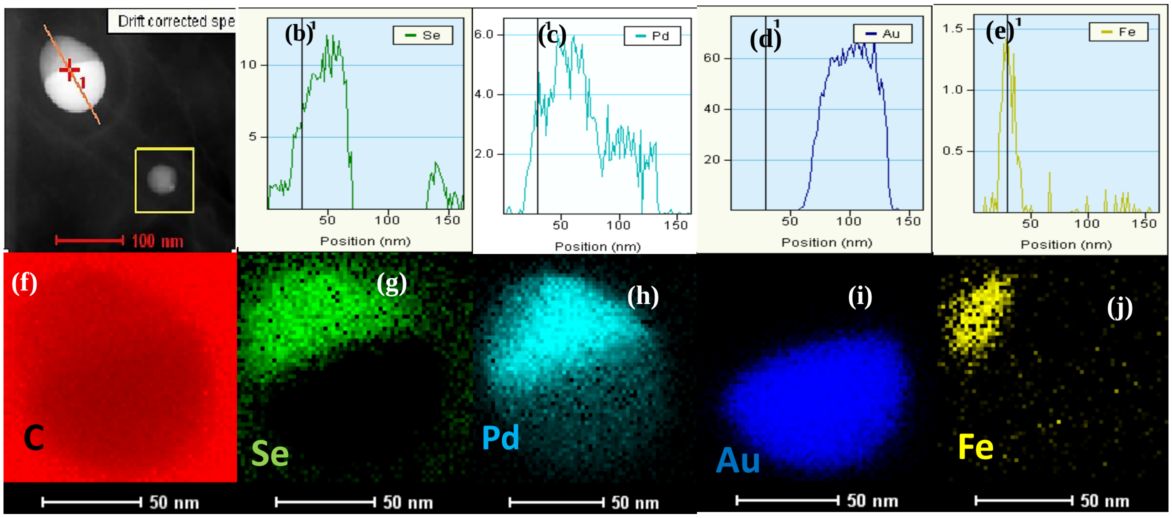

Figure 1.2 (a-e): Elemental line mapping showing the elemental distribution of Au, Pd, Fe, Se from across the line drawn from position 1 to position 2, over a single nanoparticle. (f-j) Elemental mapping of the corresponding nanoparticle demonstrating the presence of Au region, Pd/Se rich region, and Fe/Se rich region.

FeSe region was shifted to the very edge (Figure 1.3d showing the experimental mapping analysis, while 3c shows the schematic representation) or was totally masked by the over—lying Pd–Se and Au regions (Figure 1.3e). From these detailed analysis it was confirmed that the *ent*–FeSe in these nanoparticles was indeed confined between the $Pd_{17}Se_{15}$ on one side and the carbon shell on the other side, and had a large interface with the $Pd_{17}Se_{15}$.

The composition of the nanoparticles and the shell was also confirmed through XPS and Raman spectral analysis. XPS analysis was performed on these composite nanoparticles in two modes— (1) without sputtering the sample and (2) with sputtering the sample. Sputtering of the sample was performed for 20 minutes which removed approximately 20 nm surface layer of the nanoparticles. Elemental analysis and the quantification results (Supplementary Figure 4.2) confirmed the presence of C, Fe and Se along with the trace amounts of Au and Pd catalyst which remained unchanged after sputtering. Upon careful at 1315.83 cm^{-1} and 1581.63 cm^{-1}, respectively, also confirmed the presence of carbonaceous shell in the form of disordered carbon (I_D/I_G ~ 3.08).

Extensive HRTEM analysis was carried out to investigate the structural details of individual regions in these nanoparticles. Figure 1.4 (a–d) shows the HRTEM images acquired from the different regions (R1–R4) of *ent*—FeSe—$Pd_{17}Se_{15}$—Au@C nanoparticle. Figure 1.4a shows bright field TEM image of a single *ent*—FeSe—$Pd_{17}Se_{15}$—Au@C nanoparticle, showing three distinct regions of different contrasts. As confirmed from the line mapping and elemental mapping, the darkest region denoted by R1 corresponds to the Au—region, while the middle region of the nanoparticles represented the uniform Pd/Se phase (R2 in the image). It was also evident that the FeSe regions were concentrated at the periphery of the nanoparticles in R3 and R4 regions respectively. Figure 1.4b shows HRTEM image of the Au region showing lattice spacing of 2.35 Å corresponding to the [111] plane of Au. The SAED obtained from the Au region also confirmed the presence of single crystalline Au and the diffraction spots could be indexed to <$1\bar{1}1$ > and <220> planes. Figure 1.4c shows the HRTEM image obtained from the R4 region, where the lattice fringes and electron diffraction obtained from Fast Fourier Transform (FFT) (shown in inset) confirmed the presence of tetragonal FeSe. The zone axis being [111], the spots could be indexed to <001>, <010> and <101> lattice planes of tetragonal FeSe. Interestingly, the calculated d—spacing along these planes corresponds to 5.343, 3.469 and 2.81 Å respectively, which demonstrated 3.08%

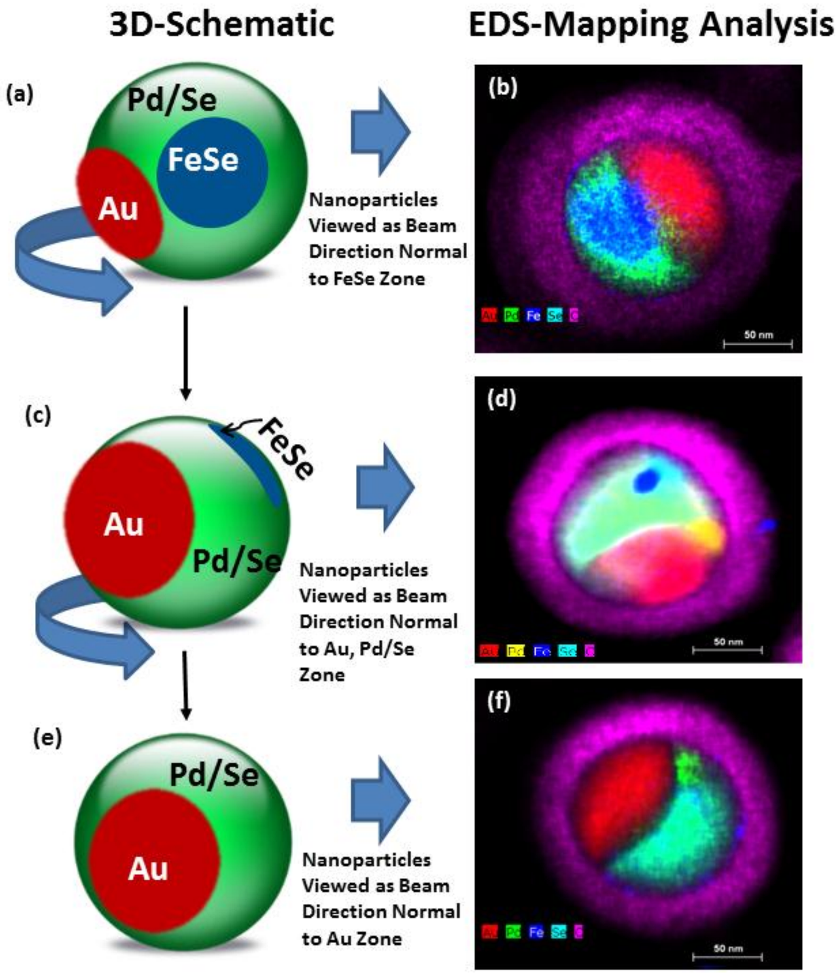

Figure 1.3 (a) Graphical representation of the *ent*-FeSe-$Pd_{17}Se_{15}$-Au@C nanoparticles across different direction of views observed during TEM imaging. (b) EDS mapping performed on the nanoparticle having FeSe region perpandicular to the direction of electron beam. (c) EDS mapping performed on the nanoparticles having the FeSe concentrated at the edges.

lattice contraction along *c*—direction (reported value of 5.51 Å), 8.22% compression along <010> (reported value of 3.77 Å)and 10.79% lattice compression along <101> (reported value of 3.15 Å). Extensive HRTEM images obtained from the FeSe regions near the edge (Region R3) of the nanoparticles also showed the existence of lattice compression of ~9.01% in <101> planes (Supplementary Figure 10.4). For the HRTEM analysis, Si single crystals were used as calibration sample for lattice spacing accuracy and all calculations for lattice spacing were done by counting at least 15 lattice planes. From the extensive HRTEM and SAED analysis it was evident that the FeSe in these nanoparticles showed appreciable lattice compression which might be attributed to the effect of restricted growth and the presence of an interface between the growing FeSe and $Pd_{17}Se_{15}$ as has been observed earlier in the FeSe nanocables.[12]

To study the effect of lattice compression of FeSe on the superconducting transition temperature (T_c), magnetization was measured as a function of temperature under zero field cooled conditions using VSM. Figure 1.5 shows the plot of magnetic susceptibility (χ) as a function of temperature, measured with an applied field of 100 Oe. Measurements were acquired for FeSe—$Pd_{17}Se_{15}$—Au@C nanoparticles and bulk FeSe. Superconducting transition for nanoparticles, was clearly observed at $T_c \approx 33K$ which was higher than the bulk FeSe $T_c=8K$. The measurements were performed on the small piece (3 mm×3 mm) Si substrate containing nanoparticles, hence the Si substrate contributed to the background signal. The resistivity measurements are typically performed by fabricating the contacts on tightly packed powder pallets. But in the case of nanoparticles, the synthesis protocol generates the nanoparticles as dispersed film over Si substrate as shown in Figure 1.5 in this arrangement it is difficult to construct electrical contacts required for resistivity measurements. observation it was evident that intensity of the carbon signal reduced drastically upon sputtering, accompanied by the decrease in atomic weight percentage from 76.76% to 54.92%, which confirmed that the shell composition is primarily carbonaceous. Raman spectroscopy analysis (Supplementary Figure 10.3) which showed the *D* band and *G* band

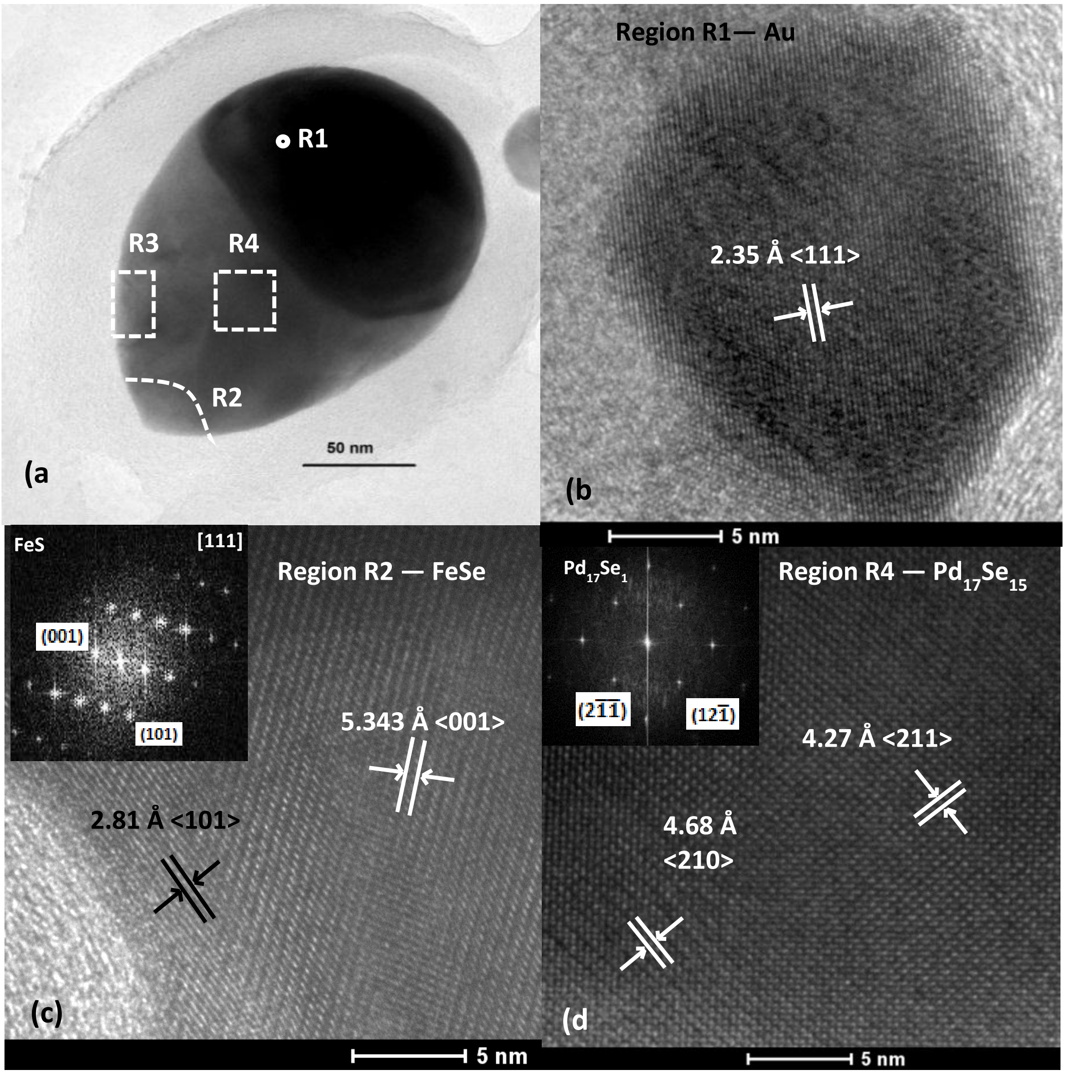

Figure 1.4 (a-d). HRTEM images of FeSe-PdSe-Au@C nanoparticles region collected from different regions in the nanoparticle. (a) Low-magnification image of the nanoparticle showing different regions (R1-Au, R2, R3- FeSe, R4-PdSe). (b) HRTEM image of the Au region (R1), having d-spacing of 2.35 Å corresponding to (111) planes. Inset shows the SAED pattern obtained from different Au region. (c) FeSe region at the edges of nanoparticle (shown by R2) with lattice fringes corresponding to (001) planes showing a spacing of 5.343 Å. Inset shows the FFT generated ED patterns, with diffraction spots corresponding to (001), (101) planes. (d) Lattice fringes obtain from the $Pd_{17}Se_{15}$ region (R4) at the middle of the nanoparticle showing a lattice spacing of 4.27 Å for the (211) planes and 4.68 for (210) lattice planes. Inset demonstrates the FFT generated ED patterns, with diffraction spots corresponding to $(2\bar{1}\bar{1})$, $(12\bar{1})$ planes.

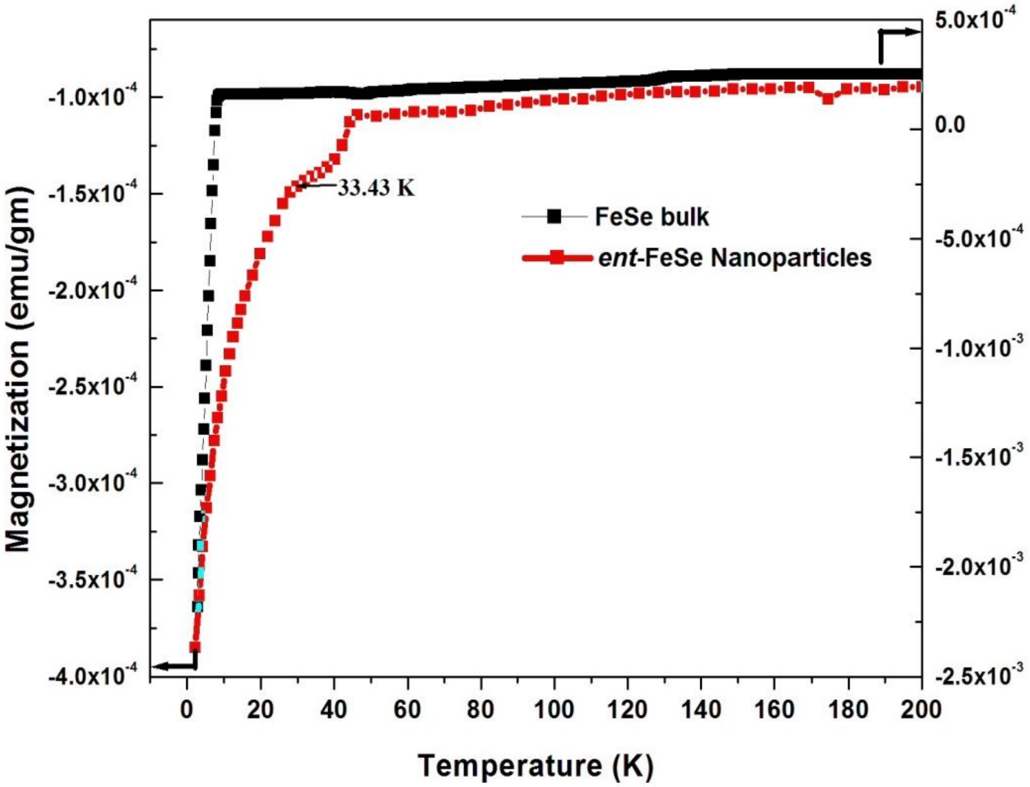

Figure 1.5 Plot of Magnetization Vs Temperature for the *ent*-FeSe-$Pd_{17}Se_{15}$-Au@C nanoparticles showing the onset of the superconductivity at ≈ 33K.

2. CONCLUSION

In conclusion we have developed a protocol for the synthesis of FeSe—PdSe—Au nanoparticles coated with carbonaceous layers. While FeSe nanocables encapsulated by carbon nanotubes demonstrated Tc of 8K, the onset of superconducting temperature is ≈ 33K for the FeSe nanoparticles. When the tetragonal FeSe phase is in close proximity with high electron density Pd/Se phase and encapsulated by carbon shell, the pressure effect which is created by the inherent morphology plays very important role towards the enhancement of the superconducting transition. According to the electronic phase diagram of tetragonal FeSe under pressure provided by Medvedev *et al*;[10] an increase in the T_c accompanies with a reduction in the volume which was addressed to the reduced separation between Fe_2Se_2 layers. The nanoparticles formed using this technique contains combination of tetragonal FeSe/ PdSe and Au, and the HRTEM studies of these nanostructures demonstrates that, the FeSe region possess compression in lattice spacings. This can corresponds to internally create high pressure and it can contribute towards a higher Tc.

Acknowledgements

The authors would like to acknowledge the Materials Research Center, for equipment usage, Dr. Switzer, Dr. Koza for their help with magnetic characterizations and Dr. Brow for help in Raman spectroscopic analysis. (Supporting Information is available online from Wiley InterScience or from the author).

Received: ((will be filled in by the editorial staff))
Revised: ((will be filled in by the editorial staff))
Published online: ((will be filled in by the editorial staff))

3. REFERENCES

[1] F. C. Hsu, J. Y. Luo, K. Y. Yeh, T. K. Chen, T. W. Huang, P. M. Wu, Y. C. Lee, Y. L. Huang, Y. Y. Chu, D. C. Yan, M. K. Wu, *Proc. Natl Acad. Sci.* **2008**, *105*, 1426.

[2] Y. Kamihara, H. Hiramatsu, R. Kawamura, H. Yanagi, T. Kamiya, H. Hosono, *J. Am. Chem. Soc.* **2006**, *128,* 10012. H. Hosono, *J. Phys. Soc. Jpn.* **2008**, *77 Suppl. C,* 1—8.

[3] B. Büchner, C. Hess, *Nat. Mater.* **2009**, *8*, 615.

[4] S. Margadonna, Y. Takabayashi, M. T. McDonald, K. Kasperkiewicz, Y. Mizuguchi, Y. Takano, A. N. Fitch, E. Suarde, K. Prassides, *Chem. Commun.* **2008**, 5607.

[5] H. Okabe, N. Takeshita, K. Horigane, T. Muranaka, J. Akimitsu, *Phys. Rev. B* **2010**, *81,* 205119.

[6] S. Margadonna, Y. Takabayashi, Y. Ohishi, Y. Mizuguchi, Y. Takano, T. Kagayama, T. Nakagawa, M. Takata, K. Prassides, *Phys. Rev. B* **2009**, *80,* 064506.

[7] S. Medvedev, T. M. McQueen, I. A. Troyan, T. Palasyuk, M. I. Eremets, R. J. Cava, S. Naghavi, F. Casper, V. Ksenofontov, G. Wortmann, C. Felser *Nat. Mater.* **2009,** *8*, 630.

[8] N. C. Gresty, Y. Takabayashi, A. X. Ganin, M. T. McDonald, J. B Claridge, D. Giap, Y. Mizuguchi, Y. Takano, T. Kagayama, Y. Ohishi, M. Takata, M. J. Rosseinsky, S. Margadonna, K. Prassides, *J. Am. Chem. Soc.* **2009**, *131*, 16944.

[9] B. Lv, L. Denga, M. Gooch, F. Wei, Y. Suna, J. K. Meen, Y. Y. Xue, B. Lorenz, C. W. Chu, *Proc. Natl. Acad. Sci.* **2011**, *108*, 15705.

[10] K. Kudo, K. Iba, M. Takasuga, Y. Kitahama, J. Matsumura, M. Danura, Y. Nogami, M. Nohara, *Scientific Reports* **2013**, *3*, 1—5.

[11] M. Rietveld, D. Glastra,V. D. Marel, *Physica C* **1995**, *241*, 257.

[12] S. Mishra, K. Song, J. A. Koza, M. Nath, *ACS Nano*, **2013**, *7*, 1145.

[13] W.H. Li, C. C. Yang, F. C. Tsao, S. Y. Wu, P. J. Huang, M. K. Chung, Y. D. Yao, *Phys. Rev. B* **2005**, *72*, 214516.

[14] F.Y. Wu, C. C. Yang, C. M. Wu, C. W. Wang, W.—H. Li, *J. Appl. Phys.* **2007**, *101*, 09G111.

[15] P. Zolotavin, P. Guyot—Sionnest, *ACS Nano* **2010**, *4*, 5599.

[16] K. Xu, J. R. Heath, *Nano Lett.* **2008,** *8*, 3845.

[17] A. Fukunaga, S.Chu, M. E. McHenry, *J. Mater. Res.* **1998**, *13*, 2465.

[18] T. Ozaki, K. Deguchi, Y. Mizuguchi, Y. Kawasaki, T. Tanaka, *J. Appl. Phys.* **2012**, *111*, 112620.

[19] C. —C. Chang, C. –H. Wang, M. –H. Wen, Y. –R. Wu, Y.—T. Hsieh, M.—K. Wu *Solid State Comm.* **2012**, *152*, 649.

[20] W. Qing—Yan *et. al.* Chinese Phys. Lett. **2012**, *29*, 037402.

4. SUPPORTING INFORMATION

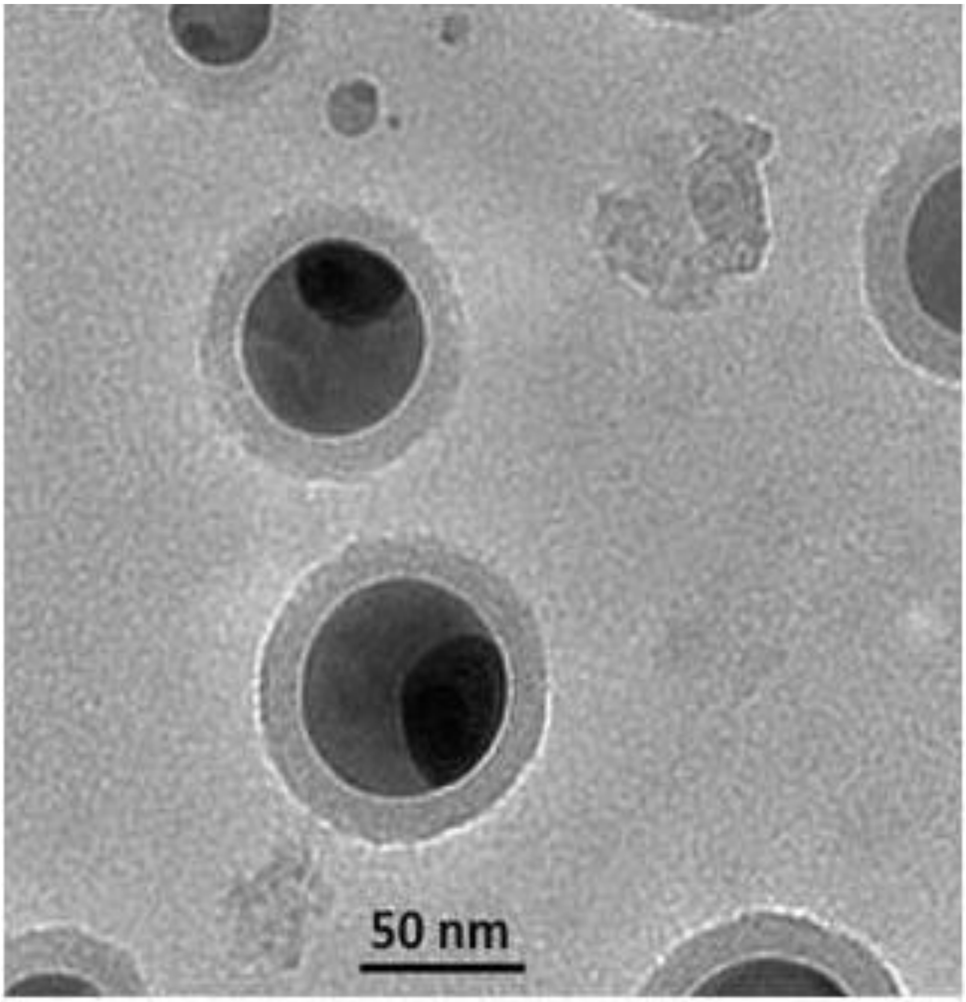

Figure 4.1 SEM image demonstrating eye-ball kind of morphology of the nanoparticle analyzed at lower reaction temperature.

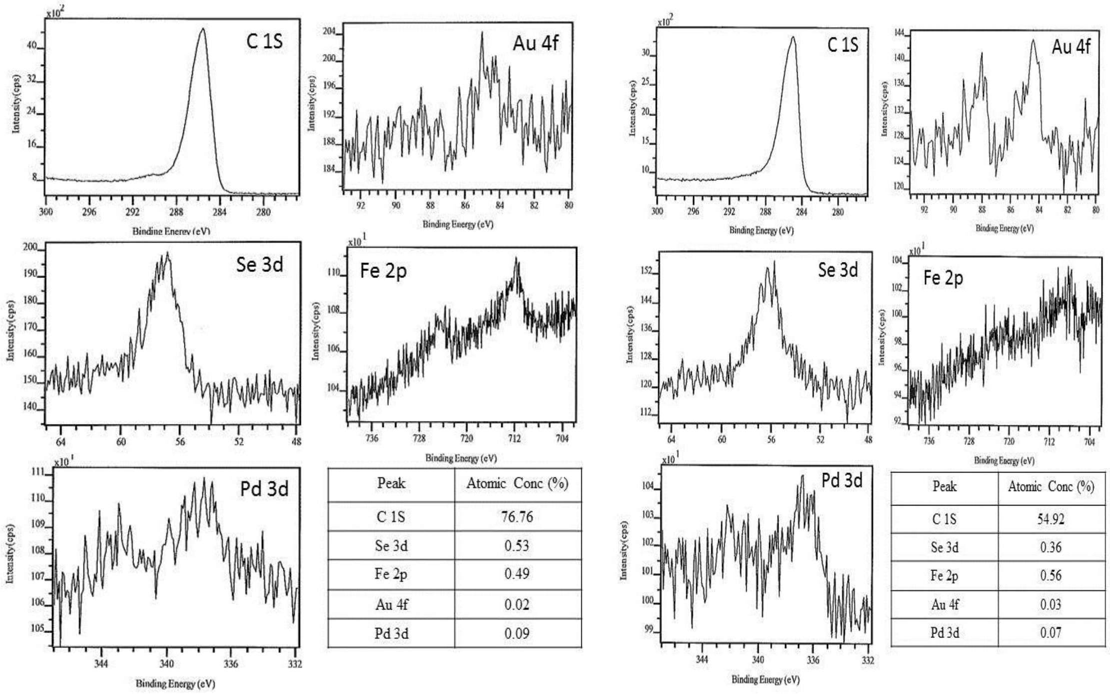

Peak	Atomic Conc (%)
C 1S	76.76
Se 3d	0.53
Fe 2p	0.49
Au 4f	0.02
Pd 3d	0.09

Peak	Atomic Conc (%)
C 1S	54.92
Se 3d	0.36
Fe 2p	0.56
Au 4f	0.03
Pd 3d	0.07

Figure 4.2 XPS spectra of individual elements for the FeSe nanoparticles before sputtering the sample. (f) shows the table of the atomic percentage of the individual elements. 4 (g-k) Showing the XPS spectrum of the elements after sputtering is performed on the FeSe nanoparticles. (l) Table showing the atomic weight percent of the FeSe nanoparticles after sputtering.

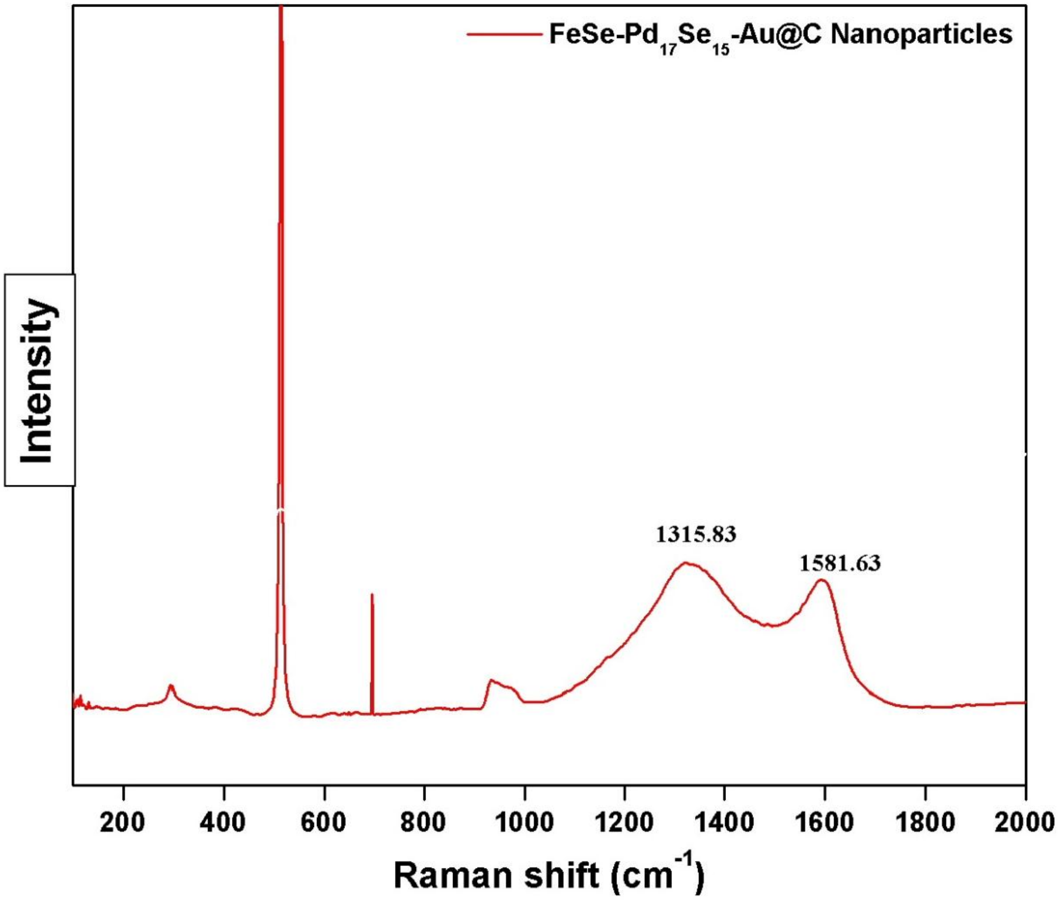

Figure 4.3 Raman spectroscopy collected from the ensemble of nanoparticles showing the Raman shifts characteristic for disordered carbon.

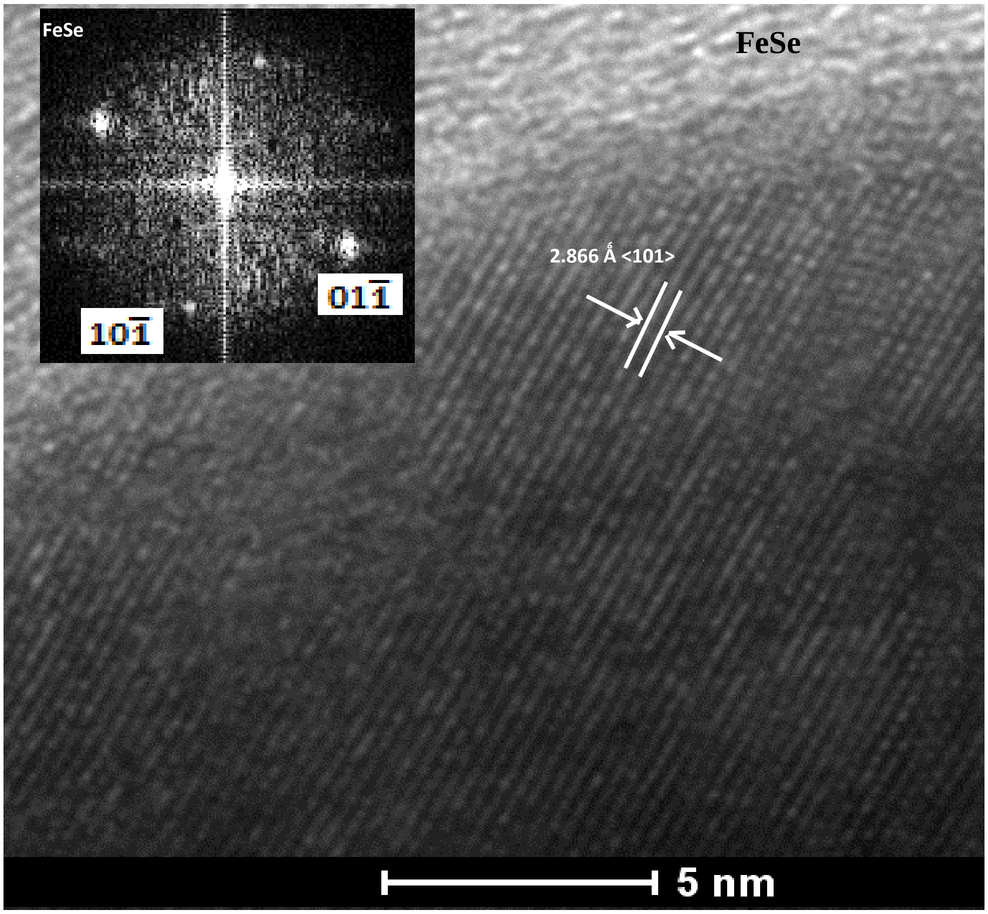

Figure 4.4 HRTEM image collected from region R-4 demonstrating the lattice fringes for 2.866 Å of <101> lattice planes. The inset shows, FFT generated electron diffraction pattern, which can be indexed to $(10\bar{1})$ and $(01\bar{1})$ lattice planes.

III. GROWTH OF VERTICALLY ALIGNED CdTe NANOROD ARRAYS THROUGH PATTERNED ELECTRODEPOSITION

Nano Energy, 2013

Sukhada Mishra, Manashi Nath*

Department of Chemistry, Missouri University of Science and Technology, Rolla, MO, USA, 65409.
Corresponding Author: nathm@mst.edu

We have successfully developed a simple, reproducible and scalable technique for growing CdTe nanorod arrays on conducting surfaces through electrodeposition on patterned nanoelectrodes. The vertically aligned CdTe nanorods grown as arrays over large area were exceptionally homogeneous in terms of their diameter and length. The ensemble of the CdTe nanorod arrays covering an area of approximately 75 x 75 μm^2, exhibited a photocurrent density in the mA range, which was significantly higher than that obtained from a CdTe film with similar coverage grown under analogous conditions. This approach can be further extended to grow complex nanowire composition including heterojunction semiconductor nanowires incorporating a lateral and radial p-n junction by simple modification of the lithography and electrodeposition steps.

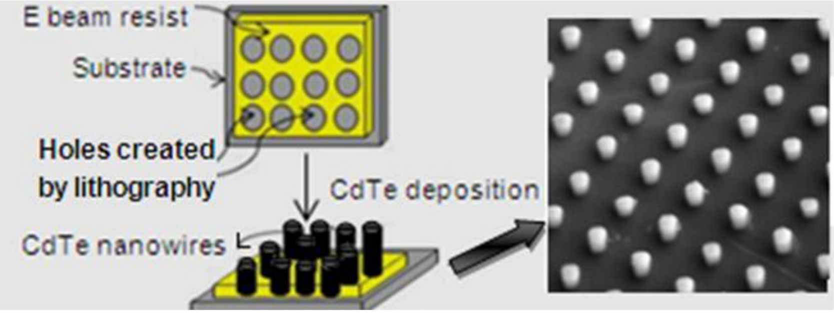

Highlights:

- Produced CdTe nanorod array by electrodeposition on lithographically patterned nanoelectrodes.
- CdTe nanorod arrays showed higher photoelectrochemical response compared to planar thin film.
- The method can be utilized for the fabrication of nanowire arrays on flexible substrates.
- The method can be further modified to grow ordered arrays of complex nanowire architectures.

Keywords: CdTe nanowire, solar cell, patterned growth, photovoltaics.

1 INTRODUCTION

The knowledge that fossil fuel needs to be replaced with alternative sources of sustainable energy has led materials scientists to accelerate research into photovoltaics, where a flurry of research activities has led to the identification of many new compositions.[1-3] For these families it has been shown that the power generation efficiency increases as the material dimension is reduced to the nanometric regime.[4-6] Hence, nanowires expectedly increase the efficiency of the solar cells, since electron transport across single nanowires is much more facilitated than that across a nanoparticle network. A parallel arrangement of high aspect ratio nanowires, where the axis of the nanowires are normal to the incident light is expected to produce a high efficiency solar cell since, this arrangement utilizes sufficient material thickness for efficient light absorption, while simultaneously providing short collection lengths for transport of excited carriers in a direction normal to the light absorption.[7,8] Recently, Borgstrom and coworkers reported the fabrication of highly oriented vertical InP nanowires arrays which demonstrated generation of bulk like photocurrent with an efficiency of 13.8%. In these nanowires, the diameter was confined in the theoretical limit for resonant light trapping in sub 200 nm regions. The ~180 nm diameter InP nanowire arrays produced 83% of the photocurrent density compared to that of planar InP solar cell, despite of having only 12 % coverage.[7] Similarly, other researchers have observed that ordered arrays of Si nanowires increase the path length of the solar radiation by a factor of 73.[8] Other viable and cost effective photovoltaic materials for efficient solar cells are CdTe, CuInSe, $CuIn_{1-x}Ga_xSe_2$ etc. which has appreciable photoconversion efficiencies.[9,10] Among these CdTe is viewed as a promising substitute for Si owing to an appropriate band gap and high solar optical absorption.[11,12] CdTe with a layer thickness of few micrometers is sufficient to absorb all the incident sunlight.[13] In fact, recently CdTe nanocrystals and nanorods when integrated into actual solar photovoltaic geometry with type II heterojunction, showed a 3% power conversion efficiency.[14] However, with the increasing complexity of the photoabsorber layer, periodic arrangement of semiconducting nanowires on conducting substrates is one of the main challenges that needs to be addressed for the advancement of the technological aspect of these functional materials.

The bottom-up approach which aims at pre-synthesis integration where the nanomaterials are grown on specific region of the substrates is more lucrative for producing nanowire arrays of uniform composition. Different methods for the patterned growth of nanowires on the substrate had been employed in the past, which includes confined electrodeposition,[15] deposition inside pores of AAO,[16-18] close space sublimation,[19] vapor transport techniques[20] and soft nanoimprint lithography.[21,22] However, most of these methods are of low-throughput and not economically viable, also the use of hard templates like AAO is sometimes not desirable since template removal requires harsh chemical treatments which are detrimental to the nanowires. Moreover, since the performance of these semiconducting materials is influenced by the properties and composition of the electrode surface, a more generalized technique to grow these semiconductor nanowires on any desired substrate for studying the influence of the substrate-nanowire interface and optimization of device performance is required.

In this article we report a simple, generalized technique to grow semiconductor nanorod arrays on desired regions using CdTe as a model system, where nanorod growth is achieved by electrodeposition on patterned nanoelectrodes defined on ITO coated glass through e-beam lithography. The resulting photovoltaic device containing nanorod arrays exhibited a huge amplification in the photoconversion efficiency, thereby, underlining the effectiveness of the approach. It should be noted here that although thin film of CdTe has been grown by various methods, including electrodeposition by several research groups, [1,2,3,23] however, as per the authors' knowledge, growth of CdTe nanowires as arrays through patterned electrodeposition is very rare. This scalable and reproducible technique executed at room temperature involves simple steps which can be further modified to grow heterojunction nanowires (like *p*-*n* junctions) and other functional semiconductors. The method reported here is ideal for exploring the variable chemical composition of the nanowires as well the nanowire-electrode interface and study their effect on the nanowire performance.

2 EXPERIMENTAL METHODS

The patterned growth of CdTe nanorods comprises of two steps: definition of nanoelectrodes through lithography and nanorod growth by electrodeposition. Indium tin oxide (ITO) coated glass slides of 1cm^2 area were used as substrates. Polymethylmethacrylate (PMMA, supplied by Microchem, MA) was used as *e*-beam resist. For the two layer configuration of the resist on conducting substrate, PMMA (mol. wt. – 975k) was spin coated above the layer of PMMA (mol. wt. – 450k) to obtain a total film thickness of 0.3 µm. Baking was carried out for 6 minutes at 180 °C. Helios Nano Lab 600, dual beam FIB instrument was used to define patterns on the substrate through *e*-beam lithography. Hole sizes of the pattern were varied from 1 µm- 400 nm. After performing lithography, substrates were developed in MIBK-IPA (1:3) solution for 45 sec. This procedure removes the PMMA which has been exposed to the *e*-beam, while the unexposed PMMA remains un-altered. Post-lithography development thereby leads to exposure of the underlying ITO through the lithographically patterned holes, thus forming nanoelectrodes on the substrate. The polymer unexposed to the *e*-beam remains

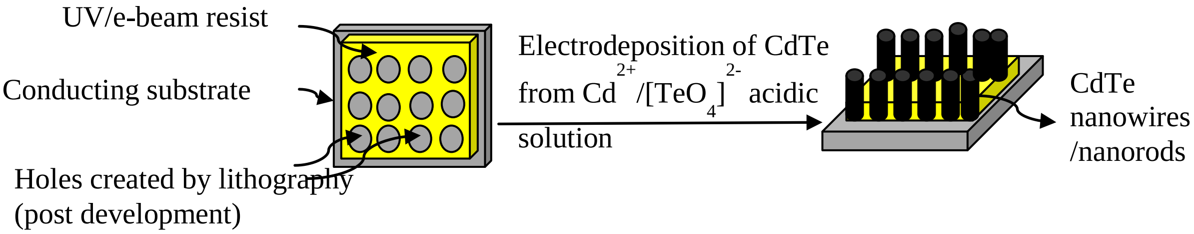

Figure 2.1 Schematic showing the steps for generating CdTe nanorod arrays on ITO coated glass.

intact, acting as a soft mask during electrodeposition of the material. Figure 1.1 shows a detailed schematic of the experiment protocol.

CdTe electrochemical deposition was performed in electrochemical bath containing 1mM $CdSO_4$ and 0.3 mM TeO_2 following a reported procedure.[23.24] The pH of the electrolytic bath was adjusted to 1.8 using 0.1 M H_2SO_4 while the temperature was maintained at 65 ºC. Deposition was carried out using IvumStat electrochemical interface instrument under constant potential (chronoamperometric or potential sweep) conditions. Following electrodeposition the substrate was washed with distilled water thoroughly in order to remove the excess reactants from the substrate.

3. CHARACTERIZATIONS

The as-synthesized CdTe nanorod arrays were characterized further for elemental composition using PANalytical’s X'Pert PRO Materials Research Diffractometer (MRD, CuKα 1.5418Ǻ) for powder X-ray diffraction (pxrd). The pxrd was collected at grazing angles in thin film geometry (GI mode with Göbel mirrors). Scanning electron microscopy (SEM) imaging was performed using Hitachi S-4700 and Helios Nanolab-600 equipped with Energy Dispersive Spectrometry (EDS) detector (Oxford Instrument). Photoconductivity was measured through photoelectrochemical measurements performed with an IvumStat potentiostat.

4. RESULTS & DISCUSSION

The novelty in the current technique lies in the fact that, the PMMA which is used as *e-beam* resist, acts as an insulator thereby restricting the electrochemical deposition solely on the nanoelectrodes. This method is somewhat analogous to the growth of CdSe pillars, walls and other nano-structures reported previously where the deposition was done under a potential sweep.[16] However in the present case, under potential sweep (0 to –1 V *wrt* Ag/AgCl reference electrode) CdTe showed a cluster by cluster growth, giving rise to overdeposition and cauliflower like morphology with an average grain size of 500 nm (Figure 10.1 in supplementary information). This kind of clustered morphology might be detrimental for use in photovoltaic devices, since the presence of large number of grain boundaries adversely affect the transport of the charge carriers. Also, as the deposition voltage for CdTe changes, the stoichiometry of the deposited film changes as reported earlier,[24] thus leading to non-uniform and variable composition of the photovoltaic layer. Hence, it was necessary that we modify our strategy to address these issues, specifically to achieve continuous columnar growth and uniform nanorod composition.

5. CHARACTERIZATION OF MORPHOLOGY AND COMPOSITION OF THE NANOROD ARRAYS

Two modifications were adopted to improve the morphology of the electrodeposited CdTe. Firstly, the patterns were designed such that the nanoelectrode diameter was less than 500 nm (which was determined to be the critical grain size for continuous deposition above which it started forming clusters). Second, more crucial modification was that instead of a potential sweep, a constant potential chronoamperometric deposition was performed. In chronoamperometry, the CdTe was deposited at one particular potential (-0.55 V *wrt* Ag/AgCl) for varying amounts of time (15 – 45 sec). As expected, under these conditions, the deposited CdTe grew as columnar nanorods on the nanoelectrodes since lateral growth was restricted by the PMMA forming the walls of the nanochannel surrounding the nanoelectrode. Figure 7.2.1a shows the FESEM image of top view of the patterned substrate with the CdTe nanorods grown on 400 nm nanoelectrodes. It clearly depicts the flawless deposition of CdTe only over

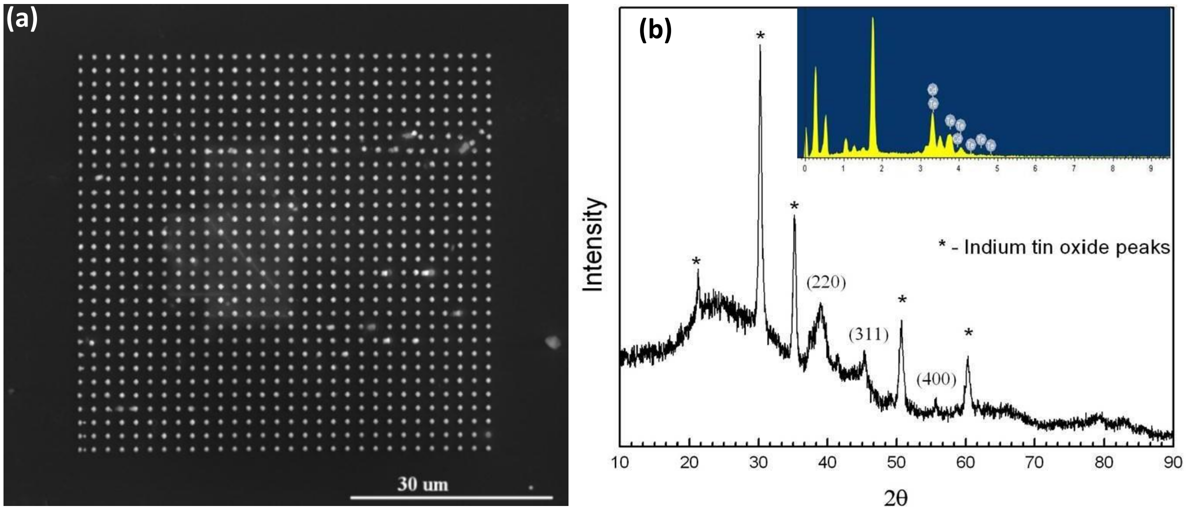

Figure 5.1 (a) SEM image of the CdTe nanorod arrays grown on 75 x 75 μm^2 area over ITO coated glass by confined electrodeposition. (b) Pxrd pattern of the as-grown nanorods showing the presence of CdTe. Inset in (b) shows the EDS analysis of the nanorods.

the nanoelectrodes defined through lithography. The rest of the PMMA surface looks absolutely clean, thereby, underlining the novelty of this approach. The formation of CdTe on the substrates was confirmed by pxrd (Figure 7.2.1b), which showed that the as-grown CdTe nanorods crystallized in the cubic zinc blende phase (JCPDS file, card number 00-015-0770). It was observed that the pxrd pattern showed weak intensities and low signal to noise ratio of the CdTe diffraction peaks. This could be attributed to the fact that the CdTe nanorods covered a region of only 75 x 75 μm^2 area on the substrate from where the pxrd pattern was collected. The high crystallinity of the ITO background also created obstructive scattering noise from the substrate. Considerable broadening of the (220) line of CdTe was observed in the pxrd pattern indicating the presence of nanodomains of ~50 nm diameter as calculated from the Scherrer equation.[26] The crystallinity of the nanorods could be increased by annealing the substrate-nanorod assembly at 200 °C under N_2. This is of significance since increased crystallinity of the nanorods indicates increase in the size of the crystalline domains inside the nanorod, thereby reducing the effects of grain boundaries, if any. The composition of the nanorods were also confirmed by EDS as shown in the inset of Figure 7.2b, which shows the presence of Cd and Te in the nanorods in approximately 1:1 ratio with slight excess of Te which indicates that the CdTe nanorods might be p-type.[24] Figure 7.2a shows SEM image, of the CdTe nanorods on the substrate at a 45˚ tilt angle demonstrating the deposition of CdTe nanorods as continuous columns which comes out of the PMMA surface. There is very minimal lateral growth of the deposited CdTe under choronoamperometric conditions. The length of the segment growing above the PMMA surface was approximately 500 nm. Inset in Figure 7.2a shows the elemental mapping of

Cd and Te across the nanorods, showing presence of Cd and Te exclusively in the nanorod. The removal of the PMMA matrix might be desirable for some applications of these nanorods, Hence, PMMA removal was attempted by soaking the substrate in acetone for 2 minutes. Figure 7.2b shows the SEM image of the CdTe nanorod arrays after partial removal of the polymer. The deposited CdTe nanorod arrays remained chemically attached on the substrate even after polymer removal, depicting the robustness of these nanorods and the firm attachment of the nanorods to the substrate. The polymer could also be removed by annealing the substrate-nanorods assembly at 200°C for 2.5 hrs under N_2, which preserved the morphology (Figure 10.2 in supplementary information). The nanorods grown by the choroamperometric deposition exhibited exact same stoichiometry and uniform aspect ratio across the entire pattern. This is of huge

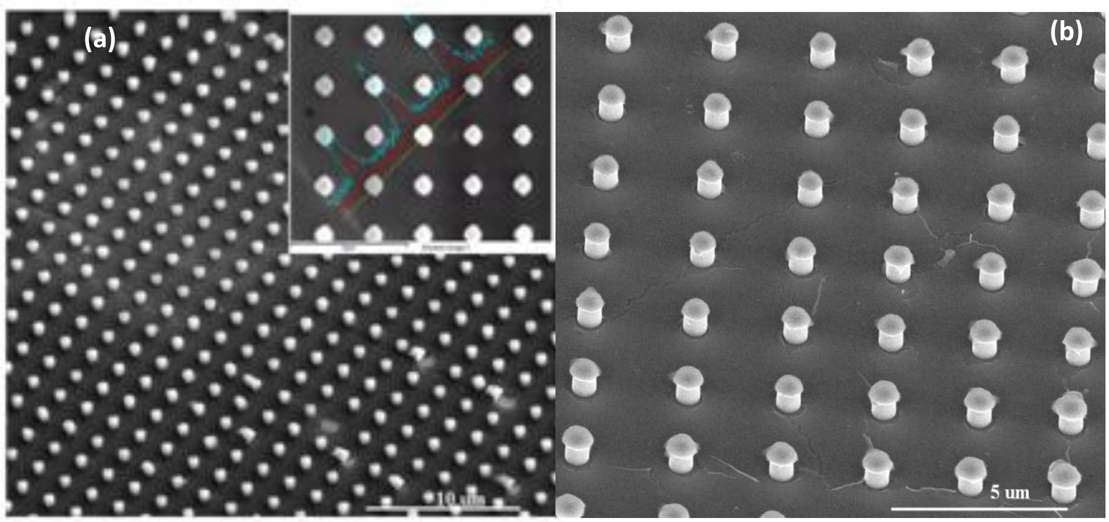

Figure 5.2 (a) SEM image of the vertically aligned CdTe nanorods tilted at 45˚ demonstrating the continuous columnar growth of CdTe. Inset shows an elemental line scan across the nanorods showing presence of Cd (red) and Te (blue) exclusively in the nanorods. (b) The CdTe nanorod arrays after partial removal of the PMMA matrix.

technological importance since, the properties of the nanomaterials are very much size-dependent and the effectiveness of the nanodevice rests on the monodispersity of the functional nano-structures in terms of size and morphology. It is very difficult to grow nanorods of exact same diameter and length by non-directed growth strategies. This simple approach outlined here was able to produce nanorods with uniform aspect ratio over 75 x 75 μm^2 area as shown in the SEM images. These individual patterns could be written one after another through stepwise *e*-beam lithography where the sample stage was moved by a fixed distance (the separation distance between two neighboring patterns), thereby creating the uniform nanorod arrays over a much larger area, typically of the order of mm^2. Hence the method outlined here can actually deliver nanorod arrays for practical usage.

6. **CONTROLLING THE ASPECT RATIO OF THE CDTE NANORODS**

While, a simple tuning of the nanoelectrode dimension was able to control the nanorod diameter very precisely, the length of the nanorods could be controlled very easily by varying the deposition time and PMMA thickness. By varying the thickness of the polymer and increasing the deposition time, we could successfully grow CdTe nanowires as long as 1 µm (Figure 7.1). However, the increased deposition time also led to mushroom-like tip of these nanowires due to the lateral growth. The aspect ratio of the CdTe nanowires was very uniform across the entire area of growth. This is of extreme significance since monodispersity in an ensemble of the nanowires is one of the most critical criterions for their applicability in practical devices. Also the packing density of these functional nanowires could be varied by changing the density of the nanoelectrodes in the lithography pattern. This is of considerable technological importance since it provides a platform for studying the effect of the diameter and especially density of these nanowires on the properties and signal strength of the device.

7. PHOTOELECTROCHEMICAL RESPONSE

Photoelectrochemical (PEC) measurements were done on the as synthesized CdTe nanorods arrays on ITO substrate. Two different electrolytes were used along with Ag/AgCl as reference electrode, Pt mesh as counter electrode and substrates as working electrodes. Acetate buffer was prepared using 0.1M acetic acid, 0.1 M sodium acetate and 0.1 M sodium sulfite.[27] The electrolyte having pH 4.6 was used for the photo electrochemical measurement. A 400W Xe lamp operating in UVA range (320-390 nm) with intensity of 100 mW/cm^2 (about 50% of the lamp intensity) was used to illuminate the nanorod device. Photoelectrochemical measurements in illuminated and dark conditions were performed for CdTe thin film on ITO and CdTe nanorod arrays on ITO. A PMMA coated ITO substrate (referred to as blank) was also characterized through PEC measurements to demonstrate that PMMA itself does not show appreciable photocurrent

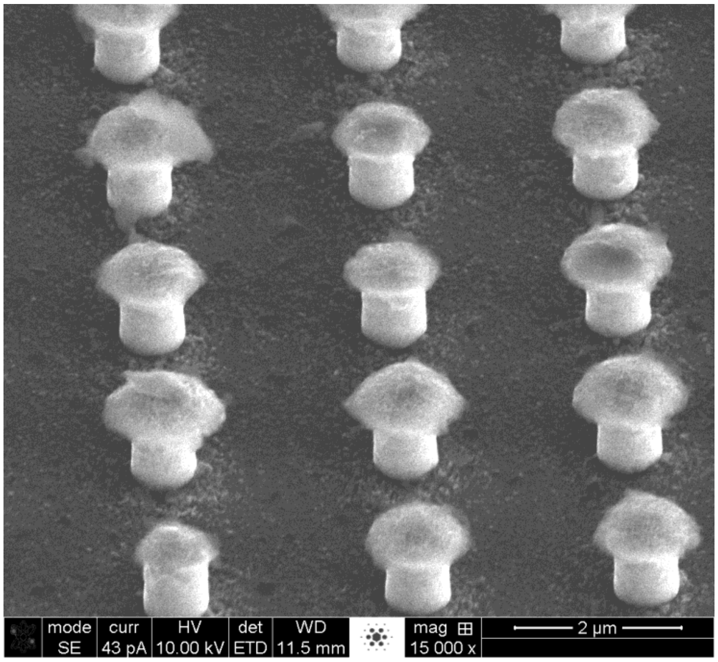

Figure 7.1 SEM image of high aspect ratio CdTe nanowires arrays synthesized using thicker PMMA coating leading to CdTe nanowires with length exceeding 1 µm.

under these conditions. The linear sweep technique was applied from 0V to 0.45V potential, at the scan rate of 0.01 V/s. For the *on-off* photocurrent measurement a polysulfide electrolyte was used. The polysulfide electrolyte was prepared by mixing equimolar quantities (0.1 M) of sodium sulfide and sulphur.[28,29] The pH was adjusted to 11 using 1 M NaOH. The *on-off* experiments were carried out by intermittent switching off of the light source for 10 sec intervals. As reported previously, the polysulfide solution is corrosive for CdTe.[30,31] But in our studies we observed that the PMMA layer actually protects the embedded CdTe nanowire arrays from chemical etching in solution.

The photoresponse from the nanorod arrays was compared with that obtained from a PMMA coated ITO-glass (blank) and bulk CdTe film electrodeposited on ITO-glass. Figure 7.2a shows the current response obtained from the nanorod arrays under dark and illuminated conditions, compared with that obtained from the blank substrate and CdTe bulk film under illumination. Clearly the PMMA blank does not show any appreciable photocurrent while the current response obtained from the CdTe nanorod device was in the mA range. Figure 7.2b demonstrates the modulation response of the photocurrent obtained from the CdTe nanorods as the light source was switched on and off intermittently.

The current density obtained from the CdTe nanorod device (0.0017 A/cm^2) was comparable to that obtained from the CdTe film (0.0015 A/cm^2) if only electrode area in considered. However, the coverage of the electrode with the active material (CdTe) was much smaller in the nanorod device. The inset in Figure 7.2b shows a graphical representation of the comparison between the electrodes containing the CdTe film and the nanorod arrays used for photocurrent measurement. In both cases the ITO-coated glass (i.e. the electrode) was dipped almost halfway into the electrolyte solution to measure the photocurrent and the electrode area is represented by the black boxes in the figure. But, while the CdTe film was grown over an electrode area of approximately 1 x 0.5 cm^2, the CdTe nanorod arrays were covering an area of 100 x 100 μm^2 (shown by the red boxes in the corresponding figure). Hence, the actual area of coverage for the CdTe nanorods would be approximately one-hundredth of the CdTe film, indicating that the actual current density will be much higher for the nanorod device. This indicates that the CdTe nanorod arrays can generate a photocurrent density as high as CdTe thin film but with

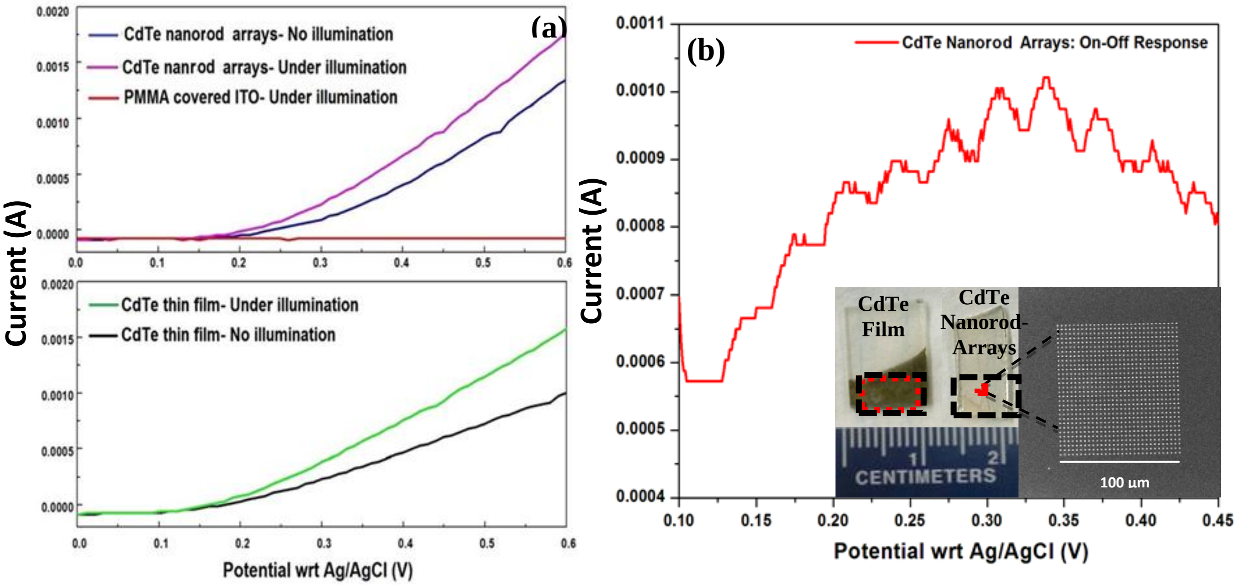

Figure 7.2 (a) The photocurrent obtained from the CdTe nanorod arrays under illumination and dark conditions compared with that obtained from electrodeposited CdTe film. (b) The "on-off" response obtained when the light source was switched on and off at regular intervals while the photocurrent was being recorded. Inset shows the comparison between the actual coverage of the electrode area with the CdTe thin film (left panel) and the CdTe nanorods (right panel). The black boxes show the electrode area under PEC measurement while the red boxes represent the actual coverage with the active material (CdTe).

less than 10% surface coverage as compared to the film. This observation is very similar to the InP nanowire arrays reported recently by Wallentin et al. [7]. Previous researchers have reported photocurrent obtained from individual CdTe nanowires contacted by two Au electrodes.[33,34] These photocurrents were mostly in the pA to nA range[32,33] as would be expected from these extremely thin, extremely small current carriers. However, the aligned nanorod arrays grown by this confined electrodeposition contains huge density of nanorods in parallel orientation acting like a parallel series of resistors. Since the current from a parallel series of resistors is summation of the individual currents, there is huge amplification of the photocurrent in this nanorod arrays leading to high signal-to-noise ratio.

8. CONCLUSIONS

We have successfully developed a protocol of growing patterned CdTe nanorod arrays on conducting surfaces by simple electrochemical methods coupled with lithographic patterning. The photocurrent obtained from the vertically aligned CdTe nanorod arrays grown by this method was comparable to that obtained from a CdTe film electrodeposited over a much larger area thereby underlining the potential of this technique for producing high efficiency miniaturized devices.

This method will be especially useful for making solar cell devices since, the efficiency of the solar cells nowadays, relies heavily on the materials chosen to absorb the solar radiation and also on the design of the cells. Recently there have been several papers describing the "*nanopillar*" solar cells, where CdS light absorbers are grown as nanorods embedded in a CdTe matrix.[34,35] The more effective separation of the charge carriers and better charge injection is believed to increase the efficiency of the solar cells in this geometry. We have in fact employed the method described in this communication in an attempt to grow CdTe nanorods in a surrounding matrix of CdS, where the CdS was deposited by chemical bath deposition prior of lithography and CdTe electrodeposition steps. By simple variations of the electrodeposition strategy, it was possible to obtain both radial and lateral *p-n* junctions in these CdS-CdTe assemblies. Preliminary results from these studies indicate that "*nanopillar*" solar cell like geometry was indeed achievable though this simplistic approach (Figure 10.3 and 10.4 in supplementary information) and the device showed significant photocurrent upon UV excitation.[36] The primary requirement for this technique is the embedded nanoelectrodes, which can be obtained by lithography on any conducting surface, including flexible substrates. In principle, any functional material can be grown by electrodeposition in the confined nanoelectrodes. This would be significantly helpful for growing nanowire arrays of the ternary and quaternary chalcogenides like the CIGS, CIS where morphology control is extremely challenging, given the complexity of the systems. The versatility of this approach is currently being tested with other photovoltaic and semiconductor systems. Authors are also trying to measure the spectral response profile for photocurrent generation of the CdTe nanorod arrays.

Supporting Information Available: SEM images for cluster growth of CdTe, annealed CdTe nanorods and CdS-CdTe heterojunction devices; elemental analysis of CdS-CdTe devices. This material is available free of charge via the Internet at http://www.sciencedirect.com.

Acknowledgements

The authors would like to acknowledge Materials Research Center (MRC) for equipment usage characterization and Dr. Kai Song for help with the lithography. This work was funded through Missouri S&T start-up funds.

9. REFERENCES

[1] N. S. Lewis, D. G. Nocera, Proc. Natl. Acad. Sci. U.S.A. 103 (2006), 15729-35.

[2] R. W. Birkmire, E. Eser, Annu. Rev. Mater. Sci. 27 (1997), 625-653.

[3] X. Wu, Solar Energy 77 (2004), 803-814. K. W. Frese, Appl. Phys. Lett. 40 (1985), 275-277.

[4] A. I. Hochbaum, R. Chen, R. D. Delgado, W. Liang, E. C. Garnett, M. Najarian, A. Majumdar, P. Yang, Nature 451 (2008), 163-168.

[5] I. Gur, N. A. Fromer, M. L. Geier, A. P. Alivisatos, Science 310 (2005), 462.

[6] B. Kannan, K. Castelino, A. Majumdar, Nano Lett. 3 (2003), 1729-32.

[7] J. Wallentin, N. Anttu, D. Asoli, M. Huffman, I. Aberg, M. H. Magnusson, G. Siefer, P. Fuss-Kailuweit, F. Dimroth, B. Witzigmann, H. Q. Xu, L. Samuelson, K. Deppert, M. T. Borgstrom, Science 339 (2013), 1057-1060.

[8] E. Garnett, P. Yang, Nano Lett. 10 (2010), 1082-1087.

[9] M. A. Green, J. Mater. Sci.: Mater. Electron. 18 (2007), S15-S19.

[10] A. Miguel, M. Contreras, A. B. Egaas, K. Ramanathan, J. Hiltner, A. Swartzlander, F. Hasoon, R. Noufi, Prog. Photovol.t Res. Appl. 7 (1999), 311-316.

[11] A. Shah, P. Torres, R. Tscharner, N. Wyrsch, H. Keppner, Science, 285 (1999), 692-69818.

[12] J. Britta, C. Ferekides, App. Phys. Lett. 62 (1993), 1851-1852.

[13] M. Burgelman, J. Poortmans, V. Arkhipov (Eds.), Thin Film Solar Cells-Fabrication, Characterizations and Applications , John Wiley & Sons, Chicester, 2006, pp. 277–314.

[14] I. Gur, N. A. Fromer, M. L. Geier, A. P. Alivisatos, Science, 310 (2005), 462.

[15] Y. W. Su, C. S. Wu, C. C. Chen, C. D. Chen, Adv. Mater. 15 (2003), 49-51.

[16] B. R.Martin, D. J. Dermody, B. D. Reiss, M. Fang, L. A. Lyon, M. J. Natan, T. Mallouk, E. Adv. Mater. 11 (1999), 1021.

[17] J-G. Wang, M-L.Tian, T. E. Mallouk, M. H. W. Chan, Nano Lett. 4 (2004), 1313.

[18] J. D. Klein, R. D. Herrick, D. Palmer, M. J. Sailor, C. J. Brumlik, C. R. Martin, Chem. Mater. 5 (1993), 902-904.

[19] D. Zubía, C. López, M. Rodríguez, A. Escobedo, S. Oyer, L. Romo, S. Rogers, S. Quiñónez, J. J. McClure, Electron. Mater. 36 (2007), 1599-1603.

[20] M. I. B. Utama, Z. Peng, R. Chen, B. Peng, X. Xu, Y. Dong, L. M. Wong, H. S. Wang, Q. Xiong, Nano Lett,. 11 (2011), 3051-3052.

[21] Y. Xia, G. M. Whitesides, Angew. Chem. Int. Ed. 37 (1998), 550 -557.

[22] B. D. Gates, Q. Xu, M. Stewart, D. Ryan, C. G. Wilson, G. M. Whitesides, Chem. Rev. 105 (2005), 1171–1196.

[23] C. Ferekides, J. Britt, Sol. Energ. Mat. Sol. C. 35 (1994), 255–262. T. L. Chu, S. S. Chu, Prog. Photovolt. Res. Appl. 1 (1993), 31–42.

[24] M. P. R. Panicker, M. Knaster, F. A. Kroger, J. Electrochem. Soc. 125 (1978), 566-572.

[25] R. N Bhattacharya, K. J. Rajeshwar, Electrochem. Soc; 131 (1984), 2032-2034.
[26] A. L. Patterson, Phys. Rev. 56 (1939), 978-982.

[27] M. Miyake, K. Murase, T. Hirajo, Y. J. Awakura, Electrochem. Soc. 150 (2003), C413-C419.

[28] S. Mishra, S. Tiwari, J. Phys. D. Appl. Phys. 27 (1994), 2009-2012.

[29] P. M. Lessner, F. R. McLarnon, J. Winnick, E. J. Cairns, J. Electrochem. Soc. 140 (1993), 1847-1749.

[30] L. P. Bicelli, J. Phys. Chem. 96 (1992), 9995–10001.

[31] G. Hodes, Nature, 285 (1980), 29–30.

[32] Z. Hackney, L. K. Skinner, S. Washburn, Mater. Lett. 64 (2010), 2016–2018.

[33] M. C. Kum, B. Y. Yoo, Y. W. Rheem, K. N. Bozhilov, W. Chen, A. Mulchandani, N. V. Myung, Nanotechnology, 19 (2008), 325711-325718.

[34] Z. Fan *et.al.* Nat. Mater. 8 (2009), 648-653.

[35] R. Kapadia, Z. Fan, K. Takei, A. Javey, Nano Energy, 1 (2012), 132-144.

[36] S. Mishra, M. Nath, unpublished results.

10. SUPPLEMENTARY INFORMATION

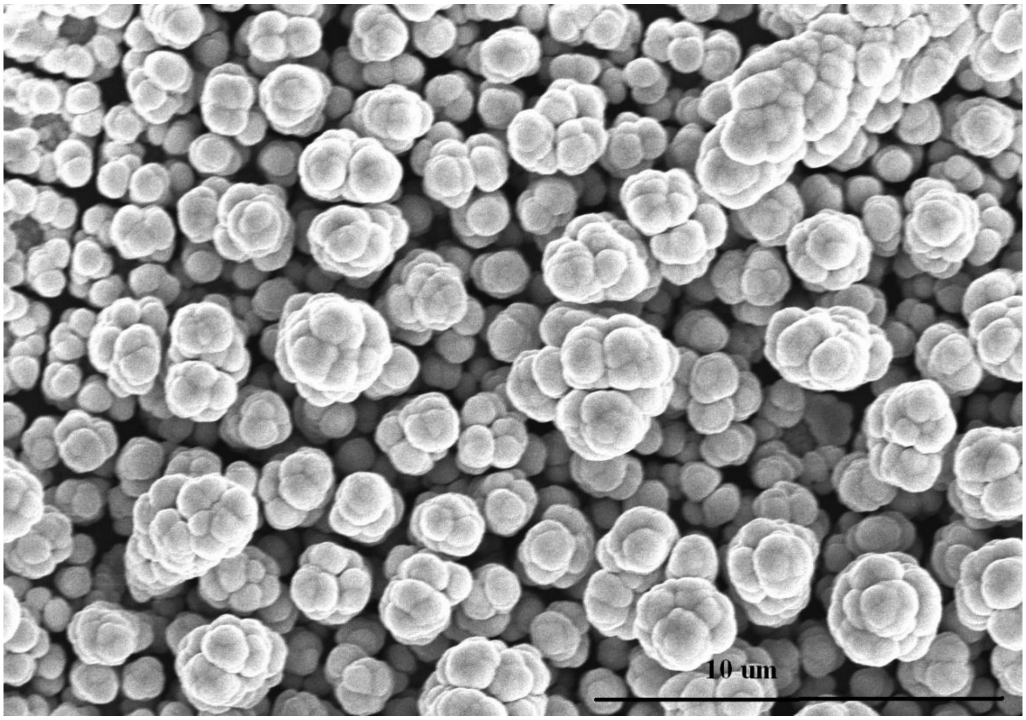

Figure 10.1 Cauliflower like cluster growth of the CdTe over nanoelectrodes with hole sizes of 1 um when subjected to cyclic voltametry technique for the electrochemical deposition. Grain size obtained was typically @ 500 nm.

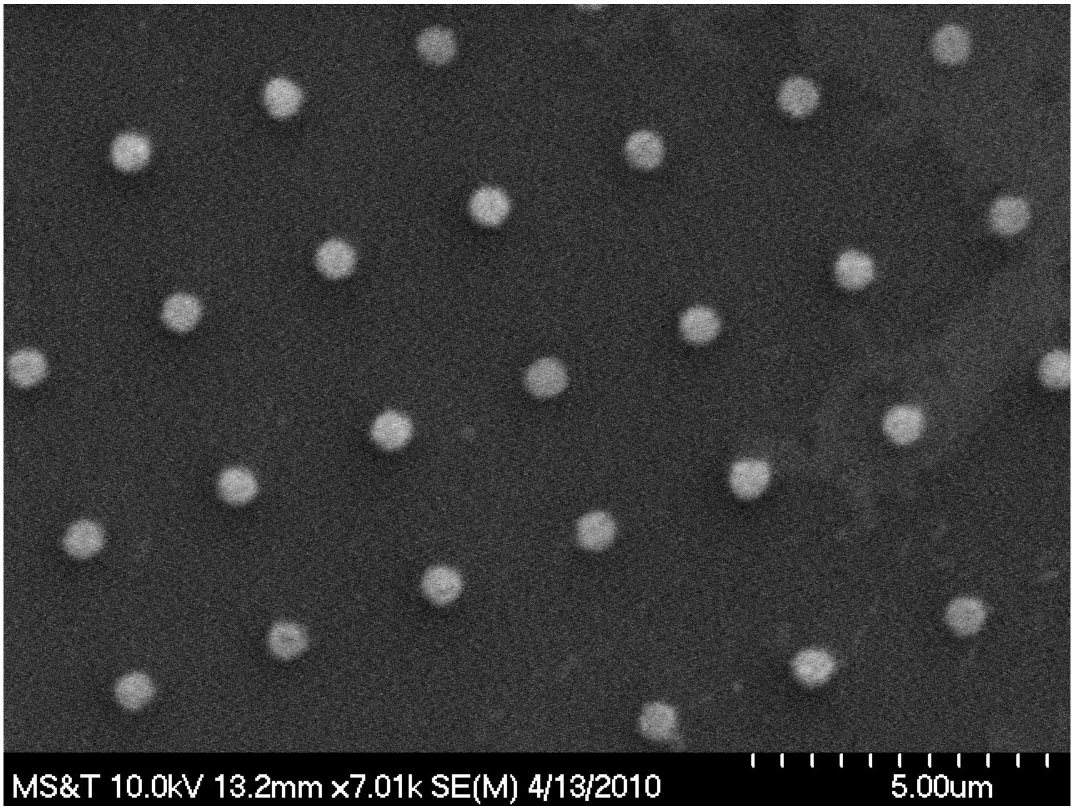

Figure 10.2 CdTe nanorods arrays on the substrate after the substrate was annealed for 30 minutes at 250°C under a flow of N_2.

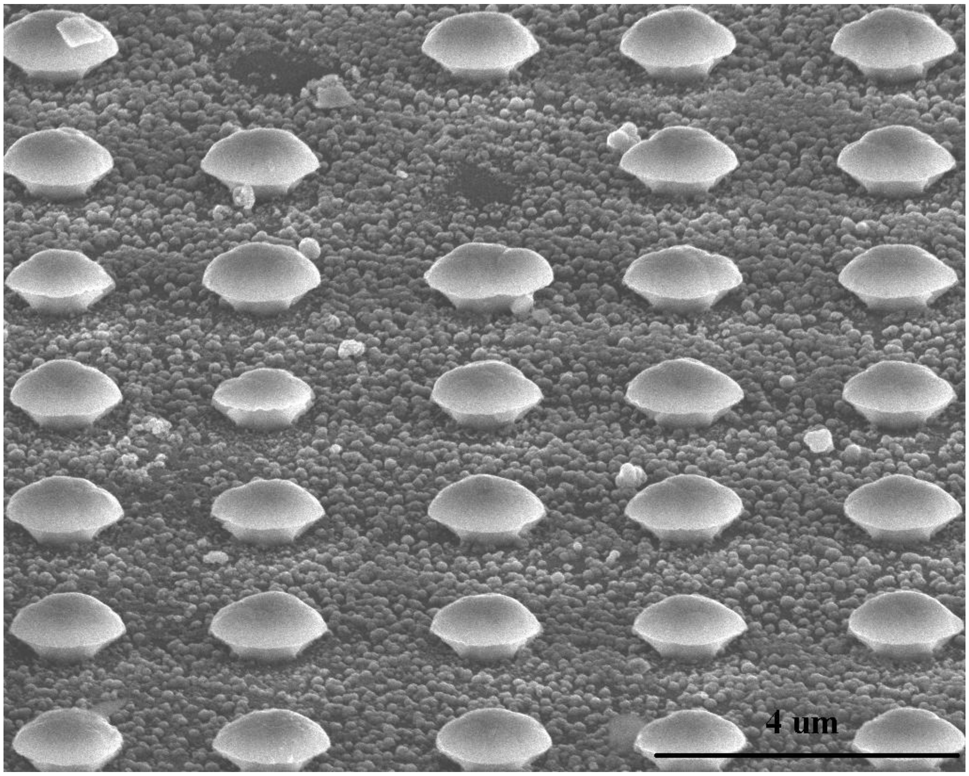

Figure 10.3 SEM image of CdTe nanorods arrays on top of 1 um thick layer of nanocrystalline CdS.

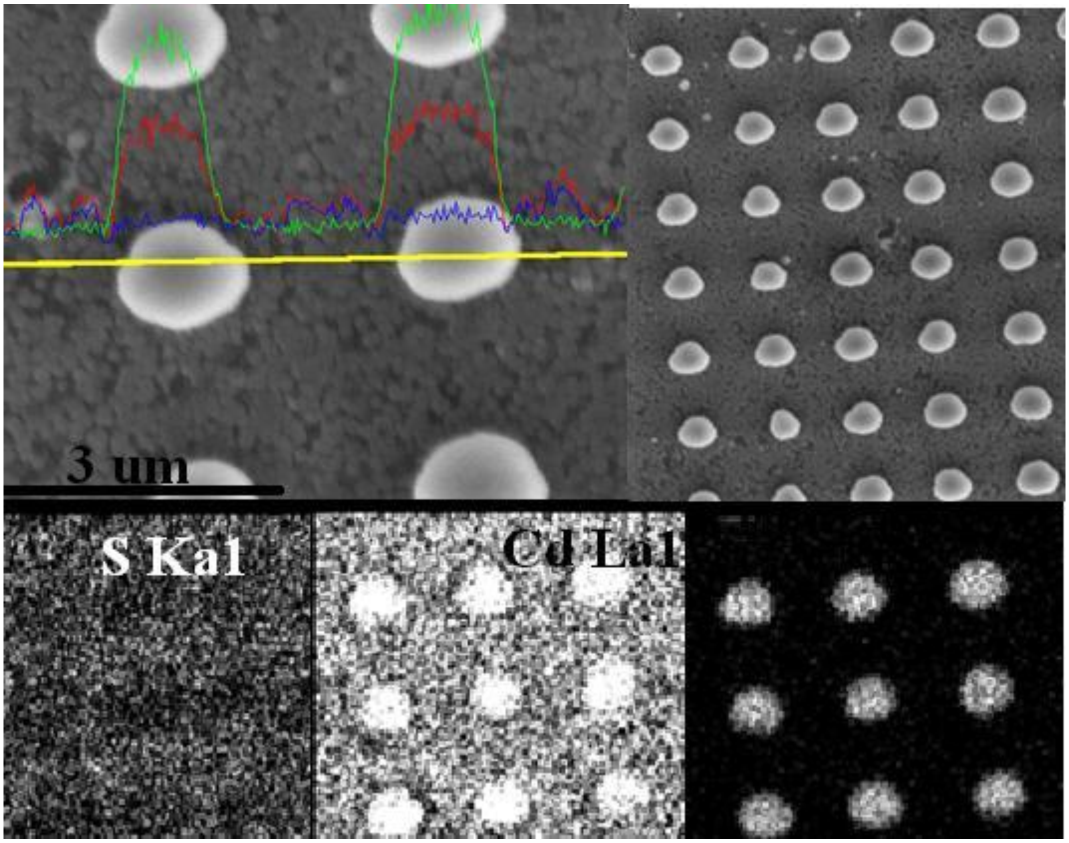

Figure 10.4 The line scan across yellow line indicates the elements (Cd-Red line, S- Blue line, Te Green line) confirming the presence of CdTe nanorods on CdS layer.

IV: FABRICATION OF RADIAL AND LATERAL, CdTe—CdS NANOROD ARRAYS ON CONDUCTING SUBSTRATE

Manuscript in Preparation for Journal of Materials Science & Engineering B

Sukhada Mishra, Manashi Nath*

We have established a protocol for the fabrication of CdTe—CdS, *p—n* junction nanorod arrays, aligned in lateral and radial dimensions, covering an area of 75 µm×75 µm on conducting substrate. The five step protocol involves chemical bath deposition, electron beam lithography and electrochemical deposition methods to achieve homogenous arrays of nanorods of CdTe—CdS. In the first step, the CdS was deposited on the conducting ITO coated glass, in the second step nanoelectrodes were defined on polymethyl methacrylate (PMMA) resist coated on CdS layer using electron beam lithography, followed by electrochemical deposition of the CdTe in final step. The selective etching of the CdS during the procedure, is the key factor defining the lateral or radial nature of the formed CdS—CdTe heterojunction. Photoelectrochemical analysis has been performed to characterize the photoconductivity response of nanorod arrays. The lateral and radial p—n junction CdS—CdTe nanorod arrays showed the current in the mA range, which was comparable to the CdS—CdTe thin film counterpart.

1. INTRODUCTION

Over the last 50 years, commercial silicon photovoltaic have been developed to convert sunlight into electricity at efficiencies around 20% and provide the most feasible carbon-neutral route to displacing terawatts (TW) of nonrenewable power consumed worldwide.[15] However, large scale implementation of Si based solar cells is still not economically the best solution since, the manufacturing and implementation process is of high cost compared to the traditional power sources. Some of the binary chalcogenides like CdTe, CdSe, CdS, CuS, CuSe have shown promise for efficient power generation.[16,20] Recently, the combination of CdS-CdTe has shown promise as photovoltaic materials, as n-type CdS acts as a window layer which maximizes the solar absorption. In 1972, Bonnet and Rabenhorst demonstrated the analysis of CdS-CdTe thin films as solar cells, and reported an efficiency of 6%.[4] In 1982, an efficiency of 10% was reported by Tyan and Perez-Albuerne.[5] An exceptional efficiency of 15.8% was achieved by Ferekides *et. al.* in 1993,[6] and the efficiency of 16.5% was achieved by Wu *et. al.*[7] Owing to the presence of CdS layer on the substrate, reduction in the surface recombination is achieved which led to the increased efficiency.[8] CdS-CdTe composition holds great potentials to achieve economically solar cells.

The growth nanorod arrays of CdTe in the CdS matrix has been demonstrated to provide a three dimensional morphology enabling high optical absorption, thereby, increasing the carrier collection efficiency.[9] High-aspect-ratio nanorods allow the use of a sufficient thickness of material to obtain good optical absorption while simultaneously providing short collection lengths for excited carriers in a direction normal to the light absorption,[10] thereby, increasing the effectiveness of the photovoltaic device. Ordered arrays of silicon nanowires increase the path length of incident solar radiation by up to a factor of 73.[11] It has been demonstrated that the efficiency of the solar cell can be further increased by constructing a radial *p*-*n* junction for Si nanowire solar cells.[10] In this communication, we have demonstrated the fabrication of CdTe-CdS, radial and lateral p-n junction nanorod arrays using electron beam lithography, chemical bath deposition and electrochemical deposition methods.

2. EXPERIMENTAL METHOD

In order to fabricate the CdTe—CdS, lateral and radial nanorod arrays patterns would be defined on transparent ITO coated glass substrate in a 5 step process, using lithographic techniques. 2.1 demonstrates the schematic representation of the 5 step processes carried out for the fabrication of p—n heterojunction. Step one consists of the chemical bath deposition (CBD) of CdS on conducting ITO coated glass. CBD is a simple, yet versatile technique which has been used extensively to grow semiconductor films on various substrates.[12] It is a low temperature method which involves dipping the substrate in a solution containing the precursor salts. The concentration of the solution, temperature and dipping time determines the thickness and morphology of the film. Well controlled CBD leads to formation of a very uniform layer of the semiconductor on the surface and the attachment of the film to the surface is very robust. In order to grow 1 µm thick layer of CdS chemical bath deposition was carried out. In the second process, 0.5 µm thick PMMA resist was spin coated covering the CdS layer. This process is followed by the third process of electron beam lithography. Upon post development process using MIBK:IPA (1:3) solvent, the PMMA from patterned regions got dissolved and underlying CdS layer got exposed. The fourth step is the critical step, which defined the lateral or radial dimension of the fabricated p—n junction. The CdS layer was selectively removed using HCl etching for 15 seconds, which led to the exposure of the underlying ITO. Some substrates were retained, without performing the CdS etching. In

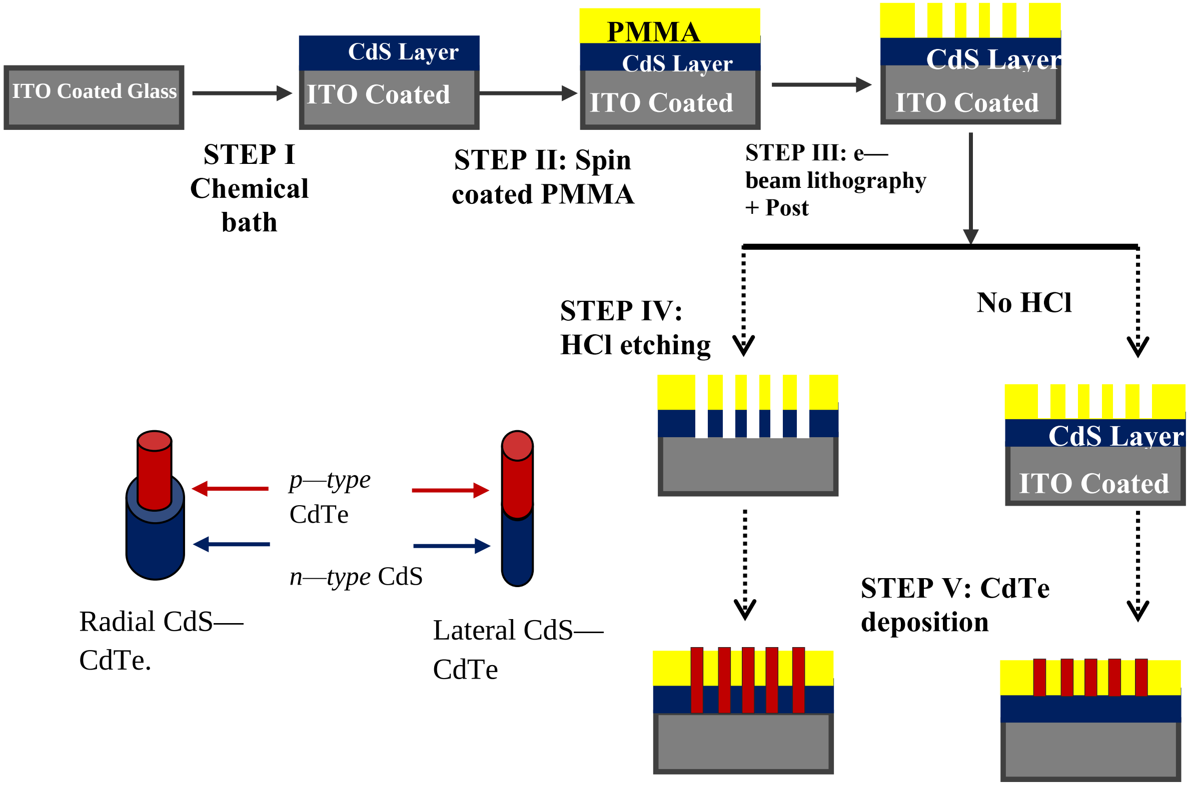

Figure 2.1. Schematic showing the fabrication of lateral and radial CdS-CdTe nanorod arrays on conducting substrates through 5 step processes.

the final step, the p—type CdTe was deposited using electrochemical deposition technique as described in earlier reports. When the CdTe was deposited on the patterns coating etched CdS, the CdTe deposited on the exposed ITO which fabricate the CdTe nanorod arrays CdS, the CdTe nanorod arrays were fabricated on top of the CdS layer, thus forming a lateral p—n heterojunction. These fabricated CdS—CdTe nanorod arrays were further characterized for the elemental composition and morphology analysis through powder X—ray diffraction (pxrd), energy dispersive spectroscopy (EDS), and scanning electron microscopy (SEM). The photoconducting characteristics of nanorod arrays were examined using photo—electrochemical conductivity measurements.

3. CHARACTERIZATION TECHNIQUES

Figure 3.1a shows the pxrd pattern collected from the region of patterned CdS—CdTe nanorod arrays. It demonstrated the presence of CdTe and CdS. It also showed the presence of ITO owing to the presence of high degree of background. The pxrd collected from the radial CdS—CdTe heterojunction nanorod arrays, also demonstrated the pxrd pattern matched with the standard patterns of CdS, CdTe, and ITO (Supplementary Figure S1). 3.1b shows the EDS collected from the patterned regions, confirming the presence of elemental Cd, S, and Te in the nanorod arrays. 3.1c shows the SEM image, demonstrating the 75 µm×75 µm area of the patterned region containing 900 nanorod arrays. It demonstrated the high degree of homogeneity of the diameter of nanorods across the area. 3.1a demonstrates the SEM image of the top view of the radial CdS—CdTe nanorod arrays. It shows the uniform diameters of about 400 nm of the CdTe nanorods, embedded in the thin film of Cds. 3.1b shows the tilted SEM image of the nanorod arrays, which clearly shows that the CdTe nanorod arrays are surrounded by CdS matrix. In order to confirm the elemental composition from the precise regions of CdTe nanorods and surrounding CdS matrix, line mapping was carried out. As shown in 3.2c, a line passing across the nanorod assembly was drawn in EDS analysis mode, and Cd, Te and S elements were traced across the region. It individual elemental signals confirmed the presence of Cd and Te in the nanorod regions, while presence of Cd and S in the surrounding thin film region. Figure 3.3. shows the characterizations perfomed on the radial p-n junction CdS-CdTe nanorods arrays.

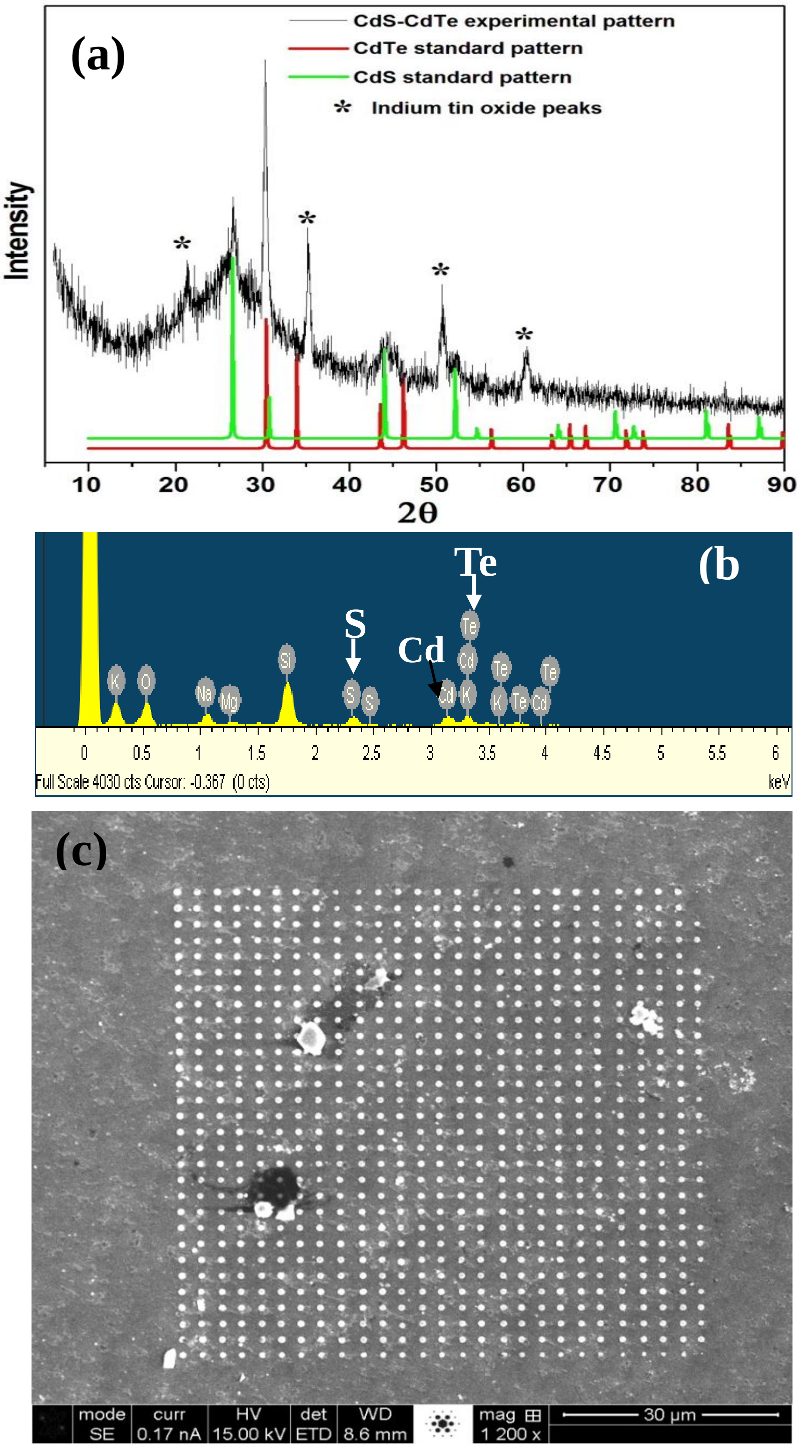

Figure 3.1 (a) XRD pattern collected from the patterned CdS-CdTe nanorod arrays, which matched with the standard patterns of CdS and CdTe. It also contained major peaks of ITO as a background effect. (b) EDS spectroscopy performed on the patterned area confirming the presence of Cd, S and Te elements. (c) SEM image of the as deposited pattern, demonstrates the CdTe nanorod arrays covering an area of 75 µm×75 µm area.

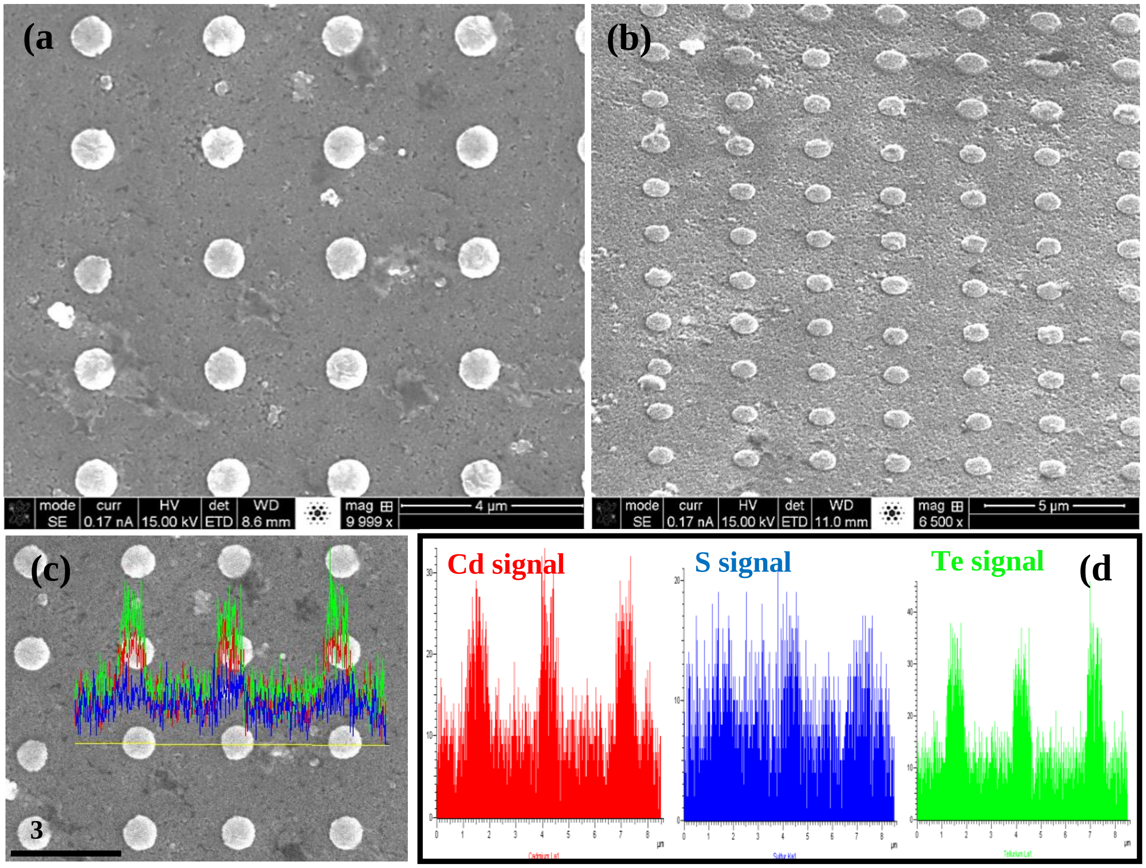

Figure 3.2 Schematic showing the fabrication of lateral CdS-CdTe nanorod arrays on conducting substrates through 5 step processes.

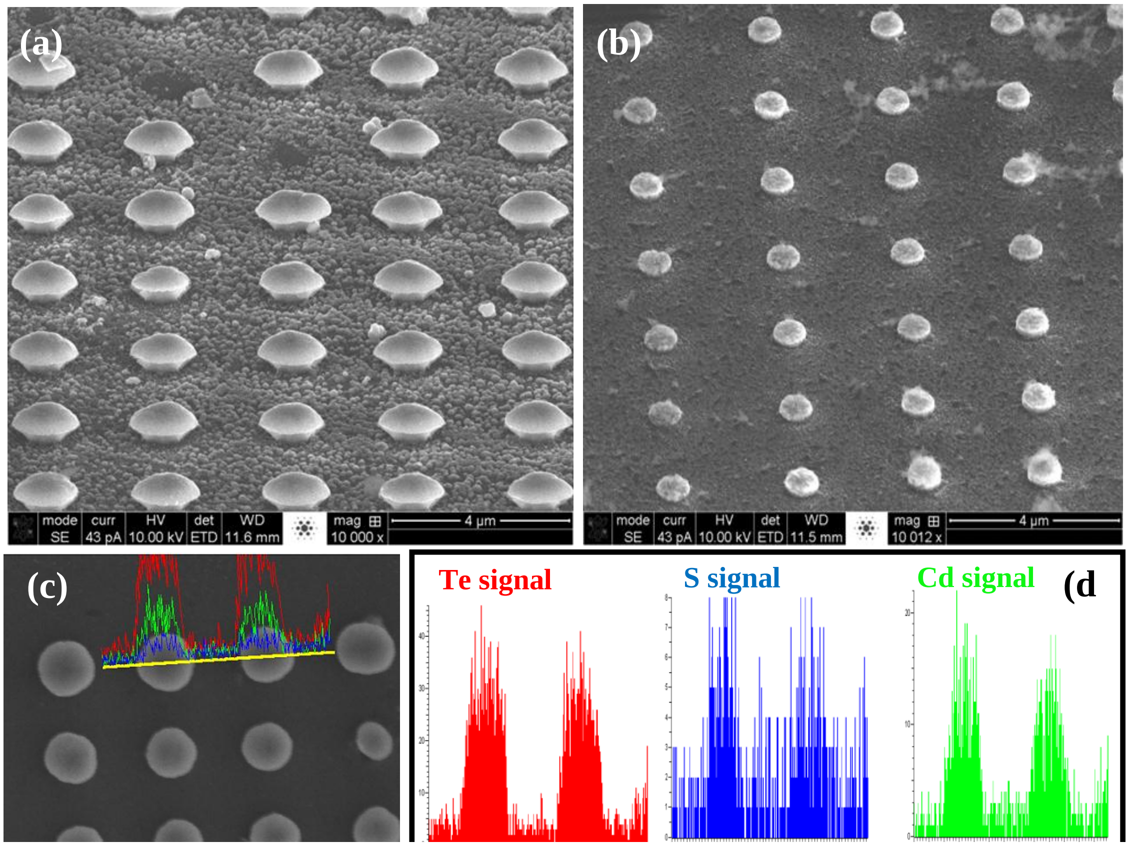

Figure 3.3 Schematic showing the fabrication of radial CdS-CdTe nanorod arrays on conducting substrates through 5 step processes.

4. PHOTOELECTROCHEMICAL ANALYSIS

Photoelectrochemical (PEC) measurements were done on the as synthesized CdS—CdTe nanorods arrays on ITO substrate. Acetate buffer electrolyte was used in three cell assembly containing Ag/AgCl as reference electrode, Pt mesh as counter electrode and substrates containing nanorod arrays as working electrodes. Acetate buffer was prepared using 0.1M acetic acid, 0.1 M sodium acetate and 0.1 M sodium sulfite.[13] The electrolyte having pH 4.6 was used for the photo electrochemical measurement. A 400W Xe lamp operating in UVA range (320—390 nm) with intensity of 100 mW/cm^2 (about 50% of the lamp intensity) was used to illuminate the nanorod device. Photoelectrochemical measurements in illuminated and dark conditions were performed for CdS—CdTe thin film on ITO and radial/ lateral p—n heterojunction nanorod arrays on ITO. The linear sweep technique was applied from 0V to 0.45V potential, at the scan rate of 0.01 V/s. It was observed that the CdS—CdTe nanorods were very stable in the electrolyte solution and did not undergo degradation during the experiments.

The on—off photoresponse from the nanorod arrays was compared with that obtained from a bulk CdS—CdTe film electrodeposited on ITO—glass. 4.1a shows the on—off current response obtained radial CdS—CdTe nanorod arrays under dark and illuminated conditions. 4.1b shows the on—off current response obtained from lateral p—n junction device. Interestingly, the photocurrent obtained from the CdS—CdTe nanorod devices (0.0001 A/cm^2) was comparable to that obtained from the CdS—CdTe film (0.001 A/cm^2). Additionally, if the electrode area is considered, then the coverage of the electrode with the active material (CdS—CdTe) was smaller in the nanorod device. On the other hand, the CdS— CdTe film was grown over an electrode

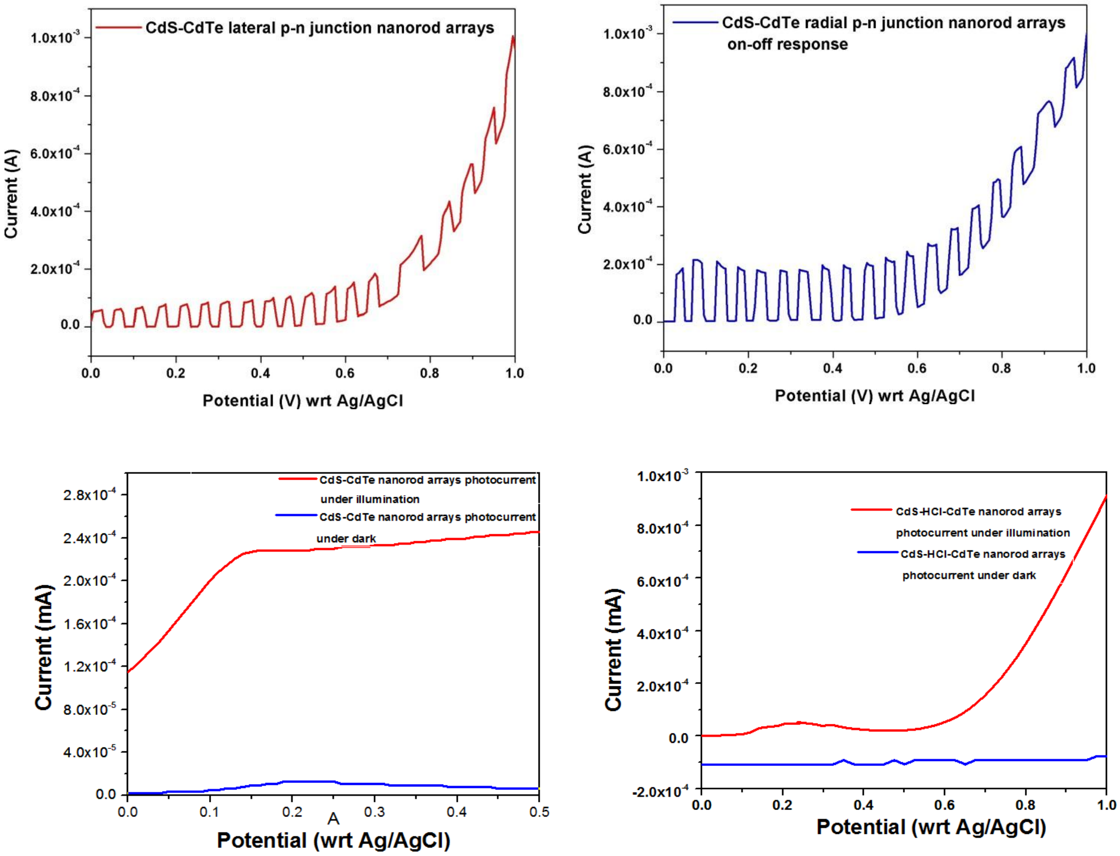

Figure 4.1 The on—off response of the photocurrent obtained from the CdS—CdTe lateral and radial p—n junction nanorod arrays under alternate illumination and dark conditions. (b) Photoconductivity response collected for CdS—CdTe radial p—n junction nanorod arrays under illumination and under dark condition.

area of approximately 1 x 1 cm^2, the CdS—CdTe nanorod arrays were covering an area of 75 x 75 μm^2 .Hence, the actual area of coverage for the CdS—CdTe nanorods would be approximately one—hundredth of the thin film which indicates that the nanorod device is more efficient than the thin film assembly. This observation is very similar to the in nanowire arrays reported recently by Wallenstein *et al.*[14]

5. CONCLUSION

In conclusion, we could successfully establish a simple yet versatile protocol for the fabrication of lateral and radial, CdS—CdTe heterojunction nanorod arrays on conducting ITO substrate. The SEM images demonstrated extremely homogenous morphology and diameter of the grown nanorod arrays. The CdS—CdTe nanorod arrays retained their morphology and chemical composition even after soaking in electrolyte solution during photoelectrochemical measurements, which indicates the robustness of the nanorod—substrate interface.. Interestingly, preliminary photoelectrochemical measurementa from this nanorod devices revealed that these nanorod arrays were capable of producing photocurrent density in the mA range, which was comparable to that obtained with CdS—CdTe thin film. This is of immense technological importance, since the photocurrent can be potentially amplified even further simply by increasing the packing density of the nanowires.

6. REFERENCES

1. Lewis, N. S.; Nocera, D. G. *Proc. Natl. Acad. Sci. U.S.A.* 2006, *103*, 15729-35.

2. Birkmire, R. W.; and Eser, E. *Annu. Rev. Mater. Sci.* 1997, *27*, 625-653. Wu, X. *Solar Energy*, 2004, *77*, 803-814. Frese, K. W. *Appl. Phys. Lett.* 1985, *40*, 275-277.

3. Chen, W. S.; Stewart, J. M.; and Mickelsen R. A. *Appl. Phys. Lett.* 1985, *46*, 1095-1098.

4. Bonnet,D.; Rabenhorst, H. *9th Photovoltaic Specialists Conf.* (1972) pp. 129.

5. Tyan, Y.; Perez-Albuerne, e. A. *Proc. 16th Photovoltaic Specialists' Conf., San Diego, CA,* IEEE, New York (1982), p. 794

6. Britt, J.; Ferekides, C. **1993** *Appl. Phys. Lett.*, *62*, 2851.

7. Wu, X. *Solar Energy,* **2004**, *77*, 803.

8. Yamaguchi, K.; Nakayama, N.; Matsumoto, H.; Ikegami, S. *Jpn. J. Appl. Phys.***1977**, *16*, 1203.

9. Fan, Z.; Razavi, H.; Do, J.W.; Moriwaki, A.; Ergen, O.; Chueh, Y. L.; Leu, P. W.; Ho, J. C.; Takahashi, T.; Reichertz, L.A.; Neale, S.; Yu, K.; Wu, M.; Ager, J. W.; Javey, A. Nat. Mat. **2009**, *8*, 648.

10. Kayes, B. M.; Atwater, H. A.; and Lewis, N. S. *J. Appl. Phys.* **2005**, *97*, 114302.

11. Garnett, E.; Yang, P. *Nano Lett.* **2010**, *10*, 1082-1087.

12. Gorer, S.; Hodes, G. *J. Phys. Chem.* ***1994***, *98, 5338–5346.*

13. M. Miyake, K. Murase, T. Hirajo, Y. J. Awakura, *Electrochem. Soc.* 150 (2003), C413—C419.

14. J. Wallentin, N. Anttu, D. Asoli, M. Huffman, I. Aberg, M. H. Magnusson, G. Siefer, P. Fuss—Kailuweit, F. Dimroth, B. Witzigmann, H. Q. Xu, L. Samuelson, K. Deppert, M. T. Borgstrom, Science 339 (2013), 1057—1060.

V. FABRICATION OF MULTIFUNCTIONAL, SOFT—FERROMAGNETIC, DUMBBELL SHAPED AU—CoSe NANOPARTICLES

(Submitted to Nanoscale)

Sukhada Mishra, Kai Song, and Manashi Nath

We have synthesized multifunctional dumbbell shaped Au—CoSe nanoparticles on Si substrate through catalyst aided chemical vapor deposition technique. The Au nanoparticles range 20—25 nm in size while the CoSe nanoparticles range 150—200 nm in size. The technique utilized volatile cobalt acetylacetonate and elemental selenium as precursors, and Au—Pd (3:2) nanoparticles acted as a catalyst.

1. INTRODUCTION

Development in the field of nanotechnology has contributed to the advancement of the practical applications of nanoparticles in nanomedicine.[1—4] The emergence of nano—bioengineering has led to the discovery and investigation of new class of nanomaterials, termed as "*multifunctional nanostructures*". The capability to tune the size, shape and morphology of the nanoparticles provide them the versatility and intensifies their performance in real life applications. Nanoparticles provide greater surface area thereby; the surface chemistry plays a crucial role. The nanoparticle surface could be manipulated by active functionalization.[1] The nanometer size of the particles is comparable to the dimensions of biological components such as antibodies, nucleic acids, protein and other biomolecules,[2] which makes the nanoparticle suitable to even introduce in the biological system as foreign bodies. Biocompatibility,[3] biomimicking[4] are one of the most important characteristics of the nanoparticles, and thus all these features collectively make the multifunctional nanoparticles a powerful tool for the potential biomedical applications.[5]

Multifunctional nanostructures, are explored extensively for the applications in biosciences such as molecular imaging,[6] magnetic separation,[7] fluorescent labeling.[8] Multifunctional nanoparticles can be categorized based on the morphology of the products and the primary functionalities of the components of the nanoparticles. Based on the morphology, core—shell geometry,[9] dumbbell shaped nanoparticles (DNP)[10] morphology could be achieved through designing the synthetic protocols. Based on the component functionalities, semiconducting and magnetic characteristics of the inorganic nanostructures could be combined together to synthesize noble metal—semiconductor,[11] noble metal—magnetic,[12] semicondutcor—magnetic nanoparticles.[13] Owing to the biocompatibility and localized surface plasmon resonance (SPR) properties, Au nanoparticles have been utilized as one of the component in multifunctional nanoparticle assemblies. The optical properties of the Au impart major advantages, as the SPR peak of the Au nanoparticles can be adjusted to near—infrared region, by tuning the size of the nanoparticles. Most, importantly the biological tissues are nearly transparent at these wavelengths,[11] which means they do not absorb in these regions which prevents the possibility of background signal error. Also, the emitted photon signals from Au nanoparticles could be easily analyzed through simple characterization techniques such as optical absorption, fluorescence characterizations.[11] The magnetic nanoparticles, such as FePt,[12] Fe_2O_3,[13] Fe_3O_4[14] nanoparticles has been evaluated in—vivo and in—vitro studies for their applicability in targeted drug delivery,[12] magnetic separation,[7] MRI contrast agents.[8] Owing to the remarkable features, synthesis of combination of magnetic—Au nanoparticles as a composite material has been the subject of interest. Well—established synthetic protocols has been described for iron oxide–Au coupled core–shell nanoparticle,[6] core—shell nanoparticles synthesis by a reverse micelle method,[14] surfactant assisted, solution based two—step method for the synthesis of Au—Fe_3O_4 nanoparticles,[16—18], synthesis of PbSe—Au—Fe_3O_4,[19] nanopartciles using binary Au—Fe_3O_4 as seed etc.

Dumbbell shaped multifunctional nanoparticles (DMNP) are the category of multifunctional nanoparticles, which consists of two nanoparticles with different functionalities joined together with a common interphase imparting new properties to the nanostructures.[20] There are many reports which describe the synthesis of DNPs, such as bifunctional Au—Fe_3O_4, synthesized through decomposition and oxidation of iron precursor over surface of Au nanoparticles in the presence of surfactants and solvents 1—octadecene, oleic acid and oleylamine.[21] The as formed Au—Fe_3O_4 DNPs can be further treated through additional heating process in the presence of S to fuse two Au nanoparticles together, forming complex Fe_3O_4—Au—Fe_3O_4 nanoparticles.[22] The DBNPs of Pt—Fe_3O_4 and Pd—Fe_3O_4 were synthesized by utilizing Pt and Pd nanoparticles as seed for the further controlled growth and oxidation of Fe, using $Fe(CO)_5$ as precursors.[23] The key observation to note here is, all the described primary synthetic protocols for the fabrication of DNPs employ the multi—step, solution phase synthesis, which imparts disadvantages use of solvents, and difficulty in the extraction of the product. On the other hand, the effective and successful chemical vapor deposition (CVD) technique has not been explored for the synthesis of multifunctional nanostructures. Thus it is essential to explore the versatile CVD methodology for the synthesis of DNBs. CoSe is a semiconducting material with the band gap of 1.52 eV.[24] Semiconducting properties combined with magnetic characteristics CoSe viable to use as dilute magnetic semiconducting. CoSe in bulk form has been synthesized through electrochemical deposition technique,[25] high pressure solid—state synthesis[26] and through mechanical alloying.[17] But these synthesis methodologies lacks the control of morphology, size and shape of the formed product. CoSe nanoparticles have been synthesized through microwave assisted polyol method using Co(II)acetate($Co(Ac)_2.4H_2O$) and sodium selenite ($Na_2SeO_3.5H_2O$), as precursors.[28] CoSe nanocrystlas were formed using metal acetate—paraffin approach, in the presence of olylamine surfactant,[29] and using hydrothermal method in presence of hydrazine, cobalt chloride and selenium.[30] But these methods also possess disadvantages of low control over morphology, inhomogenous nanoparticle morphology and size distribution.

In this communication, we report a simple, reproducible, solvent—less CVD protocol for the synthesis of dumbbell shaped Au—CoSe, which combines the semiconducting and magnetic characteristics of CoSe and SPR characteristics of Au nanoparticles. The reaction was carried out in a horizontal single zone furnace at 800°C, using cobalt acetylacetonate—$Co^{III}(C_5H_7O_2)_3$ which was kept at temperature zone of 200°C and Selenium which was kept at 400°C zones. These precursors sublime easily hence facilitate the growth of CoSe nanoparticles through Vapor—Liquid—Solid (VLS) growth mechanism using Au—Pd (3:2) as catalyst on Si substrate. At the end of the reaction, a golden—brown coating was obtained, covering the Si substrtae. The product was further characterized to understand the elemrntal, morphology composition, optical and magnetic properties through, powder X—ray diffraction (pxrd), scanning electron microscopy (SEM), scanning transmission electron microscopy (STEM), transmission electron microscopy (TEM), energy dispersive spectrometry (EDS), Raman spectroscopy and vibrating sample magnetometer (VSM).

Figure 1.1a demonstrates the pxrd pattern of the product, confirming the presence of CoSe (hexagonal structure, JCPDS card no— 42541) and Au utilized as a catalyst (JCPDS no 44362). The intense and sharp pxrd peaks suggest the presence of highly crystalline nature of the formed product. Figure 1.1b demonstrates the STEM image of the product, showing a huge yield of the dumbbell shaped morphology, presenting two different contrasts. In order to further characterize the product to understand the elemental composition and in—depth elemental analysis was carried out through EDS

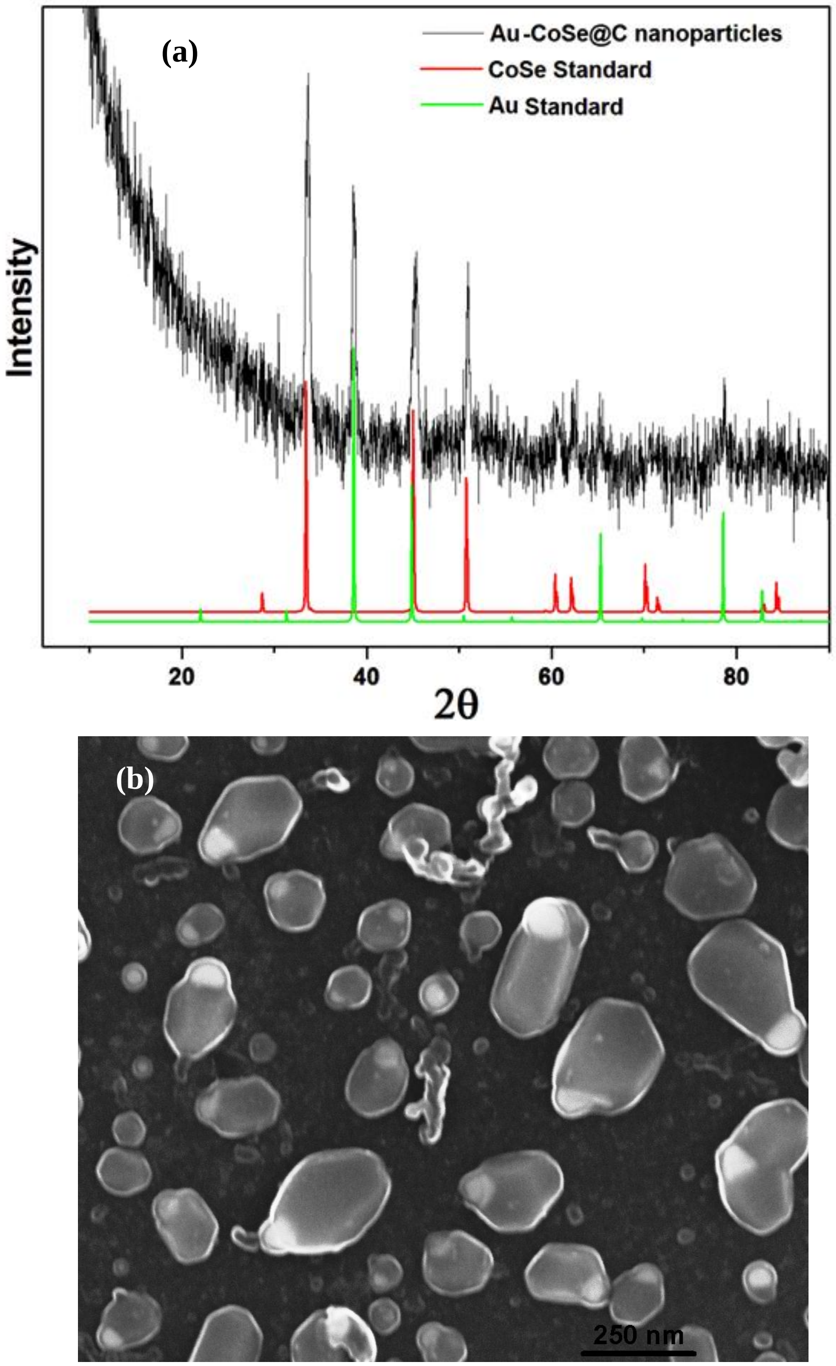

Figure 1.1 (a) XRD pattern collected from Au─CoSe nanoparticles, demonstrating the peaks matching with CoSe and Au standards. (b) Shows the SEM image of the nanoparticles, demonstrating the presence of dumbbell shaped morphology with distinct contrast difference.

line mapping and EDS elemental mapping. Figure 1.2 (a—e) shows the elemental mapping performed across a single dumbbell shaped nanoparticle. Figure 1.2a demonstrates the secondary electron image obtained during the elemental analysis. The analysis clearly depicts the presence of Au and Pd in the high contrast region and presence of Co, Se elements in the adjacent nanoparticle region, confirms the formation of Au—CoSe nanoparticles. Figure 1.2f shows the line mapping performed across the nanoparticle. The elements were assessed through line mapping in the region of line drawn from the location 1—2. A very high Au signal peaks up in the region of bright contrast. Though the Pd signal in the mapping is present in the region analogous to Au, from the line mapping it is clear that the amount of Pd in the nanoparticle region is

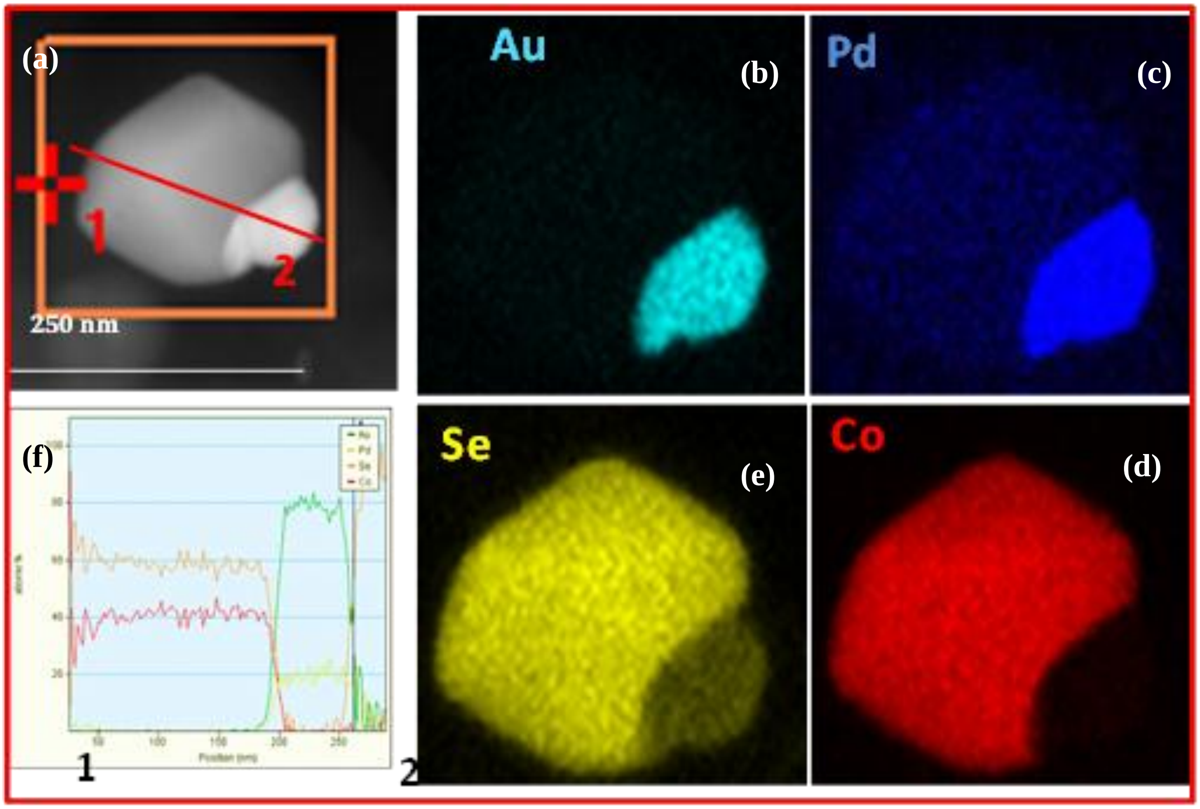

Figure 1.2 (a-e) EDS elemental mapping confirming the locations of Au, Pd, Co, Se elements. (f) demonstrates the line mapping performed across the single nanoparticle to analyze the intensity of the individual elements in both the adjacent nanoparticle components.

effectively less, and the nanoparticle region is rich in Au. In order to study the crystallinity of the CoSe, high resolution transmission electron microscopy (HRTEM) analysis was performed. Figure 1.3a shows a magnified view of the Au—CoSe, dumbbell shaped nanoparticle. Figure 1.3b demonstrates the HRTEM image which shows the cross fringes obtained from the CoSe region. The lattice fringes showed the *d*—spacings of 0.306 nm, which corresponds to the <100> lattice planes of the CoSe phase. The inset in the Figure 1.3b demonstrates the selected area diffraction pattern (SAED) obtained from the CoSe region of different nanoparticle. The SAED pattern can be indexed to (010), $(\bar{1}01)$, $(\bar{1}11)$ lattice planes.

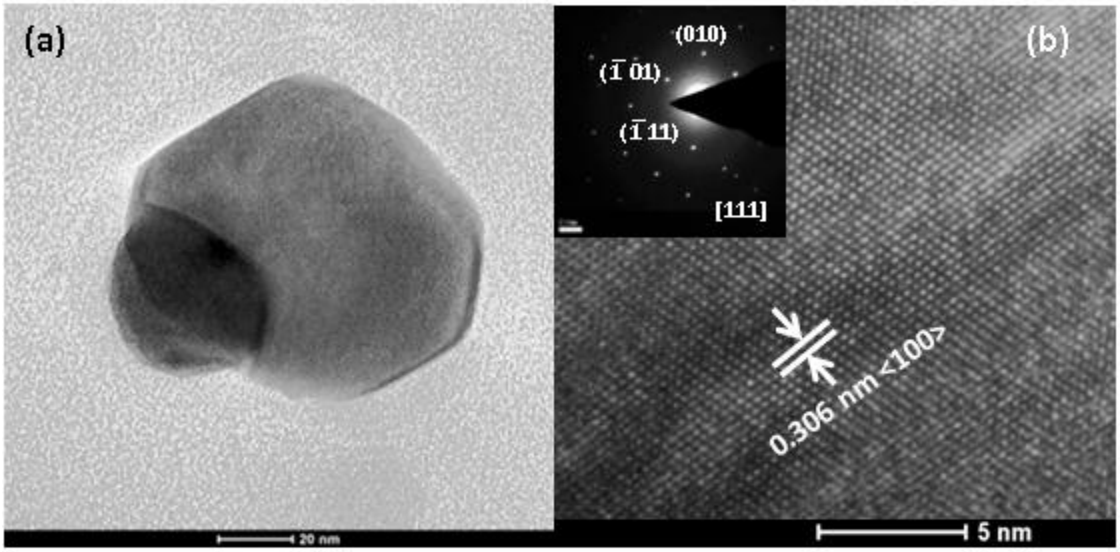

Figure 1.3 (a) TEM image of a single nanoparticle, clearly showing the union of two nanoparticls, through a common interphase. (b) HRTEM image of the CoSe region showing the lattice fringes which could be matched with (100) lattice planes of hexagonal CoSe. Inset showing the SAED pattern depicting high degree of crystallinity, and the spots could be indexed to (010), $(\bar{1}01)$, $(\bar{1}11)$ lattice planes of CoSe.

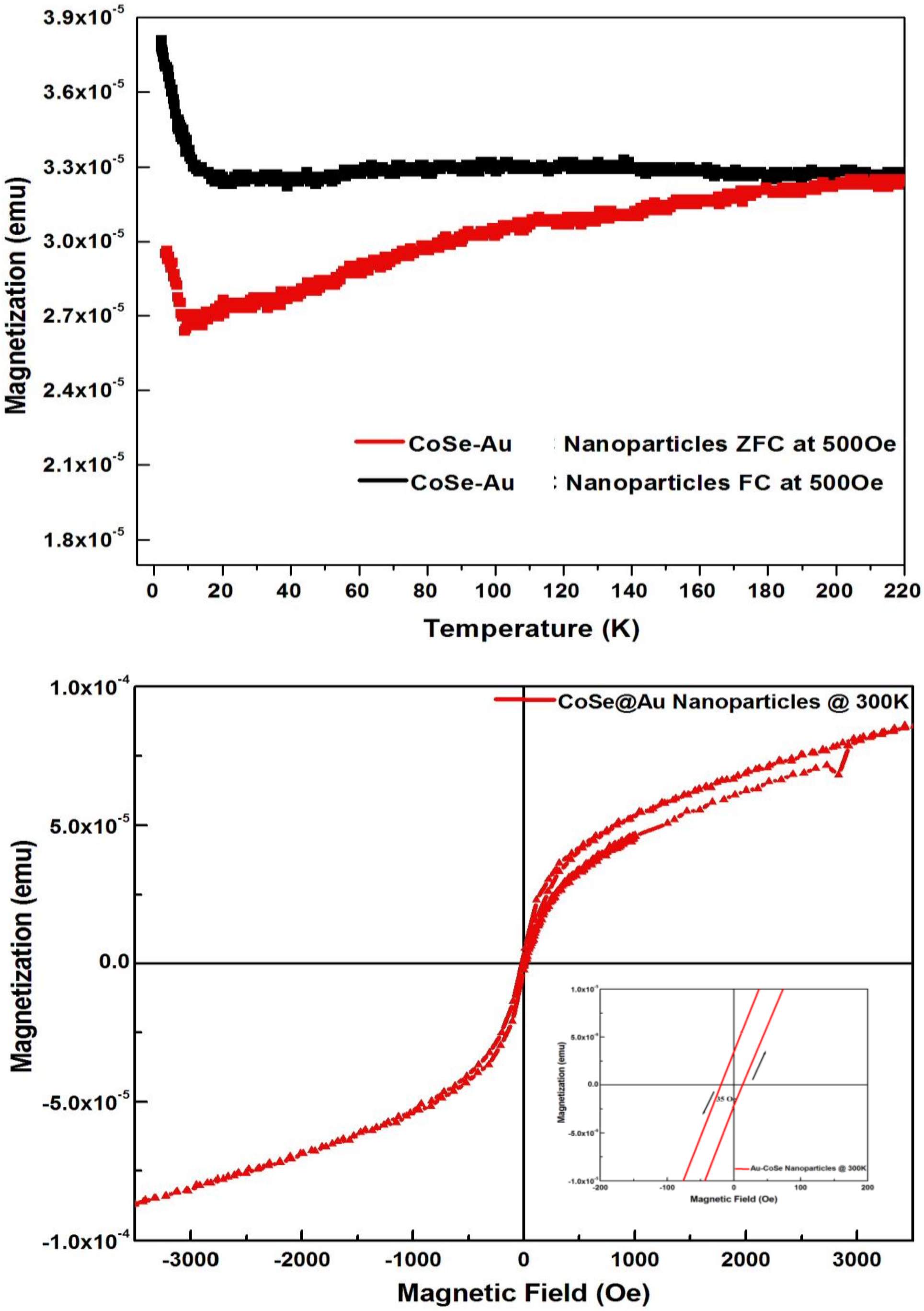

Figure 1.4 (a-b) Magnetic characterizations performed on the ensemble of Au─CoSe nanoparticles. (a) Shows the graph of magnetization Vs temperature in zero field cooled (ZFC) and field cooled (FC) conditions. (b) Shows the hysteresis loop obtained for the Au─CoSe nanoparticles.

corresponding to [111] zone axis. Supplementary figure S1, demonstrates the Raman spectroscopy analysis of the Au—CoSe nanoparticles. The characteristic Raman shift corresponds to the peaks reported in the literature for bulk CoSe.

Figure 1.4 a—b demonstrate the magnetic characterizations performed using vibrating sample magnetometer (VSM) on the 3 mm×3 mm area of the Si substrate covered with the Au—CoSe nanoparticles. Figure 1.4a demonstrates the magnetization versus temperature graph for the Au—CoSe nanoparticles sample recorded in a field of 500 Oe. It revealed a sharp transition at lower temperatures of 10K. The four quadrant M—H scan represented by Figure 1.4b also revealed that, the system has very low hysteresis with a coercive field H_c 35 Oe and a very low saturation field 3000 Oe. These observations confirm the presence of soft magnetic nature in Au—CoSe nanoparticles.

2. CONCLUSION

We have successfully synthesized, dumbbell shaped, multifunctional Au—CoSe nanoparticles, through facile, catalyst aided, chemical vapor deposition technique. The magnetic properties of the CoSe confirmed the soft ferromagnetic nature of the formed nanoparticles. The method described in this communications can be used to synthesize new multifunctional nanostructures by carefully choosing various other metal—acetylacetonate precursors, and catalyst particles to synthesize metal selenide—noble metal multifunctional nanostructures. The synthesis of DNBs depends on the control of the reaction parameters such that the conditions promote the heterogeneous nucleation.[20] In the initial stages of the reaction the Au—Pd catalyst agglomerates at high temperature and acts as a seed for the further reaction growth. As the reaction progresses, the Co and Se formed from the decomposition of the precursors, participate in the nucleation and growth of CoSe on bimetallic Au—Pd catalyst surface. This growth is not uniformly distributed over the entire catalyst surface; preventing the formation of core—shell type of morphology.

3. REFERENCES

1. Mout, R.; Moyano, D. F.; Rana, S.; Rotello, V. M. *Chem. Soc. Rev.* **2012**, *41*, 2539.

2. Sanvicens, N.; Marco, M. P. *Trends in Biotechnology* **2008**, *26*, 425.

3. Hanini, A.; Schmitt, A.; Kacem, K.; Chau, F.; Ammar, S.; Gavard, J. *Inter. J. Nanomed.* **2011**, *2011*, 787.

4. Carmona, R; Ana M. *Inter. J. Nanomed.* **2010**, *5*, 249.

5. Tiwari, P. M.; Vig, K.; Dennis, V. A.; Singh, S. R. *Nanomaterials* **2011**, *1*, 31.

6. Jokerst, J. V.; Gambhir, S. S. *Acc. Chem. Res.* **2011**, *44*, 1050.

7. Gu, H.; Xu, K.; Xua, C.; Xu, B. *Chem. Commun.* **2006**, 941.

8. Lu, H.; Yi, G.; Zhao, S.; Chen, D.; Guo, L. —H.; Cheng, Ji. *J. Mater. Chem.* **2004**, *14*, 1336.

9. Lim, I.I.; Njoki, P.N.; Park, H.Y, Wang, X.; Wang, L.; Mott, D.; Zhong, C.J. *Nanotechnology* **2008,** 19, 305102.

10. Rodríguez—González, B.; Attouchi, F.; Cardinal, M.F.; Myroshnychenko, V.; Stéphan, O.; García de Abajo, F.J.; Liz—Marzán, L.M.; Kociak, M. *Langmuir* **2012,** 28, 9063.

11. Huang, X. *et al. Nanomed.* **2007**, *2*, 681.

12. Hong, R.; Fischer, N. O.; Emrick, T.; Rotello, V. M. *Chem. Mater.* **2005**, *17*, 4617.

13. Bao, F.; Yao, J.L.; Gu, R. A. *Langmuir* **2009,** *25*, 10782.

14. Yin, G.; Huang, Z.; Deng, M.; Zeng, J.; Gu, J. *J. Colloid Interface Sci.* **2011,** *363*, 393.

15. Cho, S.; Idrobo, J.; Olamit, J.; Liu, K.; Browning, N. K.; Kauzlarich S. M. *Chem. Mater.* **2005**, *17*, 3181.

16. Caruntu, D.; Cushing, B.; Caruntu, G.; O'Connor, J. *Chem. Mater.* **2005**, *17*, 3398.
17. Yu, H.; Chen, M.; Rice, P. M.; Wang, S. X.; White, R. L.; Sun, S. *Nano Lett.* **2005**, *5*, 379.

18. Wang, L.; Luo, J.; Fan, Q.; Suzuki, M.; Suzuki, I. S.; Engelhard, M. H.; Lin, Y.; Kim, N.; Wang, J. Q.; Zhong, C. *J. Phys. Chem. B* **2005**, *109*, 21593.

19. Shi, W.; Sahoo, Y.; Zeng, H.; Ding, Y.; Swihart, M. T.; Prasad, P. N. *AdV. Mater.* **2006**, *18*, 1889.

20. Wang, C.; Xu, C.; Zeng, H.; Sun, S. *Adv. Mater.* **2009**, *21*, 3045.

21. Jin, Y.; Jia, C.; Huang, S.—W.; O'Donnell, M.; Gao, X.. *Nat. Comm.* **2012**, *41*, 2912.

22. Shi, W.; Zeng, H.; Sahoo, Y.; Ohulchskyy, T. Y.; Ding, Y.; Wang, Z. L.; Swihart, M.; Prasad, P. N. *Nano Lett.* **2006**, *6*, 875.

23. Wang, C.; Daimon, H.; Sun, S. *Nano Lett.* **2009**, *9*, 1493.

24. Liu, F.; Wang, B.; Lai, Y.; Li, J.; Zhang, Z.; Liu, Y. *J. Electrochem. Soc.* **2010**, *157* D523—D527.

25. Chang, K. J.; Lahn, S. M.; Chang, J. Y. *J. Appl. Phys.* **2006**, *89*, 182118.

26. Sreekumar, R.; Jayakrishnan. R.; Kartha, C. S.; Vijayakumar, K. P.; Khan, S. A.; Avasthi, D. K. *J. Appl. Phys.* **2008**, *103*, 023709.

27. Robinson, R. J. Kun, Z. K. *Appl. Phys. Lett.* **1975**, *27*, 74.

28. Haase, M. A.; Qiu, J.; Depuydt, J. M.; Cheng, H. *Appl. Phys. Lett.* **1991**, *59*, 1272.

29. Colli, A.; Hofmann, S.; Ferrari, A. C.; Ducati, C.; Martelli, F.; Rubini, S.; Cabrini, S.; Franciosi, A.; Robertson. J. *Appl. Phys. Lett.* **2005**, *86*, 153103.

30. Gao, J.; Zhang, B.; Zhang, X.; Xu, B. *Angew. Chem.* **2006**, *118*, 1242.

SECTION

5. FUTURE PROSPECTS

5.1. Pd NANOPARTICLE CATALYZED SYNTHESIS OF FeSe NANOPARTICLES

As described in the manuscripts, it was concluded that the catalyst—FeSe interphase plays a crucial role in the enhancement of the superconducting transition temperature of *entrapped*—FeSe in the Au—Pd/Se biphasic nanoparticles encapsulated by carbonaceous shell. Taking motivation from this exceptional observation, it is expected that, a higher enhancement in the transition temperature could be achieved through internal pressure effect owing to the increased interfacial area of FeSe. As ‘Au’ acts as an inactive catalyst particle, an experiment consisting of only Pd nanoparticles may produce a core—shell type of morphology as demonstrated in the schematic. The reaction would ideally take place on the entire outer surface of the active Pd nanoparticles, effectively coating the formed FeSe as a thin film over the Pd/Pd─Se core. In order to achieve this, the Pd nanoparticles synthesized from the physical vapor deposition technique are utilized as a thin film on Si substrate.

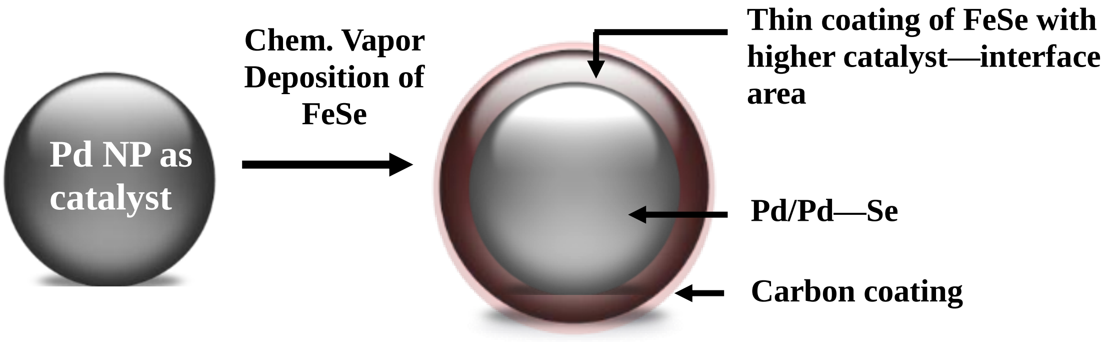

Figure 5.1. Schematic demonstrating the objective of the formation of Pd-Se—FeSe, Core—Shell Nanoparticles, summarizing the anticipation of a larger area of catalyst ─FeSe interphase.

5.2. HYDROCARBON FREE SYNTHESIS OF CARBON NANOTUBES

As described earlier, CVD method has been extensively employed in the synthesis of single walled and multiwalled carbon nanotubes. The established protocols utilize hazardous precursor gases such as acetylene, ethylene, ethanol, methane, 2-methyl-1,2′-naphthyl ketone as a source of carbon. Additionally, to initiate the growth of the nanotubes reducing agents are incorporated in the form of ammonia, nitrogen and hydrogen gases. Transition metals such as Fe, Ni or mixture combination are used to catalyze the reaction.

It has been observed that the CVD protocol which has been described for the synthesis superconducting FeSe nanostructures, unintentionally led to the formation of carbon nanofibers. Figure S12 shows the large area image of the carbon nanofibers formed during the course of the reaction, and the inset shows the HRTEM image of the nanofibers. Magnified images of carbon nanofibers shows presence of ordering and lattice fringes, which suggests that slight modification in the reaction design may led to the formation of multiwalled/single walled carbon nanotubes. In the absence of Se vapors, the reaction condition results in an ideal state for the synthesis of carbon nanotubes, as the Fe(acac)$_3$ is a source of Fe catalyst as well as carbon. As Fe(acac)$_3$ is easily sublimable at low temperature (180°C), the Si substrate could be pre—coated with thin layer of sublimed Fe(acac)$_3$ using sublimator, to insure the Fe catalytic action on the substrate. Exploring this new CVD protocol will enable us to use acetyl acetonates in the synthesis of carbon nanotubes without using hazardous gases in typically inexpensive reactor design, enabling large scale synthesis.

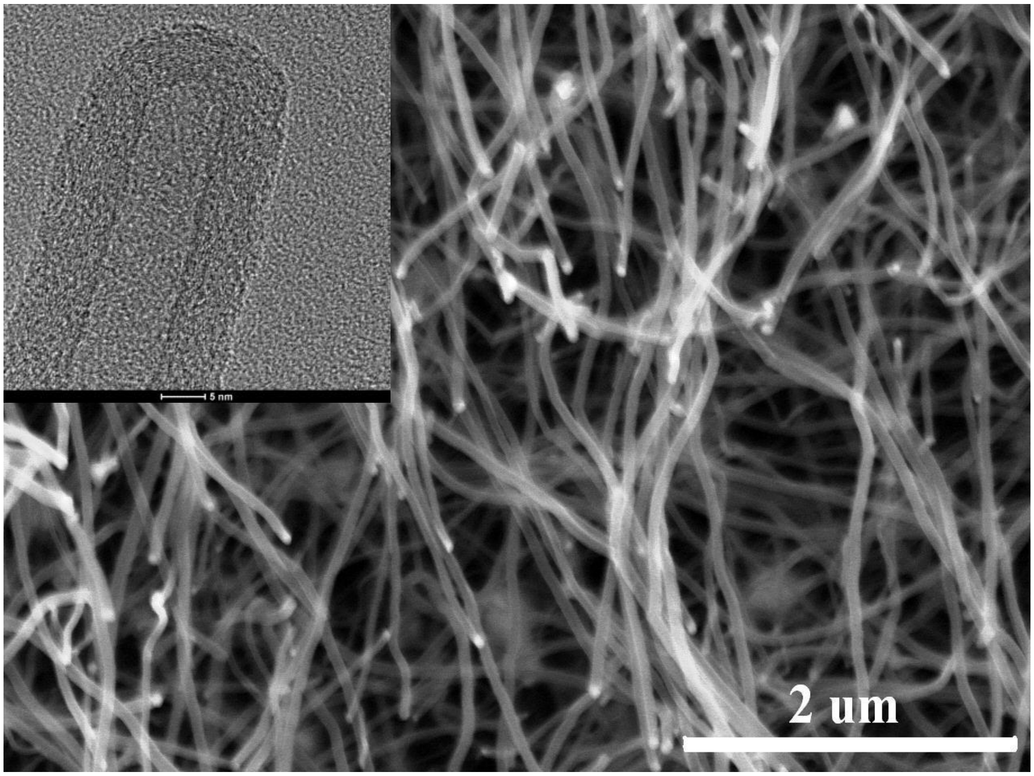

Figure 5.2. SEM image collected from the black product obtained during CVD reaction protocol, demonstrating the presence of carbon nanotubes. Inset shows the HRTEM image of a single nanotube, demonstrating minimal presence of lattice fringes.

5.3. APPLICATION OF MULTIFUNCTIONAL NANOPARTICLES IN THERONOSTIC STUDIES

Using this established protocol, it is possible to design and synthesize new multifunctional nanostructures with well—tailored properties. The attempts would be made to explore and analyze the effectiveness of Au—CoSe nanopartciels in biomedical applications especially in imaging, sensing and therapeutic applications.

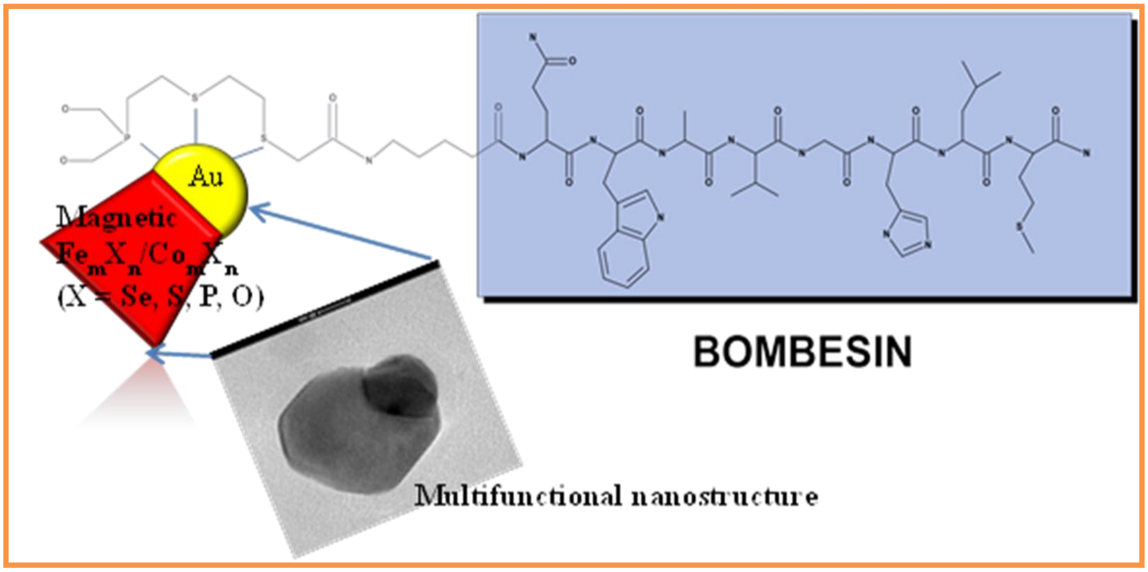

Figure 5.3.Scheme showing grafting of the peptide on the Au-Fe_mX_n (X = O, P, S, Se etc.) through attachment at the Au-part of the multifunctional nanoparticle.

5.4. SYNTHESIS OF METAL SELENIDE NANOSTRUCTURES

The experimental method, chemical vapor deposition described here is extremely versatile and can be extended to synthesize other metal selenide nanostructures by varying the reactor design, temperature profile, choice of the precursors, N_2 flow rate, the temperature profiles of the substrate and precursors, choice of catalyst and inclusion of rector gases such as acetylene, hydrogen as oxidizing of reducing agents.

A table summarizing the possible elemental compositions along with their characteristic physical properties is described below:

Table 5.1. Table compiling the properties of metal selenides and established synthesis protocols showing the inherent drawbacks of the synthesis route.

Compound (Metal selenide)	Precursor	Physical Properties	Established Synthesis (drawbacks)
Indium Selenide (In_2Se_3)	Indium Acetylacetonate	Photovoltaic Applications (Direct band gap 1.93 eV)[26]	MOCVD — Trimethyl Indium[25] (Use of hazardous H_2Se gas)
Zinc Selenide (ZnSe)	Zinc acetylacetonate hydrate	Light emitting diode[27]— blue/green laser[28] (band gap = 2.70 eV)[27]	Catalyst assisted Molecular Beam Epitaxy[29] (non—homogenous nanowires)
Cobalt Selenide	Cobalt acetylacetonate (sublimation temperature= 210°C)	Ferromagnetic, applications as catalyst	Solvothermal Method (Difficult extraction of the product from solution)[30]

BIBILIOGRAPHY

1. Wenjie Mai, Synthesis, characterization and application of zinc oxide nanomaterials By Georgia Institute of Technology

2. Zhao, M.; Sun, L.; Crooks, R. M. *J. Am. Chem. Soc.* **1998**, *120*, 4877. Zhao, M.; Crooks, R. M. *Adv. Mater.* **1999**, *11*, 217. Niu, Y.; Yeung, L. K.; Crooks, R. M. *J. Am. Chem. Soc.* **2001**, *123*, 6840. Gro¨hn, F.; Gu, X.; Gru¨ ll, H.; Meredith, J. C.; Nisato, G.; Bauer, B. J.; Karim, A.; Amis, *E. J. Macromolecules* **2002**, *35*, 4852. Scott, R. W. J.; Datye, A. K.; Crooks, R. M. *J. Am. Chem. Soc.* **2003**, *125*, 3708. Chung, Y.—M.; Rhee, H.—K. *Catal. Lett.* 2003, *85*, 159.

3. Rao, C. N. R.; Cheetham, A. K. *J. Mater. Chem.* 2001, *11*, 2887.

4. Feynman, R. P. *California Institute of Technology Journal of Engineering and Science* **1960**, *4(2)*, 23.

5. Kroto, H. W.; Heath, J. R.; O'Brien, S. C.; Curl, R. F.; Smalley, R. E. *Nature*, **1985**, *318*, 167.

6. Iijima, S. *Nature*, **1991**, *354*, 56.

7. Jones, R. *Physics Worls*, **2004**, 25.

8. Whitesides, G. M. *Small*, **2005**, *1*, 172.

9. Alivisatos, A. P. *Science*, **1996**, *271*, 933.

10. Pankhurst, Q. A.; Connolly, J.; Jones, S. K.; Dobson, J. *J. Phys. D: Appl. Phys.* **2003**, *36*, R167.

11. Borrelli, N. F.; Hall, D. W.; Holland, H. J.; Smith, D. W. *J. Appl. Phys.***1987**, *61*, 5399.

12. Willets, K. A.; Richard, P.; Duyne, V. *Annu. Rev. Phys. Chem.* **2007**, *58*, 267.

13. Sherry, L. J.; Chang, S. –H.; Schatz , G. C.; Richard, P.; Duyne, V. *Nano Lett.* **2005**, *5 (10)*, 2034.

14. Hoa, X.D.; Kirk, A.G.; Tabrizian, M. *Biosensors and Bioelectronics*, **2007**, *23*, 151.

15. Wang, Y. *et al Nanotechnology* **2007**, *18*, 465701.

16. Chakka, V. M.; Altuncevahir, B.; Jin, Z. Q.; Li, Y.; Liu, J. P. *J. Appl. Phys.* **2006**, *99*, 08E912.

17. Damontea, L.C.; Zélisa, L.A. Mendoza; Soucaseb, B. Marí; Fenollosab, M.A. Hernández. *Powder Technology* **2004**, *148*, 15.

18. Lin, C. -R.; Chu, Y.-M.; Wang, S.-C. *Materials Letters* **2006,** *60***,** 447.

19. Lam, C.; Zhang, Y.F.; Tang, Y.H.; Lee, C.S.; Bello, I.; Lee, S.T. *Journal of Crystal Growth* **2000,** *220*, 466.

20. Giri, P. K.; Bhattacharyya, S.; Singh, Dilip K.; Kesavamoorthy, R.; Panigrahi, B. K. , Nair, K. G. M. *Journal of Applied Physics* **2007**, *102*, 093515.

21. Wang, Yiping; Li, Yang; Rong, Chuanbing; Liu, J Ping. *Nanotechnology* **2007**, *18*, 465701.

22. M. N. Rahaman, *Ceramic Processing and Sintering*, 2nd ed. Marcel Dekker, New York, 2003.

23. Akdogan, N. G.; Hadjipanayis, G. C.; Sellmyer, D. J. *Journal of Applied Physics* **2009,** *105*, 07A710.

24. Zhang, D. W.; Chen, C. H.; Zhang, J.; Ren, F. *Chem. Mater.* **2005**, *17*, 5242.

25. Lam, C; Zhang, Y.F.; Tang, Y.H.; Lee, C.S.; Bello, I.; Lee, S.T. *Journal of Crystal Growth* **2000**, *220*, 466.

26. Yue, M.; Wang, Y. P.; Poudyal, N.; Rong, C. B.; Liu, J. P. *J. Appl. Phys.* **2009**, *105*, 07A708.

27. Cui, B. Z.; Gabay, A. M.; Li, W. F.; Marinescu, M.; Liu, J. F.; Hadjipanayis, G. C. *J. Appl. Phys.* **2010**, *107*, 09A721.

28. Saravanan, P.; Gopalan, R; Rao, N V Rama; Raja, M Manivel; Chandrasekaran, V. *J. Phys. D: Appl. Phys.* **2007**, *40*, 5021

29. Kima, Y.A.; Hayashia, T.; Fukaia, Y.; Endoa, M.; Yanagisawab, T.; Dresselhausc, M.S. *Chemical Physics Letters* **2002**, *355*, 279.

30. Pierarda, N; Fonsecaa, A; Konyaa, Z; Willemsa, I; Tendeloob, G Van; Nagya, J. B. *Chemical Physics Letters*

31. Li, Y.B.; Wei, B.Q.; Liang, J.; Yu, Q.; Wu, D.H. **2001**, *335*, 1.

32. Pawlak, B. J.; Gregorkiewicz, T.; Ammerlaan, C. A. J.; Takkenberg, W.; Tichelaar, F. D.; Alkemade, P. F. A. *Phys. Rev. B* **2001**, *64*, 115308.

33. Chen, Y.; Gerald, J. Fitz; Williams, J.S.; Bulcock, S. *Chemical Physics Letters* **1999,** *299*, 260.

34. Gasgnier, M.; Szwarc, H.; Chen, A. R.; Chadderton, L. T.; Gerald, J. F.; Williams, J. S. *Appl. Phys. Lett.* **1999**, *74*, 2960.

35. Lee, J. S., Park, K.; Kang, M. I.; Park, I. W.; Kim, S. W.; Cho, W. K.; Han, H. S.; Kim, S. *J. Cryst. Growth* **2003**, *254*, 423.

36. Guozhong Cao, Ying Wang, Nanostructures and nanomaterials: synthesis, properties, and application, **2010**, World Scientific, Singapore, Volume 2, Aug 31.

37. Atushi Muramatsu, Tokuji Miyashita, *Nano—hybridization of organic—inorganic materials*, Pg 33.

38. Fritz Vögtle, M. Ballauf, *Dendrimers III: design, dimension, function* Springer, 212, VBH NewYork.

39. Ganesan, M.; Freeantle, R. G.; Obare, S. O. *Chem. Mater.* **2007**, *19*, 3464.

40. Guozhong Cao, Ying Wang, *Nanostructures and nanomaterials: synthesis, properties, and application,* **2010,** World Scientific, Singapore, Volume 2, Aug 31.

41. Donegá, C. M.; Liljeroth, P.; Vanmaekelbergh, D. *Small*, **2005**, *1*, 1152.

42. Zhang, L. J.; Shen, X. C.; Liang, H.; Guo, S.; Liang, J. H. *J. Coll. Inter. Sci.* **2010**, 342, 236.

43. Stouwdam, J. W.; Janssen, R. A. J. *J. Mater. Chem.* **2008**, *18*, 1889.

44. Shevchenko, E. W.; Talapin, D. V.; Schnablegger, H.; Kornowski, A.; Festin, O.; Svedlindh , P.; Haase, M.; Weller, H. *J. Am. Chem. Soc.*, **2003**, *125*, 9090.

45. Kim, D.; Lee, N.; Park, M.; Kim, B. H.; An, K.; Hyeon, T. *J. Am. Chem. Soc.*, **2009**, *131*, 454.

46. Houtepen , A. J.; Koole , R.; Vanmaekelbergh , D.; Meeldijk , J.; Hickey, S. G. *J. Am. Chem. Soc.*, **2006**, *128*, 6792.

47. Liu, T. Y.; Li, M.; Ouyang, J.; Zaman , M. B.; Wang, R.; Wu, X.; Yeh, C. S.; Lin , Q.; Yang, B.; Yu, K. *J. Phys. Chem. C*, **2009**, *113* , 2301.

48. Desai, P.; Song, K.; Koza, J.; Pariti, A.; Nath, M. *Chem. Mater.*, **2013,** 1510.

49. Reina, Alfonso; Jia, Xiaoting; Ho, John; Nezich, Daniel; Son, Hyungbin; Bulovic, Vladimir; Dresselhaus, Mildred S.; Kong, Jing. *Nano Lett.* **2009**, *9*, 30.

50. Gomez, L.; Zhang, Y.; Kumar, A.; Zhou, C. *IEEE Trans. Nanotechnol.* **2009**, *8*, 135.

51. Arco, Lewis Gomez De; Zhang, Yi; Schlenker, Cody W.; Ryu, Koungmin; Thompson, Mark E.; Zhou, Chongwu. **2010**, *4,* 2865.

52. Kim, K. S. *et al*. *Nature* **2009**, *457*, 706.

53. Li, X. S. et al. *Science* **2009**, *324*, 1312.

54. Bae, S. et al. *Nature Nanotech.* **2010**, 5, 574.

55. Li, Z.; Wu, P.; Wang, C.; Fan, X.; Zhang, W.; Zhai, X; Zeng, C; Li, Z.; Yang, J.; Hou, J. *small*, **2011**, *5*, 3385.

56. Walker, P. L.; Rakszawski, J. F.; Imperial, G. R. *J. Phys. Chem.* **1959**, 63 (2): 133.

57. José—Yacamán, M.; Miki—Yoshida, M.; Rendón, L.; Santiesteban, J. G. *Appl. Phys. Lett.* **1993**, *62*, 657.

58. Cantoro, M.; Hofmann, S.; Pisana, S.; Scardaci, V.; Parvez, A.; Ducat, C.; Ferrari, A. C.; Blackburn, A. M.; Wang, K. Y.; Robertson, J. *Nano Lett.* **2006,** *6*, 1107.

59. Lee, C. J. *et. al. Appl. Phys. Lett.* **1999**, *75*, 1721.

60. Huang, Z. P.; Xu, J. W.; Ren, Z. F.; Wang, J. H.; Siegal, M. P.; Provencio, P. N. *Appl. Phys. Lett.* **1998**, *73*, 3845.

61. Dai, H. *Acc. Chem. Res.* **2002**, *35*, 1035.

62. Wagner, R. S.; Ellis,W. C. *Appl. Phys. Lett.* **1964**, *4*, 89.

63. Onnes, H. K. *Commun. Phys. Lab.* **1911**,*12*, 120.

64. Stephen Blundell, Superconductivity— A very short introduction, oxford university press

65. Wu, M. K.; Ashburn, J. R.; Torng, C. J.; Hor, P. H.; Meng, R. L.; Gao, L.; Huang, Z. J.; Wang, Y. Q.; Chu, C. W. *Physi. Rev. Lett.* **1987**, *58*, 908.

66. Sheng, Z. *et al. Physi. Rev. Lett.* **1988**, *60*, 937.

67. J. Bardeen; L. N. Cooper; J. R. Schrieffer (1957). "Theory of superconductivity". Physical Review B 108 (1175): 162–164.

68. Superconductivity, Superfluids and Condensates, By James F. Annett Page 58—59.

69. Room—temperature Superconductivity By Andrei Mourachkine, Cambridge International Science Publishing, Cambridge, page 41.

70. Giancoli, Douglas (2009) [1984]. "25. Electric Currents and Resistance". In Jocelyn Phillips (ed.). Physics for Scientists and Engineers with Modern Physics (4th ed.)

71. Kamihara, Y.; Hiramatsu, H.; Hirano, M.; Kawamura, R.; Yanagi, H.; Kamiya, T.; Hosono, H. “Iron—Based Layered Superconductor: LaOFeP” *J. Am. Chem. Soc.* **2006**, *128*, 10012—10013.

72. Watanabe, T.; Yanagi, H.; Kamiya, T.; Kamihara, Y.; Hiramatsu, H.; Hirano, M.; Hosono, H. “Nickel—Based Oxyphosphide Superconductor with a Layered Crystal Structure, LaNiOP” *Inorg. Chem.* **2007**, *46*, 7719—7721.

73. Kamihara, Y.; Watanabe, T.; Hirano, M.; Hosono, H. *J. Am. Chem. Soc.* **2008**, *130*, 3296—3297.

74. Johrendt, D.; Pottgen, R. *Chem. Int. Ed.* **2008**, *47*, 4782—4784. Chen, G. F.; Li, Z.; Li, G.; Hu, W. Z.; Dong, J.; Zhang, X. D.; Zheng, P.; Wang, N. L.; Luo, J. L *Chin. Phys. Lett.* **2008**, *25*, 3403—3406. Chen, X. H.; Wu, T.; Wu, G.; Liu, R. H.; Chen. H.; Fang, D. F. *Nature*, **2008**, 435, 761—762.

75. Zheng, W.; Hai'ou, L.; WeiLi, H.; Zhangming, L.; Huiyan, W.; Xiufeng, G.; Keqing, R. *J. Supercond. Nov. Magn.* **2008**, *21,* 213—215.

76. Rotter, M.; Tegel, M.; Johrendt, D. *Phys. Rev. Lett.* **2008**, *101,* 107006—10.

77. Rotter, M.; Tegel, M.; Schellenberg, I.; Hermes, W.; Pöttgen, R.; Johrendt, D. *Phys. Rev. B* **2008,** *78*, 020503—07(R).

78. Wang, X.C.; Liu, Q.Q.; Lv, Y.X.; Gao, W.B.; Yang, L.X.; Yu, R.C.; Li, F.Y.; Jin, C.Q. *Solid State Commun.* **2008**, *148,* 538—540.

79. Wang, X. C.; Liu, Q. Q.; Deng, Z.; Lv, Y. X.; Gao, W. B.; Zhang, S. J.; Yu, R. C.; Jin, C. Q. *J. Supercond. Nov. Magn.* **2010**, *23*, 583—585.

80. Hsu, F. C.; Luo, J.—Y.; Yeh, K.—W.; Chen, T. K.; Huang, T.—W.; Wu, P. M.; Lee, Y.—C.; Huang, Y.—L.; Chu, Y.—Y.; Yan, D.—C.; Wu, M.—K. *Proc. Natl. Acad. Sci.* **2008**, *105*, 14262—14264.

81. Yeh, K—W.; Huang, T—W.; Huang, Y—L.; Chen T—K.; Hsu, F—C.; Wu, P. M.; Lee, Y—C.; Chu, Y—Y.; Chen, C—L.; Luo, J—Y.; Yan, D—C.; Wu, M—W. *Europhys. Lett.* **2008**, *84*, 37002.

82. Guo, J.; Jin, S.; Wang, G.; Wang, S.; Zhu, K.; Zhou, T.; He, M.; Chen, X *Phys. Rev. B* **2010**, *82*, 180520—04(R).

83. Palstra, T. T.; Batlogg, B.; van Dover, R. B.; Schneemeyer, L. F.; Waszczak, J. V. *Phys. Rev. B* **1990**, *41*, 6621—6632.

84. Suzuki, M.; Anayama, T.; Watanabe, K.; Toyota, N.; Kobayashi, N.; Noto, K.; Muto, Y. *Jpn. J. Appl. Phys.* **1985**, *24*, L767—L769.

85. Mamalis, A. G.; Hristoforou, E.; Theodorakopoulos, I. D.; Prikhna, T. *Supercond. Sci. Technol.* **2010**, *23*, 095011.

86. Ekin, J. W.; Salama, K.; Selvamanickam, V. *Appl. Phys. Lett.* **1991**, *59*, 360—363.

87. Senatore, C.; Flükiger, R.; Cantoni, M.; Wu, G.; Liu, R.—H.; Chen, X.—H. *Phys. Rev. B*, **2008**, *78*, 054514 (7pp).

88. Ren, Z. A.; Lu, W.; Yang, J.; Yi, W.; Shen, X.—L.; Li, Z.—C.; Che, G.—C.; Dong, X.—L.; Sun, L.—L.; Zhou, F.; Zhao, Z.—X. *Chin. Phys. Lett.* **2008**, *25*, 2215.

89. Qi, Y.; Wang, L.; Wang, D.; Zhang, Z.; Gao, Z.; Zhang, X.; Ma, Y. *Supercond. Sci. Technol.* **2010**, *23*, 055009.

90. Yang, H.; Luo, H.; Wang, Z.; Wen, H. —H. *Appl. Phys. Lett.* **2008**, *93*, 142506.

91. Song, Y. J.; Ghim J. S.; Min, B. H.; Kwon, Y. S.; Jung, M. H.; Rhyee, J.—S. *Appl. Phys. Lett.* **2010**, *96*, 212508 (3pp).

92. Lei, H.; Hu, R.; Petrovic, C. *Phys. Rev. B* **2011**, *84*, 014520 (5pp).

93. Gao, Z.; Qi, Y.; Wang, L.; Yao, C.; Wang, D.; Zhang, X.; Ma, Y. arXiv:1103.2904v2, **2012**.

94. Takahashi, H.; Igawa, K.; Arii, K.; Kamihara, Y.; Hirano, M.; Hosono, H. *Nature* **2008**, *435*, 376.

95. Zhang, S. J.; Wang, X. C.; Sammynaiken, R.; Tse, J. S.; Yang, L. X.; Li, Z.; Liu, Q. Q.; Desgreniers, S.; Yao, Y.; Liu, H. Z.; Jin, C. Q. *Phys. Rev. B* **2009**, *80*, 014506.

96. Alireza, P. L.; Ko, Y. T. C.; Gillett, J.; Petrone, C. M.; Cole, J. M.; Lonzarich, G. G.; Sebastian, S. E. *J. Phys. Condens. Mat.* **2009**, *21*, 012208 (4pp).

97. Margadona, S.; Takabayashi, Y.; Ohishi, Y.; Mizuguchi, Y.; Takano, Y.; Kagayama, T.; Nakagawa, T.; Takata, M.; Prassides, K. *Phys Rev. B*, **2009**, *80*, 064506 (6pp).

98. Medvedev, S.; McQueen T. M.; Troyan, I. A.; Palasyuk, T.; Eremets M. I.; Cava R. J.; Naghavi, S.; Casper, F.; Ksenofontov, V.; Wortmann, G.; Felser, C. *Nature Materials* **2009**, *8*, 630—633.

99. Nagamatsu, J.; Nakagawa, N.; Muranaka, T.; Zenitani, Y.; Akimitsu, J. *Nature*, **2001**, *410*, 63—64.

100. Takabayashi, Y.; Ganin, A. Y.; Jeglic, P.; Arcon, D.; Takano, T.; Iwasa, Y.; Ohishi, Y.; Takata, M.; Takeshita, N.; Prassides, K.; Rosseinsky, M. J. *Science* **2009**, *323*, 1585—1590.

101. Gresty, N. C.; Takabayashi, Y.; Ganin, A. X.; McDonald, M. T.; Claridge, J. B. Giap, D.; Mizuguchi, Y.; Takano, Y.; Kagayama, T.; Ohishi, Y.; Takata, M.; Rosseinsky, M. J.; Margadonna, S.; Prassides, K. *J. Am. Chem. Soc.* **2009**, *131*, 16944—16952.

102. Shein, I. R.; Enyashin, A. N.; Ivanovskii, A. L. *Computational Mater. Sci.* **2011**, *50*, 824—827.

103. Pauzauskie, P.; Yang, P. *Materials Today (Oxford, England)* **2006**, *9*, 36.

104. Bin, Y.; Meyyappan, M. *Nano and Molecular Electronics Handbook*, Editors(s): Lyshevski, S. Edward **2007**, *7/1—7/9*, CRC Press, LLC, Fla.

105. Pearton, S. J.; Kang, B. S.; Gila, B. P.; Norton, D. P.; Kryliouk, O.; Ren, F.; Heo, Young—Woo; Chang, Chih—Yang; Chi, Gou—Chung; Wang, Wei—Ming; Chen, Li—Chyong *J. Nanosci. Nanotech.* **2008**, *8*, 99—110.

106. Bezryadin, A. *J. Phys.: Condens. Matter* **2008**, *20*, 043202.

107. Bezryadin, A.; Lau, C. N.; Tinkham, M. *Nature* **2000**, *404*, 971—974.

108. Tian,M.; Wang,J.; Snyder, J.; Kurtz, J.; Liu, Y.; Schiffer, P.; Mallouk, T. E.; Chan, M. H. W. *Appl. Phys. Lett.* **2003**, *8*, 1620 (3pp).

109. Moshchalkov, V. V.; Fritzsche, J. *Nanostructured Superconductors,* World Scientific Publishing Co Pte Ltd, Singapore, **2011**, 257.

110. Araújo, M. A. N.; García—García, A. M.; Sacramento, P. D. *Phys. Rev. B* **2011**, *84*,172502.

111. Wang, Y. G.; Zou, B. S.; Wang, T. H.; Wang, N.; Cai, Y.; Chan Y. F.; and Zhou, S. X. Nanotechnology, 2006, 17, 2420.

112. Piraux, L.; George, J. M.; Despres, J. F.; Leroy, C.; Ferain, E.; Legras, R.; Ounadjela, K.; Fert, A. *Appl. Phys. Lett.* **1994**, *65*, 2484. Piraux, L.; Dubois, S.; Fert, A.; *J. Magn. Magn. Mater.* **1996**, *159*, L287. Piraux, L.; Dubois, S.; Fert, A.; Belliard, L. *Eur. Phys. J. B* **1998**, *4*, 413. Dubois, S.; Marchal, C.; Beuken, J. M.; Piraux, L.; Duvail, J. L.; Fert, A.; George, J. M.; Maurice, J. L. *Appl. Phys. Lett.* **1997**, *70*, 396. Liu, K.; Nagodawithana, K.; Searson, P. C.; Chien, C. L. *Phys. Rev. B* **1995**, *51*, 7381. Chen, M.; Searson, P. C.; Chien, C. L. *J. Appl. Phys.* **2003**, *93*, 8253. Chen, M.; Sun, L.; Bonevich, J. E.; Reich, D. H.; Chien, C. L.; Searson, P. C. *Appl. Phys. Lett.* **2003**, *82*, 3310.

113. PeÇa, D. J.; Mbindyo, K. N.; Carado, A. J.; Mallouk, T. E.; Keating, C. D.; Razavi, B.; Mayer, T. S.; *J. Phys. Chem. B* **2002**, *106*, 7458. Kovtyukhova, N. I.; Martin, B. R.; Mbindyo, J. K. N.; Mallouk, T. E.; Cabassi, M.; Mayer, T. S. *Mater. Sci. Eng. C* **2002**, *19*, 255. Kovtyukhova, N. I.; Kelley, B. K.; Mallouk, T. E. *J. Am. Chem. Soc.* **2004**, *126*, 12738.

114. Sun, S.; Murray, C. B.; Weller, D.; Folks, L.; Moser, A. *Science* **2000**, *287*, 1989.

115. Pellegrino, T.; Fiore, A.; Carlino, E.; Giannini, C.; Cozzoli, P. D.; Ciccarella, G.; Respaud, M.; Palmirotta, L.; Cingolani, R.; Manna, L. *J. Am. Chem. Soc.* **2006**, *128*, 6690.

116. Chen, M.; Nam K.; Yong, Moo L. H.; Li, C.; Cho, S. O. *J. Phys. Chem. C* **2008**, *112*, 8870.

117. Gao, J. H.; Liang, G. L.; Zhang, B.; Kuang, Y.; Zhang, X. X.; Xu, B. *J. Am. Chem. Soc.* **2007**, *129*, 1428.

118. Gao, J. H.; Liang, G. L.; Cheung, J. S.; Pan, Y.; Kuang, Y.; Zhao, F.; Zhang, B.; Zhang, X. X.; Wu, E. X.; Xu, B. *J. Am. Chem. Soc.* **2008**, *130*, 11828.

119. Hao, Rui; Xing, Ruijun; Xu, Zhichuan; Hou, Yanglong; Gao, Song; Sun, Shouheng. *Adv. Mater*, **2010**, *22*, 2729.

120. Skrabalak, S. E.; Chen, J. Y.; Sun, Y. G.; Lu, X. M.; Au, L.; Cobley, C. M.; Xia, Y. N. *Acc. Chem. Res.* **2008**, *41*, 1587.

121. Gao, J.; Gu, H; Xu, B. *Acc. of Chem. Res.* **2009**, *42*, 1097.

122. Gu, H. W.; Zheng, R. K.; Zhang, X. X.; Xu, B. *J. Am. Chem. Soc.* **2004**, *126*, 5664.

123. Kwon, K. W.; Shim, M. *J. Am. Chem. Soc.* **2005**, *127*, 10269.

124. Gu, H. W.; Zheng, R. K.; Liu, H.; Zhang, X. X.; Xu, B. *Small* **2005**, *1*, 402.

125. Wang, D. S.; He, J. B.; Rosenzweig, N.; Rosenzweig, Z. *Nano Lett.* **2004**, *4*, 409.

126. Kim, H.; Achermann, M.; Balet, L. P.; Hollingsworth, J. A.; Klimov, V. I. *J. Am. Chem. Soc.* **2005**, *127*, 544.

127. Jinhao, G.; Bei Z.; Yuan G.; Yue P.; Xixiang, Z.; Bing, X. *J. Am. Chem. Soc.* **2007**, *129*, 11928.

128. Allen, P. M.; Liu, W.; Chauhan, V. P.; Lee, J.; Ting, A.Y.; Fukumura, D.; Jain, R.K.; Bawendi, M. G. *J. Am. Chem. Soc.* **2010**, *132*, 470.

129. Kim, S. W.; Zimmer, J. P.; Ohnishi, S.; Tracy, J. B.; Frangioni, J. V.; Bawendi, M. G. *J. Am. Chem. Soc.* **2005**, *127*, 10526.

130. Guo, S.; Dong, S.; Wang, E. *Chem. Eur. J.* **2009**, *15*, 2416.

131. Chen, M.; Kim, Y. N.; Lee, H. M.; Li, C.; Cho, Sung O. *J. Phys. Chem. C* **2008**, *112*, 8870.

132. V. R. Reddy, *Thieme*, **2006**, 1791.

133. Michael Faraday, Philosophical Transactions of the Royal Society, London, 1857.

134. Cobley, C. M.; Chen, J.; Cho, E. C.; Wang, L. V.; Xia, Y. *Chem. Soc. Rev.* **2011**, *40*, 44.
135. Turkevich, J.; Stevenson, P. C.; Hillier, J. *Discuss. Faraday. Soc.* **1951**, *11*, 55.

136. Kimling, J.; Maier, M.; Okenve, B.; Kotaidis, V.; Ballot, H.; Plech, A. *J. Phys. Chem. B* **2006**, *110*, 15700.

137. Frens, G. *Colloid & Polymer Science* **1972**, *250*, 736.

138. Frens, G. *Nature: Phys. Sci.* **1973**, *241*, 20.

139. Brust, M.; Walker, M.; Bethell, D.; Schiffrin, D. J.; Whyman, R. *Chem. Commun.* **1994**, 7, 801.

140. Manna, A.; Chen, P.; Akiyama, H.; Wei, T.; Tamada, K.; Knoll, W. *Chem. Mater.* **2003**, *15*, 20.

141. Perrault, S. D.; Chan, W. C. W. *J. Am. Chem. Soc.* **2009**, *131*, 17042.

142. Zhang, J.; Du, J.; Han, B.; Liu, Z.; Jiang, T.; Zhang, Z. *Angew. Chem.* **2006**, *118*, 1134.

143. Weissleder, R. *Nat. Biotechnol.* **2001**, *19*, 316.

144. Hu, M.; Chen, J.; Li, Z.Y.; Au, L.; Hartland, G. V.; Li, X.; Marquez, M.; Xia, Y. *Chem. Soc. Rev.* **2006**, *35*, 1084.

145. Pong, B. K. et al. *J. Phys. Chem. C* **2007**, *111*, 6281.

146. Lin, S. –Y.; Tsai, Y. –T.; Chen, C. –C.; Lin, C. –M.; Chen, C —H. *J. Phys. Chem. B* **2004**, *108*, 2134.

147. Shukla, R.; Bansal, V.; Chaudhary, M.; Basu, A.; Bhonde, R. R.; Sastry, M. *Langmuir* **2005**, *21*, 10644.

148. Khlebtsov, N.; Dykman , L. *Chem. Soc. Rev.* **2011**, *40*, 1647.

149. Li, Y.; Liu, J.; Zhong, Y.; Zhang, J.; Wang, Z.; Wang, L.; An, Y.; Lin, M.; Gao, Z.; Zhang, D. *Int. J. Nanomedicine* **2011**, *6*, 2805.

150. Skrabalak, S. E.; Chen, J.; Au, L.; Lu, X.; Li, X.; Xia, Y. *Adv. Mater*. **2007**, *19*, 3177.

151. Lal, S.; Clare, S. E.; Halas, N. J. *Acc. Chem. Res.* **2008**, *41*, 1842.

152. Murphy, C. J.; Gole, A. M.; Stone, J. W.; Sisco, P. N.; Alkilany, A. M.; Goldsmith, E. C.; Baxter, S. C. *Acc. Chem. Res.* **2008**, *41*, 1721.

153. Rosi, N. L.; Mirkin, C. A. *Chem. Rev.* **2005**, *105*, 1547.

VITA

Sukhada Mishra was born on 14th October, 1986 in Dombivli, Maharashtra, India. In 2008, she received her Bachelor of Technology (B. Tech.) degree in Surface Coating Technology, from Institute of Chemical Technology (formerly UDCT), Mumbai. Upon completion, she joined Missouri University of Science and Technology to pursue Ph.D. in Chemistry. During the course of her research, she has published 2 journal articles, submitted 2 articles, and presented her research in 1 regional and 3 ACS national conferences. She also co—authored a book chapter in the book titled ‘Lean Systems: Applications and Case Studies in Manufacturing, Service & Healthcare’ written by Dr. David Dietrich *et. al.* In August, 2013 she received her Ph.D. in Chemistry from Missouri University of Science and Technology.